Carbon Nanotube/Polyimide Film Based Strain Microsensor for Carbon Fiber/Epoxy Composites

Marco Cen

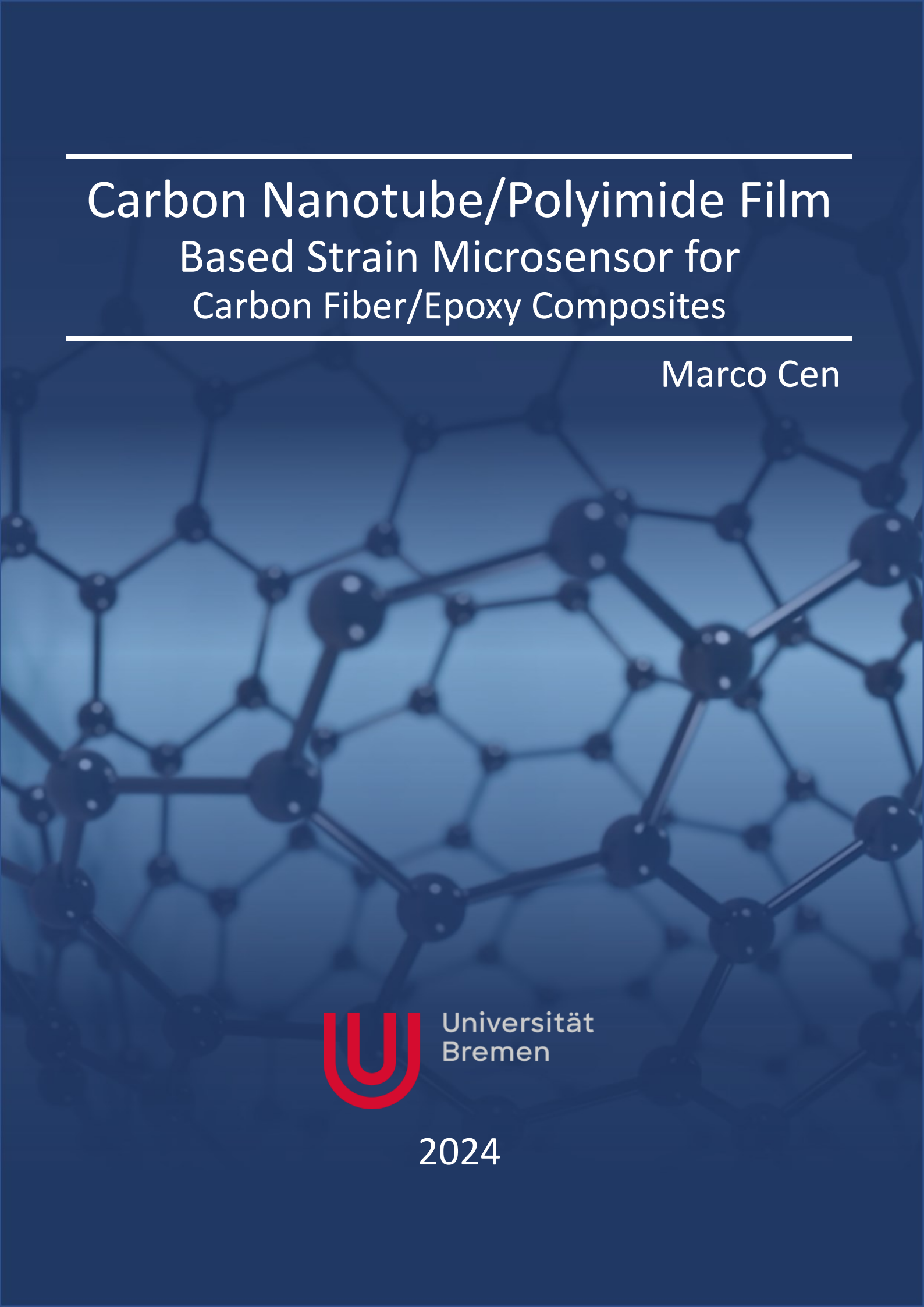

Universität Bremen

2024

Carbon Nanotube/Polyimide Film Based Strain Microsensor for Carbon Fiber/Epoxy Composites

Marco Cen

2024

Universität Bremen

Faculty of Physics and Electrical Engineering

Institute for Microsensors, -actuators and –systems

Carbon Nanotube/Polyimide Film Based Strain Microsensor for Carbon Fiber/Epoxy Composites

Dissertation approved to obtain the academic degree of

Doctor of Engineering (Dr.-Ing.)

by

M.Sc. Marco Antonio Cen Puc

First reviewer: Prof. Dr.-Ing. Walter Lang

Second reviewer: Prof. Dr.-Ing. Steffen Paul

Date of submission: 18.07.2024

Date of colloquium: 29.10.2024

I dedicate this work to my family

Thank you for all your love and support

Este trabajo está dedicado a mi familia

Gracias por todo su cariño y apoyo

Acknowledgements

I would like to express my gratitude to Prof. Dr.-Ing. Walter Lang for giving me the opportunity to pursue my PhD at IMSAS. This represented for me a great chance to learn about microtechnology and sensor development.

To Dr.-Ing. Andreas Schander, for his invaluable guidance in microfabrication, thank you for sharing your expertise since the very beginning of this work.

Thanks to Dr.-Ing. Minerva Vargas for her contributions to the percolation modeling. She has been a sister that life gave me in Germany, I appreciate all her advice and friendship.

To my colleague Tim de Rijk, who shared topics of the work with nanoparticles, thanks for his contributions in our joint publications like our IEEE Sensors Conference in Dallas… *Howdy!*

I want to thank Dr.-Ing. Sarah Bornemann for her assistance with the sensors embedding into fiber composites at our small "Faserinstitut" at IMSAS.

I want to mention Ana, Lukas and Wiebke, thank you for the coffee breaks and the Mario Kart games at IMSAS. I am happy we went together to the Eurosensors Conference in Italy.

This work couldn't be possible without the support of the technicians Melanie Kirsch, Ingrid Michaels and Eva-Maria Mayer.

I also thank Lisa Reichel for her kind assistance with paperwork at the university.

Thanks to the people from IGS, to Dr.-Ing. Ingrid Rügge for her support to the PhD candidates, and of course to Vishnu, Mong, Lambert, Gabriel and Raúl for their friendship.

I want to mention my friends outside IMSAS: Jorge, René, Ricardo, Alejandro, Samuel, Dhanisha, Rahman, Julio and Thomas Neumann.

I appreciate the support from the National Council of Science and Technology of Mexico (CONACYT) and the German Academic Exchange Service (DAAD) through the CONACYT-DAAD doctoral scholarships program.

Finally, I want to make a very special mention to Julia Hermes for all her support during all these years. Words in a single language are not enough, thank you so much! Vielen Dank! ¡Muchísimas gracias! Merci beaucoup! Jach níib óolal chan Julia!

Abstract

The work reports the development of strain sensors based on a 5 µm thick piezoresistive polyimide film. A direct mixing process of carbon nanotubes with polyimide precursor was proposed for the material fabrication. As a proof of concept, the sensor was embedded within carbon fiber composites for strain measurements.

For the development of the sensors, the following steps were performed:

- The adhesion between polyimide layers was investigated using surface treatments based on oxygen plasma and alkaline solutions.
- Modeling of the electrical percolation of films was proposed to predict the amount of nanoparticles required to achieve electrical conductivity of the polyimide films.
- The fabrication of a nanotube/polymer film was performed using ultrasonication and direct mixing approaches. As an alternative, graphene nanoplatelets were also tested.
- The piezoresistive characterization of the nanotube/polyimide films was performed to evaluate the material sensitivity under applied strain.
- The nanotube content of films and the minimum size for sensor structures were determined considering photolithography for the microfabrication of the sensors.

The surface modification of the polyimide indicated that oxygen plasma is the proper route for ensuring the adhesion between the sensor layers.

The direct mixing proposed for this work was the most efficient approach to produce polyimide films with 1.5 - 3 % nanotube contents. This particle content agreed with the predictions of the material percolation. On the other hand, graphene was not a suitable material due to its higher percolation threshold (>10 %).

The sensors were fabricated as meander structures, with an aspect ratio of length/width = 10 and a minimum linewidth of 50 µm. The embedded devices showed a gauge factor K = 10.7, which is five times higher than the sensitivity of commercial strain gauges (K = 2).

These sensors could be used as integrated sensors in different structural parts for online monitoring of forces or strain. The proposed material has additional potential applications such as pressure and temperature sensing, or polymer cure monitoring.

Kurzfassung

Diese Arbeit berichtet über die Entwicklung von Dehnungssensoren auf Basis eines 5 µm dicken piezoresistiven Polyimidfilms. Zur Materialherstellung wurde ein Mischprozess von Kohlenstoffnanoröhren mit Polyimid-Präkursor vorgeschlagen. Als Machbarkeitsnachweis wurde der Sensor zur Dehnungsmessung in Kohlefaserverbundwerkstoffe eingebettet.

Für die Entwicklung des Sensors wurden folgende Schritte durchgeführt:

- Die Haftung zwischen Polyimidschichten wurde durch Oberflächenbehandlungen auf Basis von Sauerstoffplasma und alkalischen Lösungen untersucht.
- Die elektrische Perkolation von Filmen wurde modelliert, um die nötige Mindestanzahl der Nanopartikel für einen elektrisch leitfähigen Polyimidfilm vorherzusagen.
- Nanoröhren-/Polymerfilme wurden durch Ultraschall und direktes Mischen hergestellt. Auch graphemische Nanopartikel wurden getestet.
- Zur Bewertung der Empfindlichkeit des Materials wurde eine piezoresistive Charakterisierung der Nanoröhren-/Polyimidfilme durchgeführt.
- Der Nanoröhrengehalt und die Mindestgröße der Sensorstrukturen wurden unter Berücksichtigung der Photolithografie als Mikrofabrikationswerkzeug bestimmt.

Die Oberflächenmodifikation des Polyimids zeigte, dass Sauerstoffplasma der richtige Weg ist, um die Haftung zwischen den Sensorschichten sicherzustellen.

Das vorgeschlagene direkte Mischen war der effizienteste Ansatz zur Herstellung von Polyimidfilmen mit einem Nanoröhrengehalt von 1,5 - 3 %. Dieser Partikelgehalt stimmte mit dem Perkolationsmodell überein. Andererseits war Graphen aufgrund seiner höheren Perkolationsschwelle (>10 %) kein geeignetes Material.

Die Sensoren wurden als Mäander mit Linien im Seitenverhältnis von Länge/Breite = 10 und einer Linienbreite von mindestens 50 µm hergestellt. Die integrierten Sensoren hatten einen Faktor K = 10,7, fünfmal höher als die Empfindlichkeit von kommerziellen Sensoren (K = 2).

Die entwickelten Sensoren könnten in Strukturen integrierte Elemente sein, um Kraft oder Dehnung zu messen. Das vorgeschlagene Material hat weitere potenzielle Anwendungen wie Druck- und Temperaturmessungen oder die Überwachung der Polymeraushärtung.

Content

x

List of Tables

List of Figures

Glossary

α	Thermoresistivity coefficient
γ	Surface energy
ε	Mechanical strain
θ	Angle
κ	Electrical conductivity
μ	Percolation exponent
ρ	Electrical resistivity
σ	Mechanical Stress
A	Cross-sectional area
E	Elastic modulus
F	Force
f_c	Percolation threshold
f_{wt}	Mass fraction of carbon nanotubes
K	Gauge factor
L	Length
m_{CNT}	Mass of carbon nanotubes
m_{PI}	Mass of polyimide
R	Electrical resistance
v_{CNT}	Volume fraction of carbon nanotubes
v_{PI}	Volume fraction of polyimide
wt.%	Weight percentage of carbon nanotubes
APTES	Aminopropyltriethoxysilane
CF_4	Carbon tetrafluoride
CNT	Carbon nanotube
DI water	Deionized water
DMSO	Dimethyl sulfoxide
HCl	Hydrogen chloride
ICP	Inductively coupled plasma
KOH	Potassium hydroxide
NMP	N-Methyl-2-pyrrolidon
O_2	Oxygen
PEI	Polyethyleneimine
PI	Polyimide
RIE	Reactive-ion etching
RPM	Revolutions per minute
SEM	Scanning electron microscope
SiO_2	Silicon oxide
UV-light	Ultra violet light

Introduction

In our modern world, sensors are everywhere because electronic devices have sensors as essential components. Different sensor types (temperature, pressure, humidity, etc.) are included in many objects like washing and coffee machines, vehicles and smartphones. At the same time, polymer materials have been used in a wide range of applications, such as rubber sealing elements, structural components of aircraft or cars, electronics housing, toys, home appliances, etc.

In the case of polymers, epoxy resins can be combined with stiff elements in the form of fibers (glass, carbon, etc.). Those fiber composites offer good stiffness, lightweight and corrosion resistance, and they can be easily shaped. These characteristics are desirable for automobile parts, airplanes, bridges, wind turbines and even medical prosthetics.

One important aspect when working with polymer fiber composites is the regular evaluation of the material for preemptive failure detection of structural elements. This is also known as “online health monitoring” and can be achieved by embedding sensors within the composite materials. For example, capacitive sensors can measure moisture absorption, and piezoelectric sensors can detect material cracks. Electrically conductive or optical fibers can also detect material failure. However, the large size of sensors, stiffness, or thermal expansion mismatch represents a drawback as it can lead to a disruption of the composite materials, also called the “wound effect”.

An interesting approach to reduce material disruption is the use of thin flexible sensors based on polymers. Although current technology involves polymer/metal layer combinations, there are still problems due to a mismatch of material properties (mechanical stiffness, thermal expansion, etc.), and the adhesion challenge between material layers. One way to overcome this issue is the use of piezoresistive polymer films as a replacement for metal layers.

The work presents the results of the development of strain sensors based on a piezoresistive polyimide film. The piezoresistive film was obtained by a mixture of carbon nanotubes and the prepolymer. As an application example, the prototype sensor was embedded within a carbon fiber/epoxy composite to detect applied cyclic strain.

Chapter 1: Background

1.1 Self Sensing Materials

In the last decades, a wide range of composite materials has been developed to cover different applications in the fields of aerospace, medicine, energy, etc. In the case of structural materials, self-sensing materials arise as an enhanced material type that is capable of detecting or measuring an applied stimulus [1,2]. Such self-sensing materials could, for example, detect mechanical damage, enabling the continuous nondestructive evaluation of the structural components. This idea has been proposed for its use in materials such as carbon fiber composites and concrete (Fig. 1.1), which is also known as "structural health monitoring".

Material with self-sensing capabilities can be developed by the use of embedded sensors within the materials during the design of structural parts. One step further could even be accomplished by the addition of actuators and computer systems, which produce not only sensing capabilities, but also provide an active response. Such enhanced materials are also called intelligent or smart materials [3].

a)

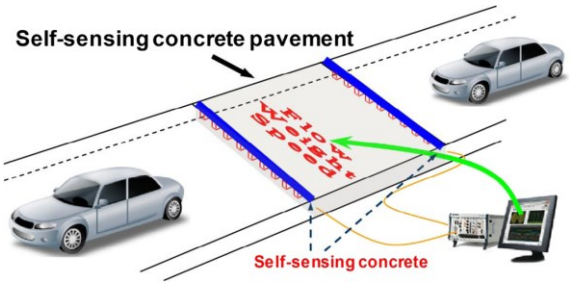

a)

Fig. 1.1 Example of self-sensing materials. a) Self-sensing fiber composites for aircraft [4]. b) Self-sensing concrete concept [5].

Several types of sensors can be integrated into the materials for real-time sensing, such as optic fibers, piezoelectric sensors, electrically conductive fibers and capacitive probes, just to name some of them [3]. However, it is necessary to keep in mind that the integration of sensors may lead to a downgrading of the macroscopic properties of the host material. If the size of the sensing element is too large or too thick in comparison to the host element, it can

be considered a wound. Moreover, if the mechanical stiffness of the sensor has a huge mismatch with the surrounding material, it can impact on the transfer of the loads or strain from the material [6].

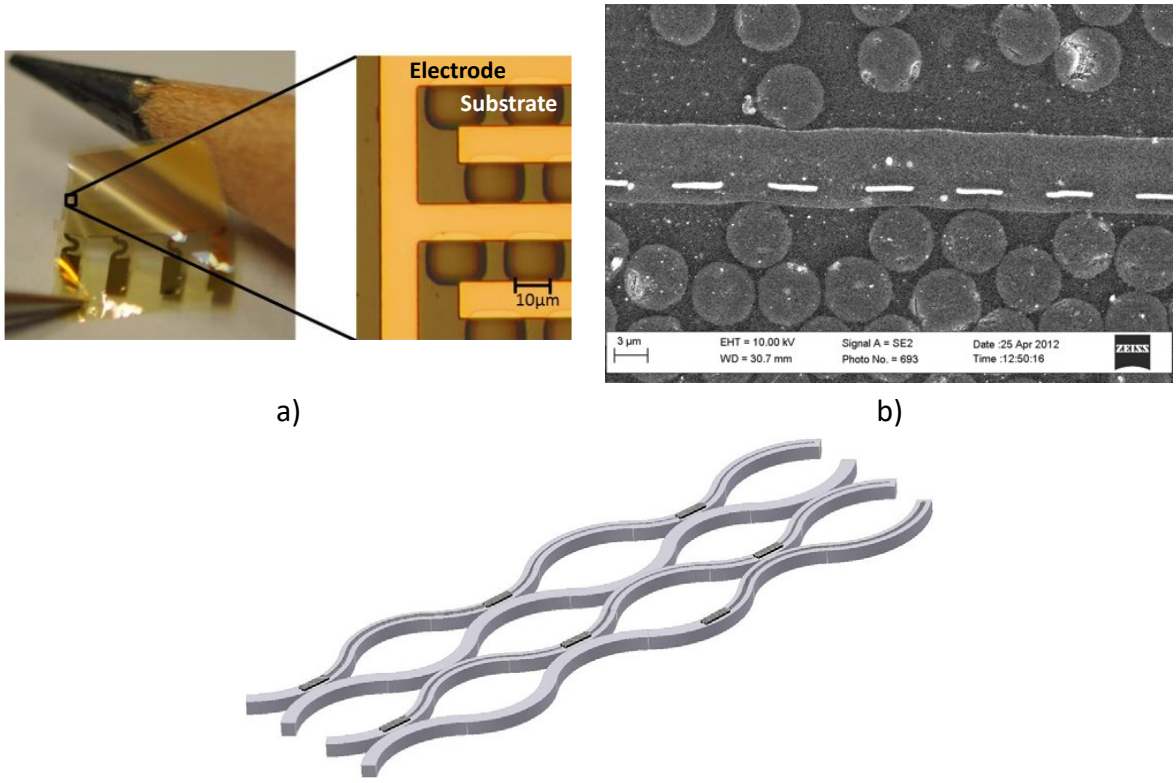

Fig. 1.2 Example sensors for integration into composites. b) Thin capacitive sensor [7]. b) Micrograph of embedded sensor within a carbon fiber composite [8]. c) Concept of a functional net for embedding applications [9].

Some research has pointed out the need of using sensors as small as possible and with a proper geometry [9] to minimize the “foreign body” effect. In such cases, thin flexible sensors present a significant integration improvement in comparison with other bulkier sensors. Such flexible sensors can be attained by using thin polymer substrates in combination with other thin material layers. By using this approach, miniature capacitive sensors (Fig. 1.2a) with a thickness of 10 µm can be integrated within carbon fiber composites (Fig. 1.2b). This type of sensors may be useful for monitoring applied strain, moisture uptake or resin curing of fiber composites [7]. Furthermore, this idea can be extended to the future concept of a functional net (Fig. 1.2c), which can be conceived as a set of small sensors in a small area. By considering a small footprint, matrix flow is allowed around the sensing device, improving integration with the host material [9]. However, further improvements in the fabrication of thin flexible

sensors must be done by testing new material combinations, since the adhesion between layers, like polymer to metals may be particularly challenging.

1.2 Commercial Strain Gauges

The strain is defined as the percentage of deformation that a body shows under the action of an applied force. This deformation can be converted into an electrical signal using a strain sensor. Commercial strain gauges are sensors that have an electrical resistance (R), which is a function of an applied strain (ε). Commercial strain sensors are typically made of a metal resistance layer with a zigzag pattern or meander structure, which is produced on a flexible substrate [10]. The working principle of those devices is the piezoresistivity: the resistor element exhibits a change in its electrical resistance when it is strained. Here, the dimensions of the strained element change; the cross-sectional area (A) is reduced and its length (L) is increased, which in total increases the electrical resistance of the resistor element. This relationship between the electrical resistance, geometry and material resistivity (ρ) is represented as [10]:

$$R = \rho(L/A) \qquad \text{Eq. 1.1}$$

Once the sensing element is deformed, the relationship between the applied deformation (ε) and its changes in electrical resistance (ΔR) is given by [10,11]:

$$\Delta R/R_0 = K\varepsilon \qquad \text{Eq. 1.2}$$

where K is the gauge factor and refers to the sensitivity of the sensor under an applied strain ε, which is defined as the normalized deformation of the element according to the initial length (L_0) as:

$$\varepsilon = \Delta L/L_0 \qquad \text{Eq. 1.3}$$

The most common materials for the fabrication of commercial strain gauges are metals and alloys like constantan, nichrome and platinum. The typical electrical resistances of commercial devices have values in the range of 100 Ω to kΩ and sensitivities of K ≈ 2. They are usually connected to resistance bridges to produce voltage values that can be amplified. Examples of commercial strain gauges are shown in the Fig. 1.3.

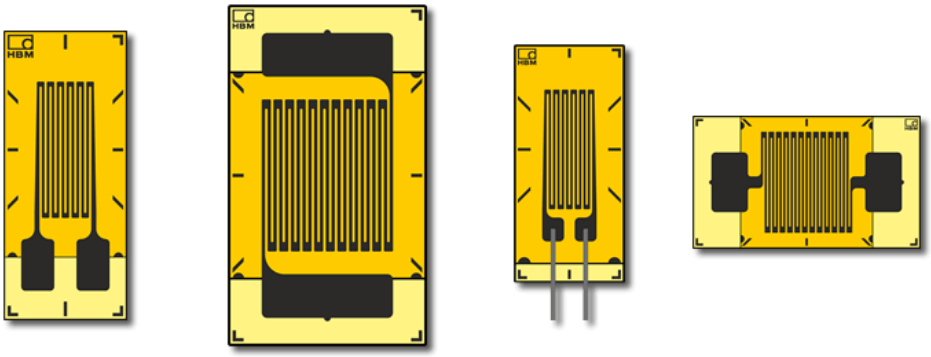

Fig. 1.3 Example of commercial foil strain gauges [12].

1.3 Fiber Composite Materials and Fabrication Methods

A composite material is defined as the combination of two or more elements that produce a new material whose properties (thermal, electric, mechanical, etc.) have a combination of its constituents [13,14]. There are several configurations of composites, for example, based on the reinforcement geometry, they could be particles or flakes composites, short or continuous fibers composites. Moreover, the fiber orientation can be random, aligned, 0° - 90° oriented, or multidirectional oriented (Fig. 1.4).

In fields like aerospace or civil construction, the need for materials with better mechanical performance has led to the use of reinforcing material (typically in the form of fibers) that is added to a matrix material (polymer, metal or ceramic). The fibers improve the mechanical stiffness, while the matrix transfers the mechanical loads to the fibers. The matrix material also keeps the shape of the part and protects the fibers from the surrounding conditions. Such material combinations can produce materials with a higher stiffness-to-weight ratio in comparison to a part based on a single material like a metal.

The most common type of reinforcement geometry for composite materials is long fibers, and many types of fiber materials are used for the fabrication of composites like glass, metal, carbon, ceramic, etc. In the case of carbon fibers, they are produced from organic precursors like Polyacrylonitrile or pitch. The precursor is carbonized and graphitized using high temperatures to produce a material with a high elastic modulus. Carbon fibers are used in the aerospace industry for the fabrication of the body and wings of aircraft, but they can also be found in the fabrication of car parts and medical prostheses [13].

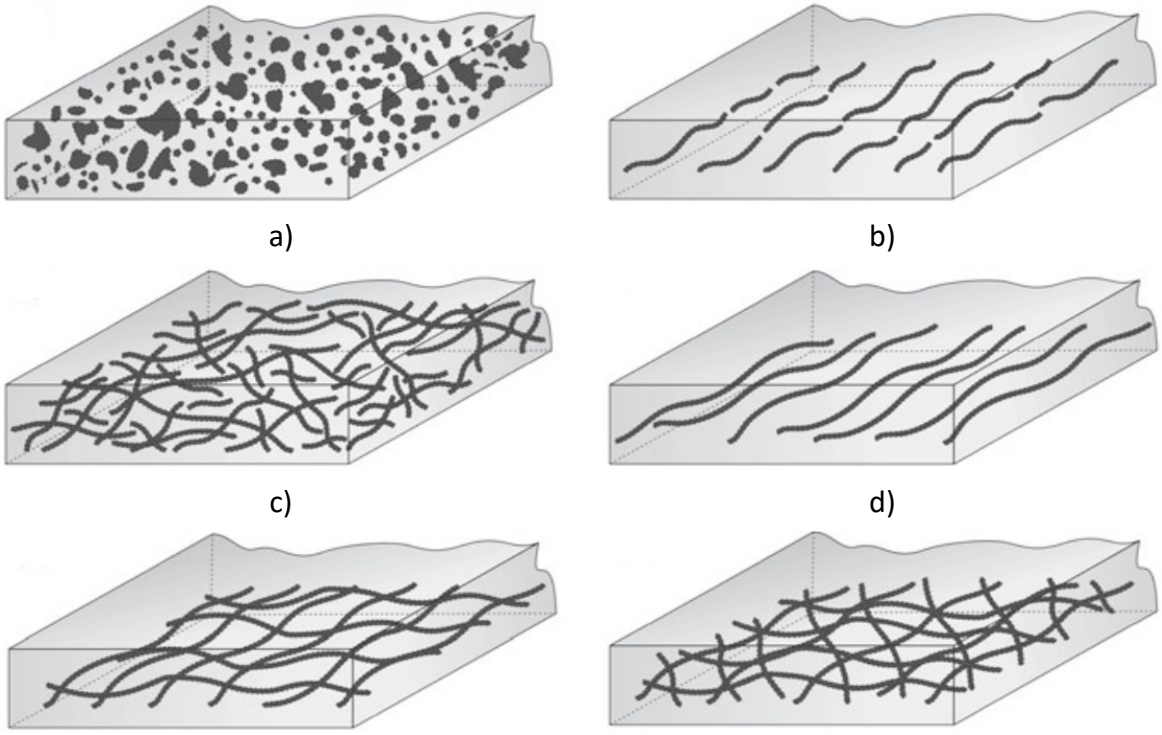

Fig. 1.4 Typical classification of composite materials [15]. a) Particle reinforced. b) Aligned short fibers. c) Randomly oriented short fibers. d) Aligned continuous fibers. e) Continuous 0° - 90° fibers. f) Multidirectional continuous fibers.

Among the common matrices used for the manufacture of fiber composites, polymers are characterized by a lower strength, lower elastic modulus, and lower temperature resistance in comparison to other materials like metals or ceramics. However, polymers are more resistant to chemicals than metal materials.

Polymers are generally not electrically conductive, they are formed by long molecular chains and can be classified into two main groups: thermoplastics and thermosets [13]. Thermoplastic polymers can melt on heating, whereas thermosets present cross-linked molecules that form a network and therefore do not soften when heating (see Fig. 1.5). The two most common polymers used for the fabrication of fiber composites are polyester and epoxy resins, both are thermosets polymers. Epoxy resin is a material that contains epoxide groups in its structure and is usually more expensive than polyester resins, but it exhibits better resistance to moisture, lower shrinkage, higher resistance to temperature and better adhesion to certain types of fibers.

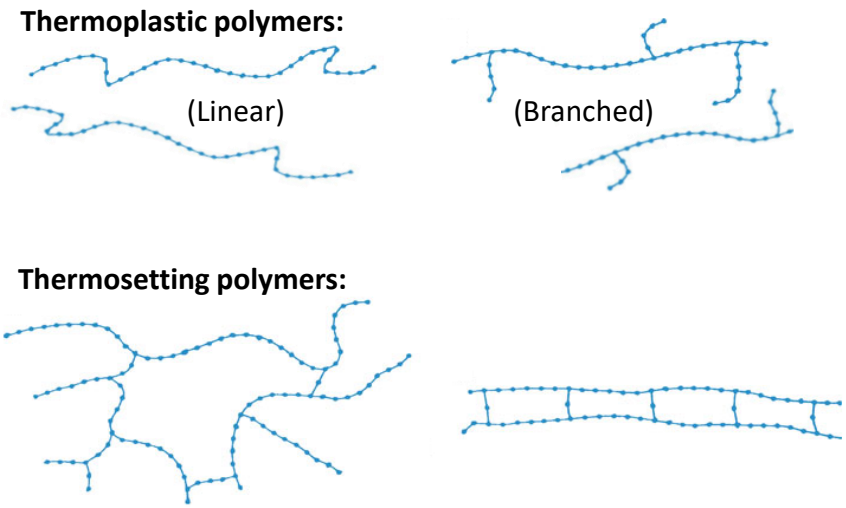

Fig. 1.5 Molecular structure of thermoplastic and thermosetting polymers [13].

There are several methods for the fabrication of fiber composite parts, but they can be divided into two major groups [16]: direct impregnation and indirect impregnation.

For direct impregnation, methods include:

Handy lay-up (Fig. 1.6). Here the fibers (chopped or woven) are placed on top of the molding surface and they are coated with the resin. The resin is applied by hand using a roller. Several layers can be applied until the desired thickness for the material is obtained.

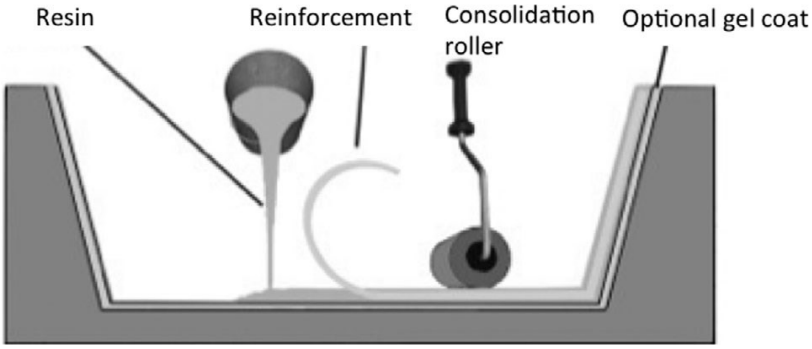

Fig. 1.6 Schema of the handy lay-up fabrication process [16].

Spray-up. This method can be considered a semi-automated version of the previous one. The difference is that chopped fibers are combined with the resin and sprayed together on the mold surface.

Pultrusion (Fig. 1.7). This method uses continuous fibers that are pulled through a resin bath. After resin immersion, they are heated using a die to cure the materials, producing a part with a defined section geometry.

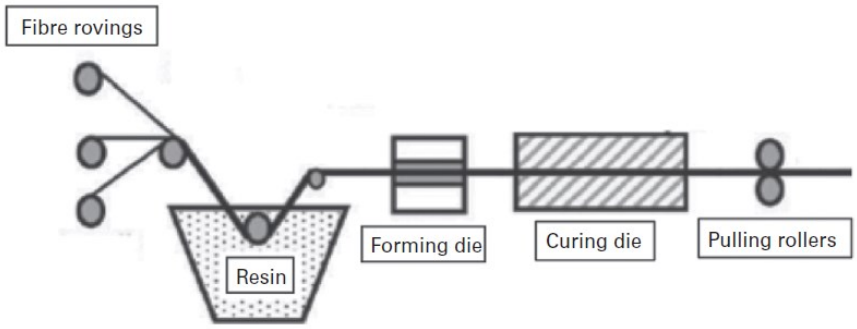

Fig. 1.7 Schema of the pultrusion process [16].

Filament winding. Continuous fibers are used in this method, the fibers are pulled through a resin bath similar to the previous method, but they are wrapped in a cylindrical shape to produce a hollow cylinder.

Resin transfer molding (Fig. 1.8). In this method, the resin is infused into a fiber preform. The preform is placed inside a mold and the resin is pumped into the mold. Vacuum can also be used to reduce the amount of voids in the final part. This variation is also known as vacuum-assisted resin transfer molding.

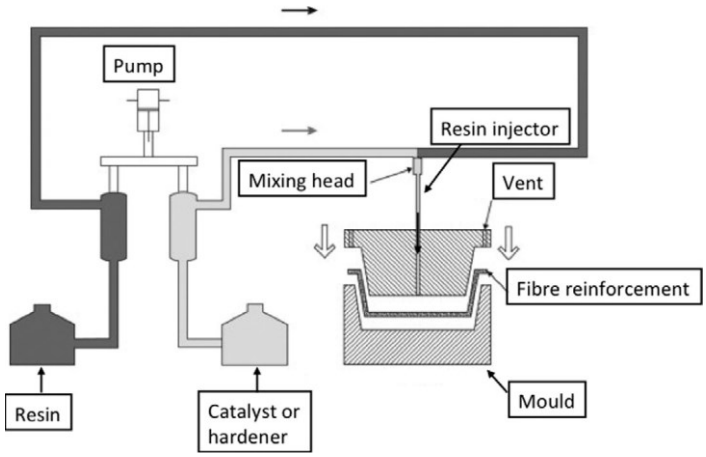

Fig. 1.8 Schema of resin transfer molding [16].

For the fabrication of elements by indirect impregnation, the fibers are pre-impregnated with the resin. The resulting pre-impregnated materials can be:

Prepreg (Fig. 1.9). The continuous fibers are impregnated with a resin. The viscosity of the resin is increased by a partial reaction with its hardener, but an additive can also be mixed. The resin is placed on a film substrate and the fibers are placed between two resin layers.

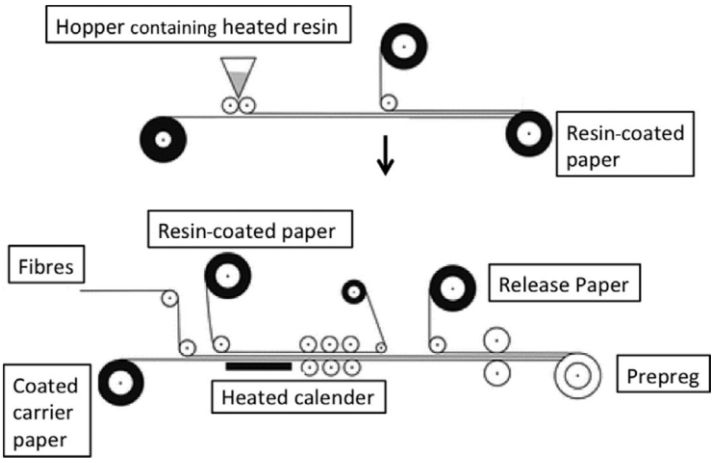

Fig. 1.9 Schema of prepreg manufacture [16].

Sheet molding compound. The fibers are chopped and mixed with a resin with higher viscosity produced by additives. The resin is first placed on a film and then the short fibers are added, a second film with resin is applied to cover the fibers.

Dough or bulk molding compound. A mixture of chopped fibers and resin is produced. This material is later used for hot press molding or injection molding.

1.4 Polyimides

Polyimides (PI) belong to the engineering polymers, as their mechanical properties and chemical resistance are more stable at higher temperatures than other polymers (>250 °C). This polymer type is desirable for coatings of cookware, structural components of vehicles and electronic components. The PIs are mostly amorphous polymers and they are resistant to oxidation and acidic environments. However, PIs can be attacked by alkaline solutions [17,18].

The aromatic PIs (with a ring chemical structure) are produced by the reaction between aromatic dianhydrides and diamines [17]. The first step involves the production of a polyamic acid using a suitable solvent, for example N-Methyl-2-pyrrolidone (NMP). After the processing (e.g. film, coating, laminate), the material is converted into PI material by heating it at temperatures above 150 °C. During this thermal curing, the chemical reaction releases water to finally produce the imide ring. The chemical reaction for PI synthesis is represented in Fig. 1.10. Some applications of polyimides include electrics (as an insulator or substrate material), automotive and aircraft engine parts, seals and bearings [17,18] and even fabrication of neurological devices [19].

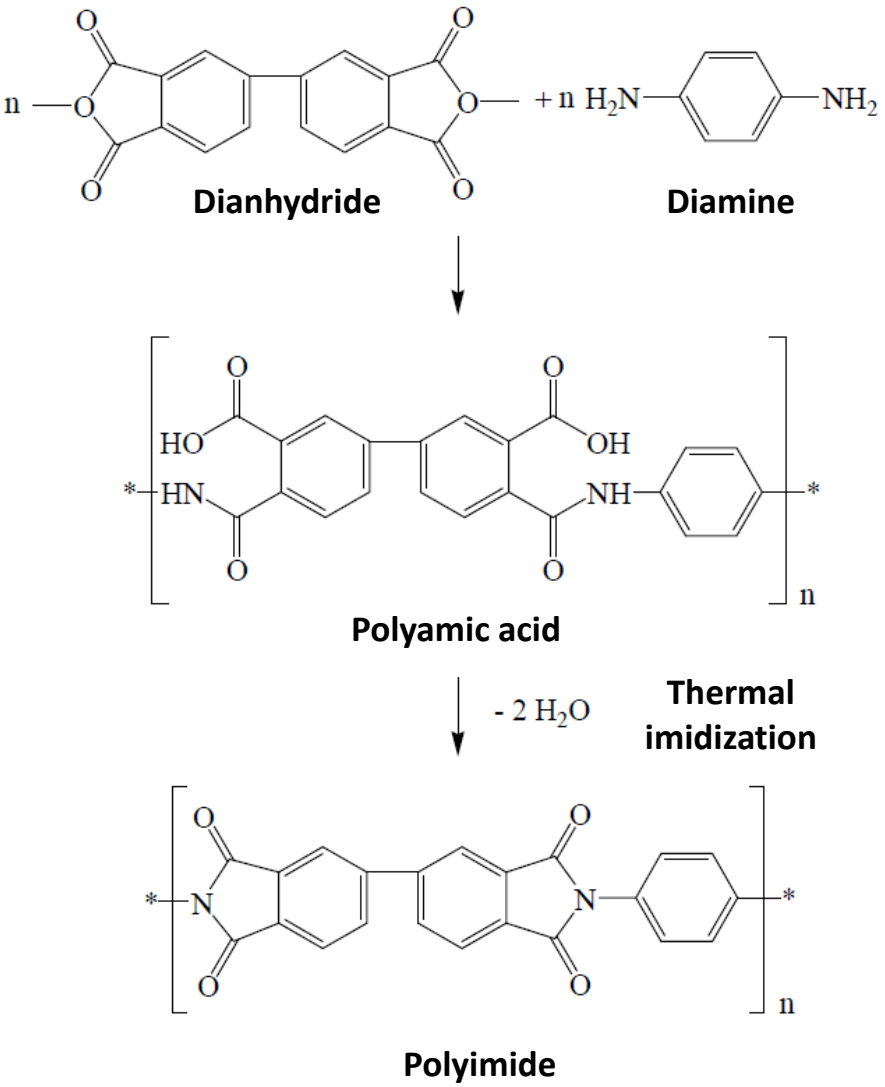

Fig. 1.10 Chemical structure and thermal synthesis of the polyimide [18].

The aimed host material for the strain sensors in the present work is a fiber/epoxy composite. Therefore, it is necessary to ensure that sensors can stand the typical curing temperature range of the resin, which ranges from 80 °C to 150 °C. The PI material is an excellent choice for the sensor development as its glass transition temperature (Tg) is 324 °C. In addition, the thermal expansion coefficient (CTE) is in the same range as epoxy resins. A comparison of some mechanical and thermal properties between commercial epoxy resin and PI is shown in Table 1.1.

Table 1.1 Mechanical and thermal properties of epoxy resin and polyimide [20,21].

Polymer	Epoxy resin	Polyimide
Elastic modulus (GPa)	2.89	9.3
Tensile strength (MPa)	75	482
Strain (%)	3.4	40
CTE ($1x10^{-6}$ /K)	52.7	60
Tg (°C)	-	324

1.5 Carbon Nanotubes

Described first in the 1990s by Iijima [22], carbon nanotubes (CNTs) are an allotrope of carbon, and they can be visualized as hollow cylindrical structures that are formed by rolling a graphene layer. The CNTs can be divided into two main classifications: single-walled (SWCNTs) and multiwalled (MWCNTs), depending on the number of concentric layers [23] in their structure (Fig. 1.11).

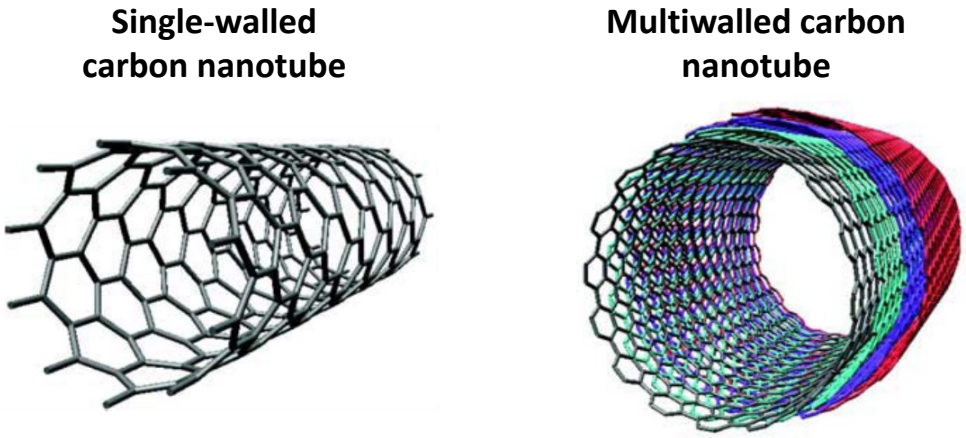

Fig. 1.11 Representation of carbon nanotubes [24].

Outstanding physical properties of the CNTs are related to their structure. For example, they are among the stiffer materials, with an elastic modulus of up to 1 TPa. Another interesting physical property is the thermal conductivity of the MWCNTs, which has been reported between 300 and 6000 W/mK. In the case of their electrical conductivity, the SWCNTs can behave as semiconductors or metallics, depending on the chirality or orientation of the carbon structure. In the case of the MWCNTs, they behave as metallic materials due to the

interactions between their layers, although the current flow occurs on their outer shell. Given their chemical structure, one more characteristic of CNTs is their thermal stability since they are stable up to temperatures close to 4000 K. Table 1.2 summarizes the typical physical properties of the MWCNTs.

Table 1.2 Typical properties of MWCNTs [23,25,26].

Property	**Reported value range**
Elastic modulus (TPa)	0.3 - 1
Electrical conductivity (S/cm)	10^2 - 10^6
Thermal conductivity (W/mK)	200 - 3000
Density (g/cm^3)	0.8 - 1.8
Outer diameter (nm)	10 - 100
Length (µm)	5 - 100
Aspect ratio (length/diameter)	≥100

Three main methods are used for the production of CNTs: chemical vapor deposition (CVD), laser ablation, and arc discharge. However, for the fabrication of commercial amounts of CNTs, the CVD method is the preferred one [23,25]. This method uses a substrate like quartz or silicon with metal catalyst particles such as nickel, cobalt or iron on it. The substrate is heated in a chamber (T>700 °C) and a flow of carbon gas such as carbon monoxide is applied, then the carbon atoms form the CNT at the edges of the metal particles and grow to form the CNT structure.

1.6 Strain Sensors based on Carbon Nanotubes

Several research has focused on the use of CNTs as an electrically conductive filler for polymer materials to produce electrically conductive polymers, which can be used for the development of different kinds of sensors [27]. This mixture of CNTs and polymers leads to a nanoparticle network inside the polymer, which allows electricity to flow through those conductive paths. A minimal amount of CNTs is required to produce such a transition from an insulator material to an electrically conductive one, this minimum filler content is known as

the electrical percolation threshold [28,29]. The selection of the CNTs instead of other materials like carbon black relies on the high aspect ratio (>100) of the CNTs. This geometry characteristic reduces the amount of the particles required to achieve electrical conduction, which is typically lower than 1 wt.% [29–31].

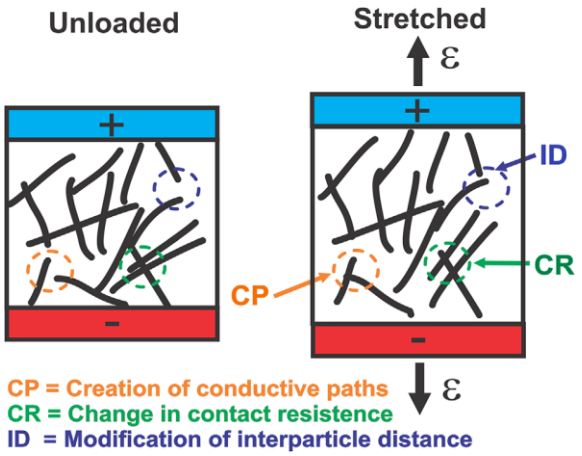

Fig. 1.12 Schema of a CNT/polymer composite and its piezoresistive effect [32]

This combination of CNT/polymer can be used for the development of piezoresistive polymers [32]. The piezoresistive property of such polymer materials relies on the changes exhibited by the CNT network during an applied strain. During the strain, the particles of the conductive network can be partially disconnected or the distance between them is increased, leading to an increase of the electrical resistance of the bulk material. Another possibility is that the section of CNTs which is connected between two other nanoparticles increases, thus changing the electrical resistance of the nanocomposite. Changes in the CNT network under an applied strain are schematized in Fig. 1.12.

All those changes in the CNT network inside the polymer under tensile strain (or compression) modify the electrical resistance of the bulk material. This property can be exploited for the fabrication of polymer-based sensors. This approach brings the possibility of using the same material (polymer) for the sensors and the host material, which should reduce the “foreign body” effect. However, a good dispersion of the CNTs within the polymer is necessary to obtain such properties with a low amount of CNTs. This later task may be challenging since the van der Walls interaction between entangled CNTs has to be overcome.

Although in the last years research has focused on the development of CNT/polymer nanocomposites as potential materials for strain sensors, it has to be noticed that most of the

reported results are mainly referred to a bulk material instead of a final sensor, i.e., strain gauges. Some of the reported strain sensors based on CNTs are presented in this section.

In the work of Ya-Ting et al. [33], a SWCNT network was synthesized by alcohol-catalytic chemical vapor deposition on a silicon wafer. The CNT later was patterned by reactive ion etching as a meander structure with a linewidth of 20 µm and a line length of 1 mm. The produced CNT array was encapsulated between two layers of parylene-C. For tensile experiments, the device was glued on a 200 x 50 mm acrylic plate. The gauge factor K of the produced sensors ranged between 4 and 6. The reported SEM images of the produced CNT structures and the complete sensor array are shown in Fig. 1.13.

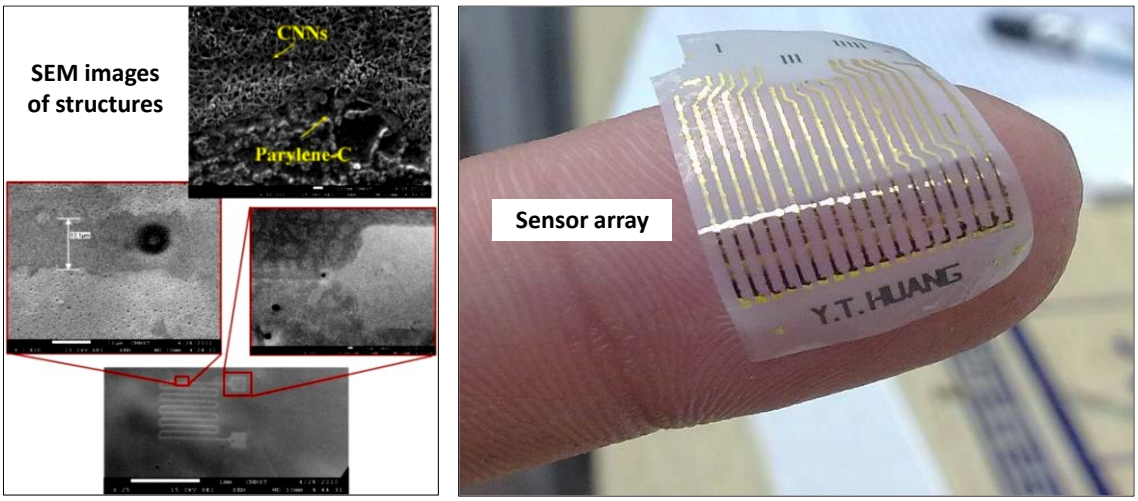

Fig. 1.13 Strain sensors produced in [33].

Another related research by Lee [34] used a PI film as the substrate for a single SWCNTs-based sensor (see Fig. 1.14). The PI film was spray-coated with a CNT solution and this layer was patterned as meander structures of around 3 mm length using oxygen plasma. The produced devices presented remarkable gauge factors of K ≈ 60. This high sensitivity of sensors was attributed to CNT arrange produced by the spray-coating. However, one consideration for this approach is that surface treatment and purification of the CNTs are required in order to enhance their adhesion to the substrate.

Another spray-coated based device was studied by Arana et al. [35], where MWCNTs were dispersed in chloroform and sprayed on a PI (kapton) film of 40 x 10 mm. The coating was repeated for a total of five layers, and the meander structures were produced using an engraving machine. The produced sensing structures (3.2 x 7.8 mm) were later covered with

a layer of polyurethane by spraying. For a tensile test of ε = 1 %, the sensors indicated a gauge factor K ≈ 0.7. This represents a lower sensor sensitivity in comparison to the work of Lee [34], indicating that the CNT-based sensors can show a wide sensitivity range.

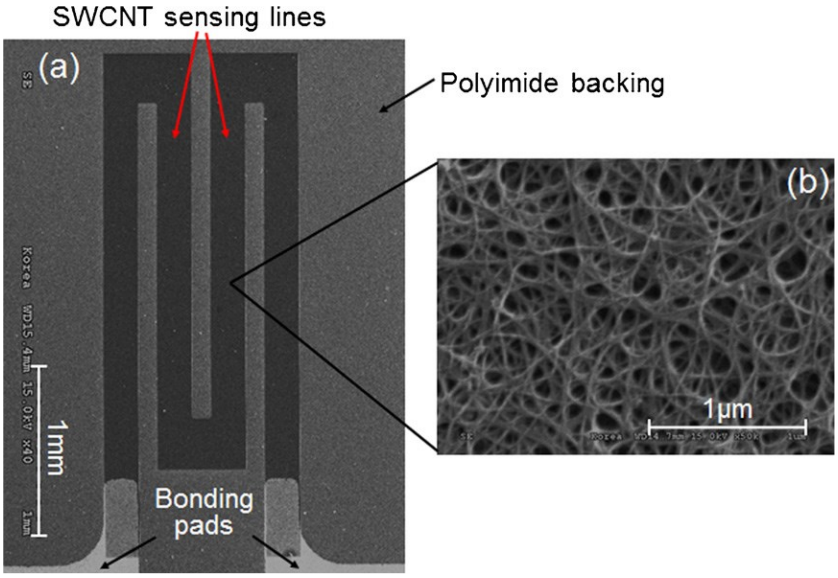

Fig. 1.14 Detail of the meander structure of a CNT-based sensor in [34].

An alternative approach for producing meander structures using CNTs is by inkjet printing (see Fig. 1.15). According to Jehn et al. [36], an MWCNT/PDMS mixture was printed on a PI film (Kapton) to produce the meander structures (8 by 0.9 mm), and the curing agent for PDMS was printed subsequently. Several printed layers allowed to control the resistance of the sensor, from 100 kΩ to 10 MΩ. The printed sensors had a gauge factor of K ≈ 1.4.

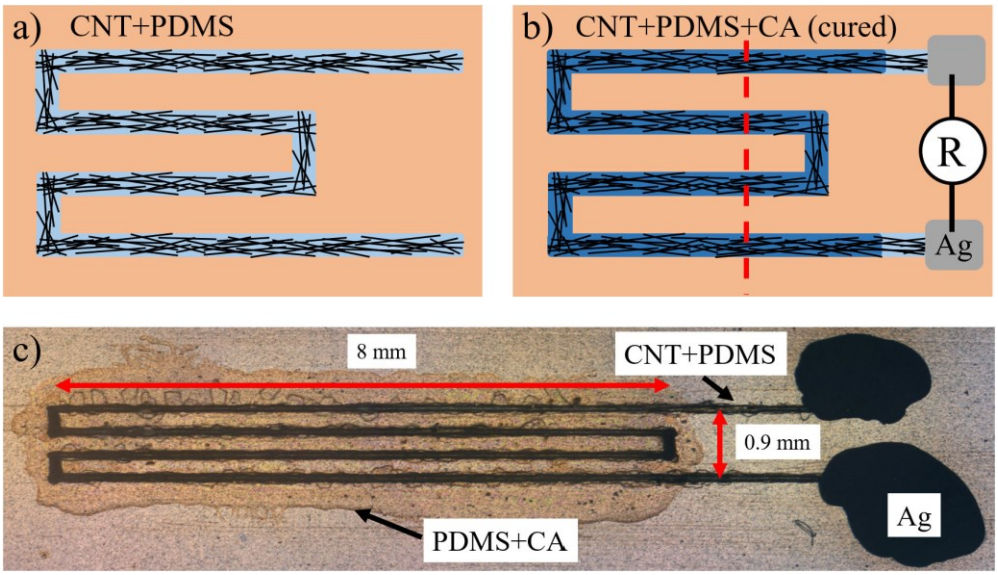

Fig. 1.15 Sensor design by inkjet printing and final sample from [36].

A similar approach was used by Peng [37] to print MWCNT sensors on quartz fabrics for applications in high-temperature intelligent textiles. The CNTs were dispersed in ethylene glycol and printed on the quartz fabrics. The printed meanders were later covered by silicate glue and dried at 120 °C. Although no gauge factor was reported, the bending test showed that the electrical resistance of samples increased with higher bending angles. However, the electrical resistance of the sensors showed a temperature dependence.

More recently, a study by Li [38] compared the sensitivity between CNT layers with and without structuring. In that work, the CNTs were coated with magnetic particles and then dispersed in ethanol for casting in an acrylic mold. After drying, the CNT layer was coated with silicon resin, and the sample was peeled after curing. For the structured samples, the acrylic mold was designed with an engraved meander structure with a magnet placed below it. The tensile test showed that for deformations below 8%, the samples without pattern have a gauge factor of K = 4.8, whereas the samples with a meander structure increased their sensitivity to K = 6.5.

Finally, the work of Hwang [39] was also based on engraving a meander mold in an acrylic plate. There, a mixture of MWCNT/epoxy (0.5 wt.%) was used to fill the mold. The sample was bag sealed, vacuumed and cured at 80 °C for 8h on a heating plate. The gauge factor of patterned samples (K = 2.5) was higher in comparison to the patch geometry samples under compression (K = 1.43) and tension (K = 2.2).

1.7 Proposed Approach for this Work

This research project proposes the use of a polymer nanocomposite film as an alternative material to metals for the fabrication of strain sensors by combining a polyimide with carbon nanotubes.

The main motivation for this approach is the reduction of thermal and mechanical mismatch usually observed on traditional sensors with different material layer build-ups. Since the expected content of nanoparticles for the polymer films is low (<10 %), it is also expected that the mechanical properties of the final material are mainly determined by the polymer component. The general approach for this work can be divided into four main steps, as represented in Fig. 1.16.

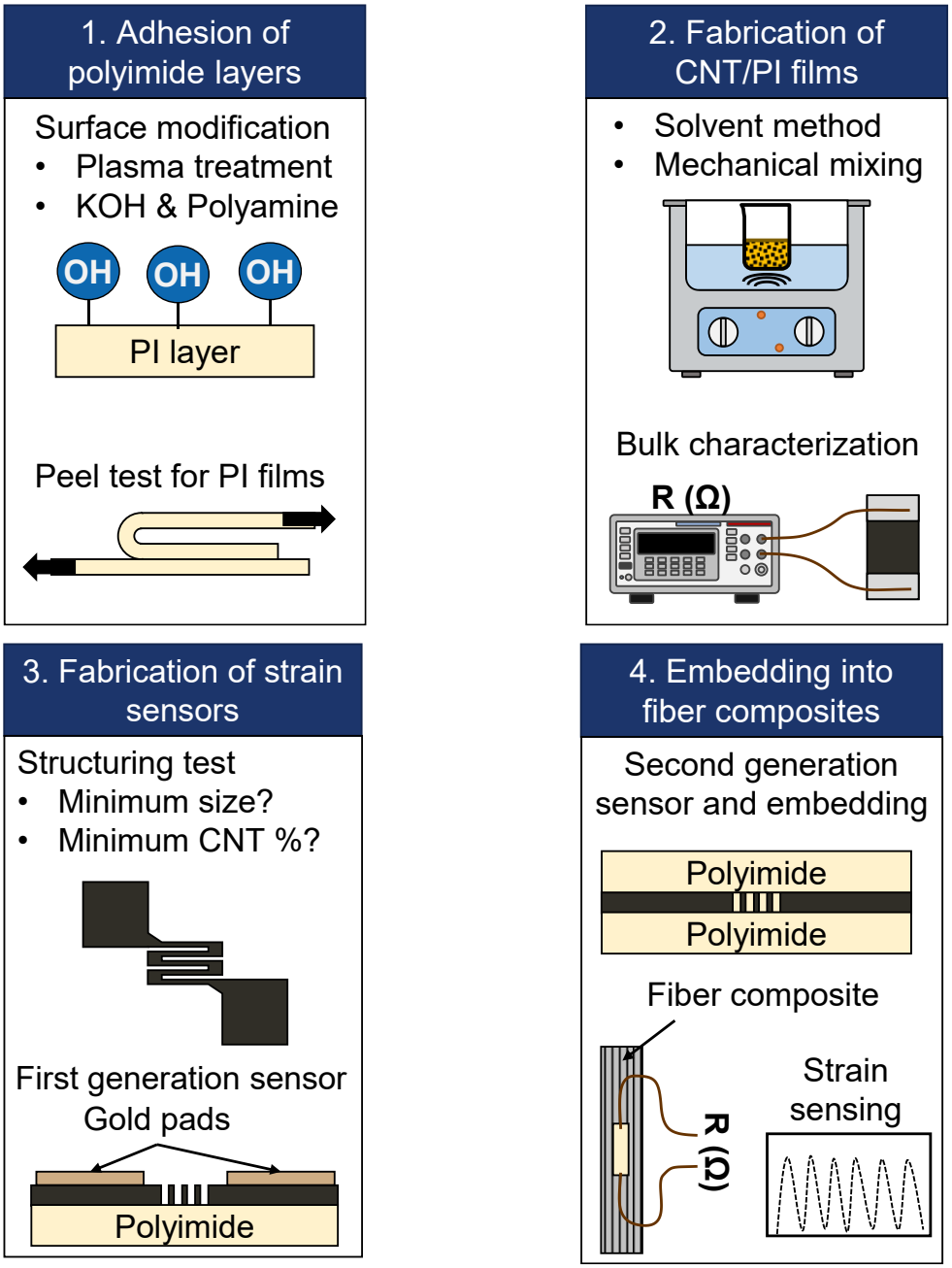

Fig. 1.16 Steps for the development of the polymer-based strain gauges.

First, the adhesion between polymer layers is achieved by the surface modification of the polymer films. For that purpose, treatments found in literature based on oxygen plasma, amine and alkaline solutions were used. Their adhesion effectivity was assessed using a 180° peel test. From this step, the surface treatment that provided the better adhesion between polyimide films was kept for the fabrication of sensors.

The second research step involved the fabrication of the polymer nanocomposite films. Two mixing approaches were compared, one based on the use of solvents and ultrasonication for

the dispersion of the nanoparticles, and a second one based on direct mechanical mixing. The characterizations performed for the nanocomposite included the electrical conductivity, piezoresistivity response, mechanical resistance and thermoresistive behavior of the material as a bulk film.

Once the film adhesion and nanocomposite film fabrication methodologies were defined, the third step was focused on the development of the first generation of sensors. The sensor design was based on the bibliographic review considering a meander-structured device. The smallest sensor size and other parameters were determined in this step. For the evaluation of the sensors, those were fabricated on top of a polyimide substrate and their sensitivity was measured under applied strains.

The last step involved the fabrication of a second sensor iteration, which was embedded into a carbon fiber composite laminate for a cyclic strain. The results showed that the produced sensor can be used for strain monitoring of the fiber composites, with a higher sensitivity than the commercial reference sensor.

Chapter 2: Adhesion of Polyimide Films

One of the main challenges of working with devices fabricated from material layers is the adhesion between them. Usually, some sort of surface treatment or an intermediate layer is required to bond different layers. This is very important, as a good adhesion between the layers will ensure a proper transfer of forces to the sensor and mechanical stability. This chapter covers different treatments aimed at improving the adhesion between two PI layers. The effectiveness of adhesion was evaluated by a 180° peel test, and complementary characterizations included the surface wettability and surface energy of the treated films.

The main routes for such surface activation or modification of PI surfaces can be divided into wet chemistry [40–42] and plasma treatments [43–46]. In the first case, solution treatments are aimed to produce the imide ring opening of PI structure and even graft some sort of molecules, which can enhance the adhesion to a consecutive PI layer. For plasma treatments, a series of highly reactive species are produced and grafted as functional groups on the PI. The nature of the gas used during plasma treatments plays an important role for the type of grafted molecules. For example, oxygen and CO_2 plasma treatments are known for promoting hydroxyl and carbonyl functional groups.

The content of this chapter is based on a previously published article and a presentation at the LDIC Conference in 2020:

- M. Cen-Puc, A. Schander, M.G. Vargas Gleason, W. Lang, An Assessment of Surface Treatments for Adhesion of Polyimide Thin Films. Polymers 2021, 13, 1955.
- M. Veigt, M. Cen-Puc, E. Hardi, W. Lang, M. Freitag, Using RFID to Monitor the Curing of Aramid Fiber Reinforced Polymers, in: M. Freitag, H.-D. Haasis, H. Kotzab, J. Pannek (Eds.), Dynamics in Logistics, Springer Internation Publishing, Cham, 2020, 441–450.

2.1 Materials and PI Film Fabrication

The PI used for the film fabrication was the U-Varnish-S (UBE Europe GmbH), which is supplied as a prepolymer with an 18 wt.% content of polyamic acid. The adhesion promoter 3-Aminopropyltriethoxysilane (APTES) from Sigma-Aldrich Chemie GmbH was used to produce a proper adhesion between the PI films and the silicon wafers substrates (100 mm diameter and 525 µm thickness). For the solution treatments, KOH at 50 %, HCl at 37 % (MicroChemicals

GmbH), and branched polyethyleneimine (PEI) with an average molecular weight of 800 g/mol (Sigma-Aldrich Chemie GmbH) were used.

Before the fabrication of the PI films, an aqueous solution of 0.1 vol.% of APTES was spin-coated on a silicon wafer using a speed of 4000 RPM and later dried with a hotplate at 120 °C for 2 min. Then, the PI precursor was spin-coated using a speed of 3000 RPM for 60 s. The coated wafer was then placed in a vacuum hotplate RSS-HC (UniTemp GmbH) and the PI curing process followed a step temperature profile with a peak temperature of 450 °C as indicated by the material supplier; the cured PI films had a thickness average of 5 µm.

For each surface treatment condition, two PI films were tested. Their thickness was measured before and after treatments with an interferometer F20-EXR (Filmetrics Europe GmbH). Another characterization was performed by water contact angle with the drop shape analyzer DSA II from Krüss. A total of five DI water drops (2.5µL/min flow) were randomly placed on the film surface, and the drop angle was obtained with the software of the device.

2.2 Solution Treatments for Surface Modification of Films

The first wet chemistry approach for surface modification of the PI was based on an amine solution. In general, the amine molecules can produce an opening of the imide ring [42,47] of the polyimides. After this opening, the amine group can react with the anhydride group, leading to a molecule grafting to the original PI structure. The amination process of a PI with a polyamine molecule [47] is represented in Fig. 2.1.

For surface treatments with the PEI, a 2 wt.% PEI solution was prepared using a solvent combination of isopropanol and deionized (DI) water with a 1:1 ratio. The selected PEI has a branched structure with several amine groups that are expected to produce reactive points for chemical bonding with the next polyimide layers. The PEI solution was heated to a temperature (T) of 70 °C, and the PI films were immersed for 2, 5 and 10 min. Mechanical stirring was used during the treatment. The samples were cleaned after the treatment with DI water and dried with nitrogen at room temperature.

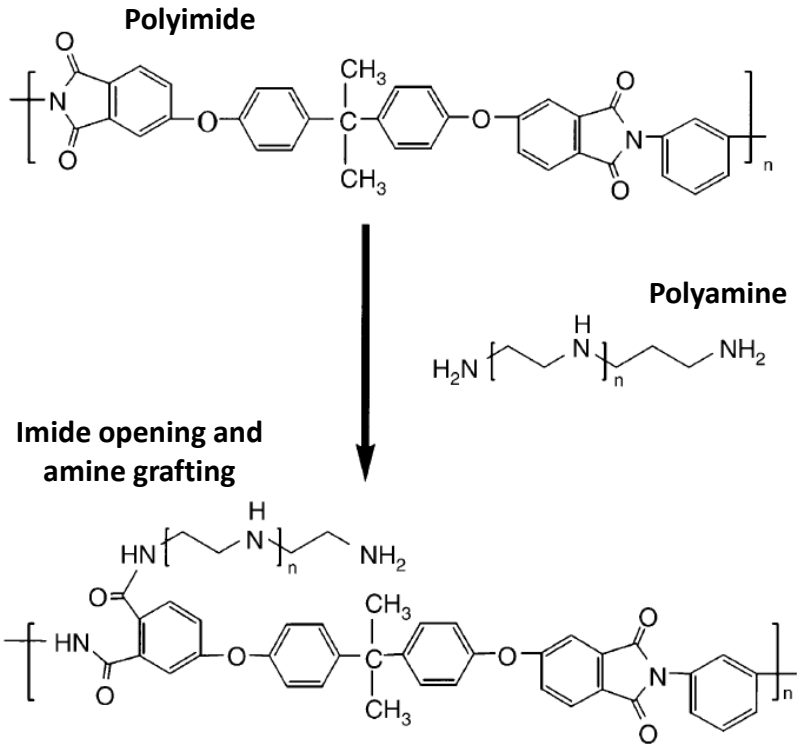

Fig. 2.1 Modification of the PI by polyamine [47].

The second route by solution treatments for the PI films was based on a combination of KOH and HCl solutions [40,41,48]. First, an aqueous KOH solution was expected to react with the imide ring of the polymer to produce a potassium polyamate. During the second step of the treatment, an aqueous solution of HCl should produce a substitution of the K atom, reversing this material to a polyamic acid, which is the PI precursor [49]. This reversing process from PI to PI precursor is represented in Fig. 2.2.

The PI films were first immersed in a KOH aqueous solution with a concentration of 1 M, with a temperature of 50 °C, and treatment times of 2, 5 and 10 min. After the immersion in KOH, the samples were washed with DI water and immersed in a aqueous solution of 0.2 M HCl for 5 min at room temperature. Both solutions were mechanically stirred during the treatment. Finally, the samples were washed with DI water and dried with nitrogen at room temperature.

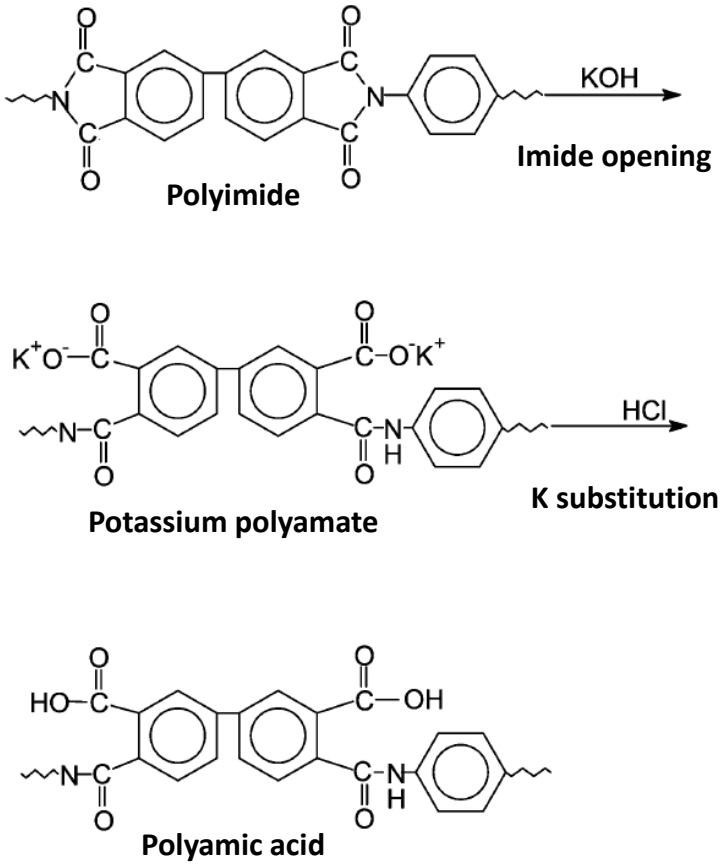

Fig. 2.2 Modification of the polyimide by KOH and HCl treatment [50].

Table 2.1 summarizes the time and temperature conditions considered for each solution-based treatment for the surface modification of the PI films.

Table 2.1 Conditions of the solution treatments for PI films.

Solution	Temperature (°C)	Time (min)
PEI (2 wt.%)	50	2, 5, 10
KOH (1 M)	70	2, 5, 10

2.3 Plasma Treatments for Surface Modification of Films

The second group of surface modification was based on oxygen plasma. Plasma treatments are used to insert functional groups into polymers. During this type of treatment, the PI molecules tend to break down and form C-O and C=O groups [44,45]; other secondary reactions can also produce -OH or COOH functional groups [43], this process is represented

in Fig. 2.3. Such chemical change leads to a higher wettability of the PI films. However, a higher surface roughness is also expected after this treatment.

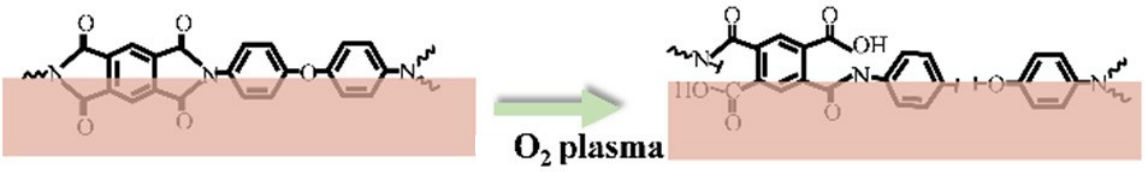

Fig. 2.3 Schema of polyimide surface activation by oxygen plasma [50].

Two different pieces of equipment for oxygen plasma were available at the IMSAS. The first one was the Tepla 400 Microwave Plasma (Technics Plasma GmbH), which is mainly used for the cleaning of material surfaces. For this device, the oxygen flow was fixed at 500 mL/min, and the power (P) was varied at 250, 500 and 1000 Watts, while the treatment times were set to 0.5, 1 and 5 min.

The second plasma device was the Multiplex ICP Reactive Ion Etcher (RIE Surface Technology Systems Ltd.), which is the equipment used for dry etching. This device was used with a combination of bias power (BP) levels of 10, 25 and 50 Watts. The times for the treatments were proposed as 0.25, 0.5, and 1 min. For this device, the coil power, oxygen flow and pressure were set as constant with the values of 800 W, 40 sccm and 5 mTorr, respectively. All the time and power combinations for the plasma treatments are presented in Table 2.2.

Table 2.2 Condition parameters of the plasma treatments for PI films.

Device	**Power (Watts)**	**Time (min)**
Microwave Plasma	250, 500, 1000	0.5, 1, 5
ICP RIE Plasma	10, 25, 50	0.25, 0.5, 1

2.4 Wettability of Treated Polyimide

Given the considerable amount of treatment conditions tested in this work, the wafers were first characterized by measuring the changes in their surface wettability as represented in Fig. 2.4a. The Polyimide films were characterized by measuring their water contact angle before and after each treatment variation with the drop shape analyzer DSA II. A total of five random points were selected on the wafer surface to obtain an average value. The pristine PI samples

exhibited a degree of hydrophilicity since the average water contact angle was 68°. However, all treated surfaces showed a significant reduction of the water contact angle, indicating that the PI surface was chemically modified. Representative pictures of a water drop on pristine and treated films are shown in Fig. 2.4b.

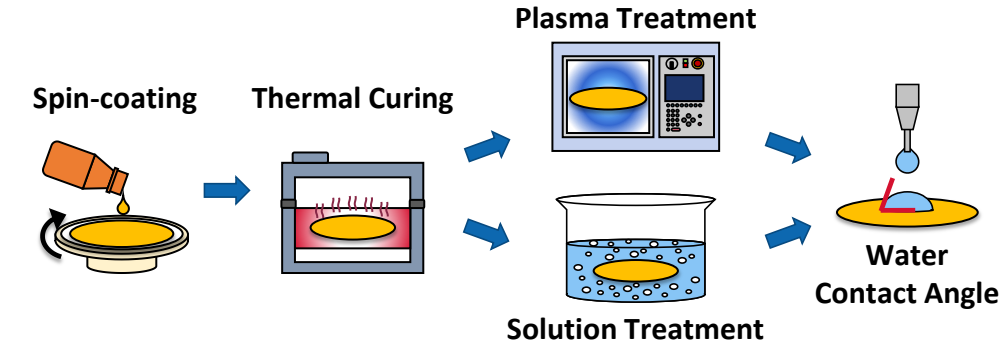

a)

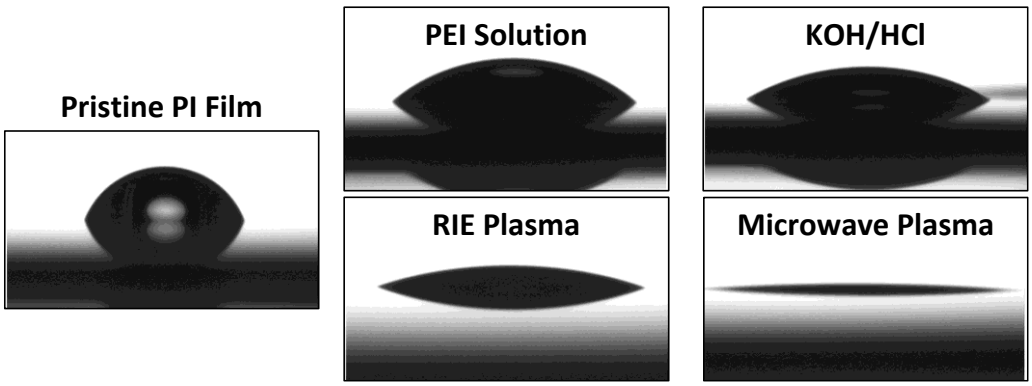

b)

Fig. 2.4 Wettability characterization of PI films. a) Schema of samples fabrication and evaluation. B) Examples of water drops on films.

After the comparison of the contact angle of the samples, only the treatment variations that produced the lowest contact angle for each treatment type were selected. Starting with the solution-based treatments, the samples modified with the PEI solution (Fig. 2.5a) showed a monotonic reduction of the contact angle with the increased treatment time, reaching a minimum value of 55.5° at 10 min of treatment, which can be considered the best treatment variation for PEI solutions.

The samples immersed In the KOH and HCl solutions (Fig. 2.5b) exhibited lower contact angles (38°) in comparison to the PEI solution, although no significant difference was observed between the different treatment times. However, since the material modification is expected

to reach deeper into the PI layer after longer immersion times into the solutions [49], a treatment time of 10 min can be assumed as better.

In general, the oxygen plasma treatments produced lower contact angles in comparison with the solution-based treatments. For the microwave plasma treated samples (Fig. 2.5c), the contact angle follows a reduction as a function of the treatment time, which was observed at each power level. The better treatment was achieved with the combination of a power of 1000 W and a time of 5 min, producing a contact angle of 7°.

The results of the RIE plasma treatments (Fig. 2.5d) did not show a monotonic dependency of the treatment time at bias powers of 0.25 or 0.5 W, since the contact angle increased with longer treatment times instead of producing further reductions. This behavior could be attributed to surface etching [43]. However, the best treatment was considered for the minimum contact angle of 13°, which was observed with a treatment consisting of a bias power of 50 W and 1 min time treatment.

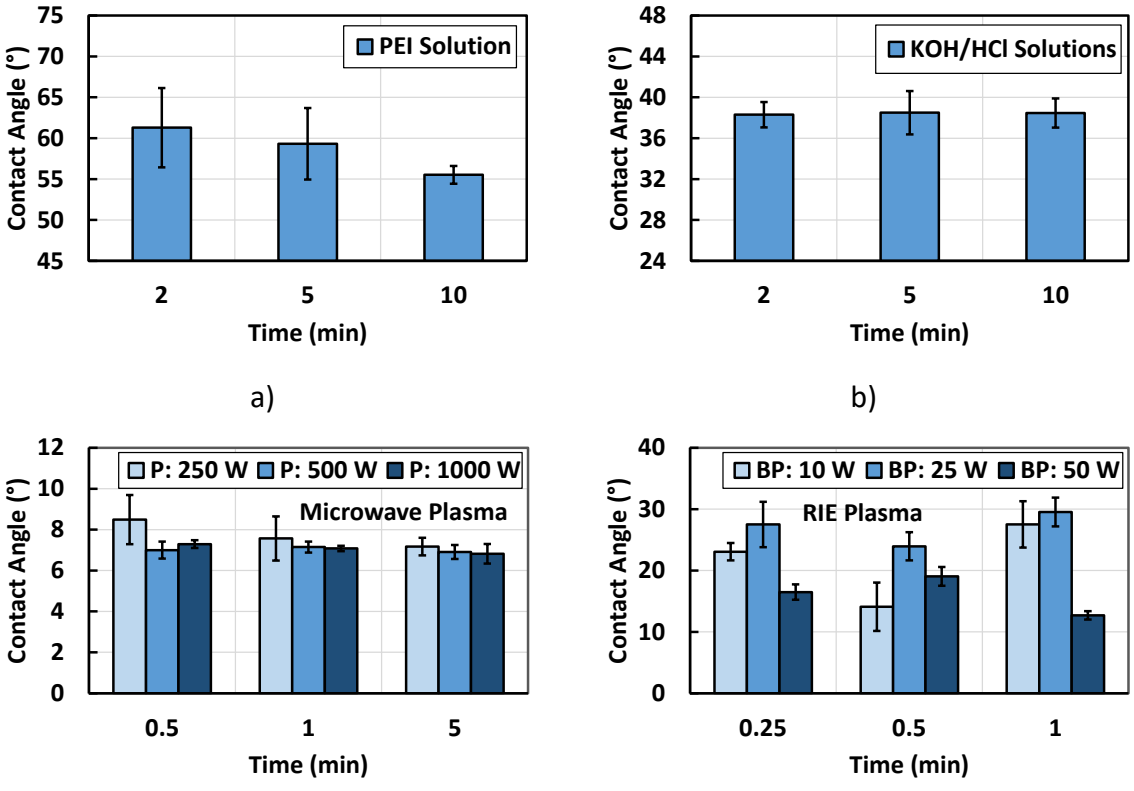

Fig. 2.5 Average water contact angle of treated PI films. a) PEI solution. B)KOH/HCl solutions. C) Microwave plasma. D) RIE plasma.

The selected treatment conditions, which produced the lowest contact angles, were further evaluated to see changes in surface energy and adhesion enhancement of PI films. The treatment conditions for further experiments are presented in Table 2.3.

An additional stability evaluation of the treated surfaces was also performed with a set of PI films treated with selected conditions (Table 2.3). The water contact angle was measured for 14 days, showing that all the samples increased their contact angle in the first few days. Details can be found in Appendix A.

Table 2.3 Selected treatment conditions for further testing.

Treatment	**Conditions**
PEI Solution	T = 70 ◦C, t = 10 min
KOH + HCl Solutions	KOH: T = 50 ◦C, t = 10 min
Microwave Oxygen Plasma	P = 1000 W, t = 5 min
RIE Oxygen Plasma	BP = 50 W, t = 1 min

2.5 Surface Energy of Treated Polyimide

An increase in the PI surface was expected after the proposed surface treatments, which is likely to be related to an improvement in the adhesion of the PI layers. The computation of the surface energy was obtained from the contact angle of films using three solvents: deionized water, dimethyl sulfoxide (DMSO) and isopropanol.

The surface energy (γ) has a polar (γ^P) and a dispersive component (γ^D), which are related to the contact angle by the Owens-Wendt equation [51], which in its linear form is defined as

$$0.5\gamma_L(1 + \cos\theta)/(\gamma_L^P)^{1/2} = (\gamma_S^D)^{1/2}(\gamma_L^D/\gamma_L^P)^{1/2} + (\gamma_S^P)^{1/2} \qquad \text{Eq. 2.1}$$

where θ is the contact angle of the liquid drop, γ_L is the total surface tension of the liquid, γ_L^P and γ_L^D are the polar and dispersive components, respectively. In the case of the surface energy of the polymer film, γ_S^D is its dispersive component and the polar component is represented as γ_S^P. Since the values of γ_L, γ_L^P, and γ_L^D are reported in the literature, at least two liquids need to be used to determine the energy components for the PI films (γ_S, = γ_S^P + γ_S^D). The known data of the proposed liquids are listed in Table 2.4.

Table 2.4 Surface energy and components of proposed solvents [52–54].

Liquid	γ_L (mN/m)	γ_L^P (mN/m)	γ_L^D (mN/m)
DI Water	72.8	51.0	21.8
DMSO	44.0	8.0	36.0
Isopropanol	23.0	3.5	19.5

For the computation of the unknown surface energies in Eq. 2.1, it was plotted as a linear function y = mx + b, being $y = 0.5\gamma_L (1 + \cos\theta)/(\gamma_L^P)^{1/2}$ and $x = (\gamma_L^D/\gamma_L^P)^{1/2}$. Then, a linear fitting to the data generated the slope value $m = (\gamma_S^D)^{1/2}$ and an intercept $b = (\gamma_S^P)^{1/2}$.

The extracted values of surface energy (γ_S) of PI, including the polar (γ_S^P) and dispersive (γ_S^D) components, are plotted in Fig. 2.6. The surface energy of untreated PI films was γ_S = 37.6 mN/m, the polar component was γ_S^P = 22.7 mN/m and its dispersive component γ_S^D = 14.8 mN/m. After treatments, all samples exhibited a reduction of the dispersive component and their polar component was increased. The lowest surface energy (γ_S = 48.1 mN/m) was observed for films with the treatment based on PEI solution, which was followed by the KOH/HCl solutions treatment, γ_S = 65.4 mN/m. The highest surface energy was produced with microwave plasma (γ_S = 87.3 mN/m), while the second highest surface energy was for the RIE plasma treatment (γ_S = 84.7 mN/m). The increment of surface energy produced by plasma treatments was around 2.3 times the values of the PI films without treatments.

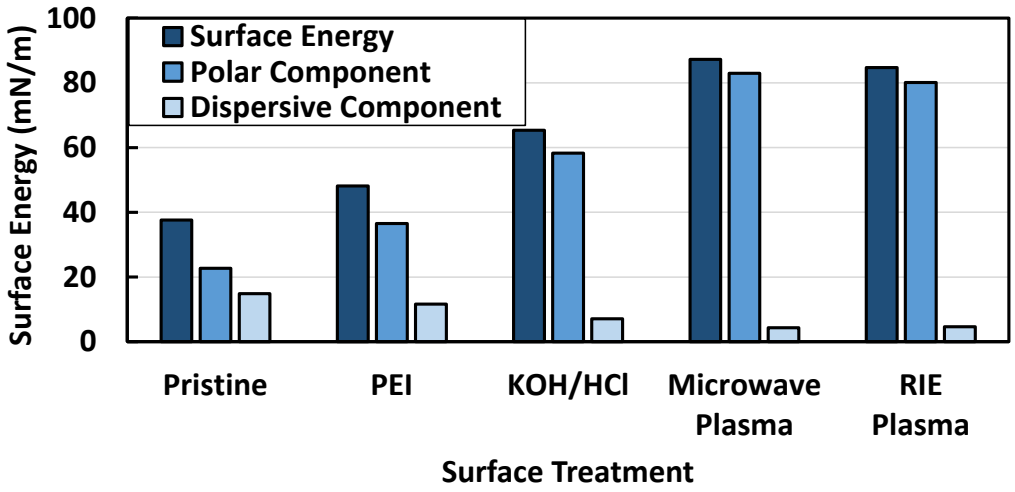

Fig. 2.6 Surface energy of pristine and treated PI films.

2.6 Adhesion Strength of Treated PI Films

For a quantitative evaluation of adhesion between treated PI films, a 180° peel test was proposed. For such evaluation, specific samples were produced using a first PI layer (5 µm thick) on a silicon wafer, previously coated with APTES. The PI layer was gold-sputtered (100 nm thick) and coated with AZ1518 photoresist (1.8 µm thickness) for its etching with iodine solution. This produced a gold rectangle of 40 by 5 mm, which is aimed to start the peeling process of the second PI layer due to the poor adhesion of the PI layer on gold.

Once the gold layer was structured, the PI surface was modified using one of the four selected treatments shown in Table 2.3. The second PI layer was applied, but using lower RPM (1000 RPM) for 60 s to produce layers close to 10 µm thickness. This second layer was also thermally cured and structured with a 20 µm thick photoresist AZ9260. The top PI layer was etched using O_2/CF_4 gas by RIE and the photoresist was removed with AZ 100 Remover. The result were six PI rectangle structures (70 mm length and 5 mm width) for each wafer. Two wafers per treatment and two reference wafers (pristine PI) were produced.

After fabrication of the samples, the wafers were diced to fit in a wafer holder, which was then later fixed to the Condor 100 XYZTEC bond tester. The PI film on top of the gold structure was initially peeled manually from the wafer using small tweezers. This released section of the PI was then fixed to a small custom gripper (Appendix C) also fixed to the bond tester. The schema of the structuring samples for the 180° peel test is shown in Fig. 2.7.

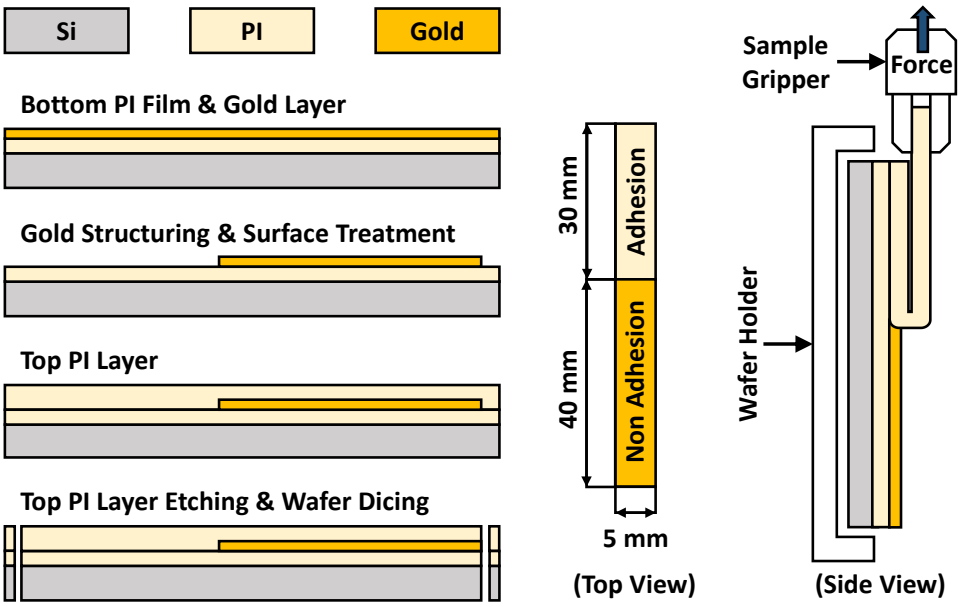

Fig. 2.7 Schema of structuring of samples for the 180° peel test.

The samples were placed in the bond tester with a pull cell of 100 N, with testing parameters set as a crosshead speed of 500 µm/s and a displacement of 50 mm. The peel force was obtained by fitting a constant value to the stable force region of each run. This force value was then divided by the sample width (5 mm) to obtain the peel strength in N/mm. A picture of the experimental setup with an actual sample is presented in Fig. 2.8.

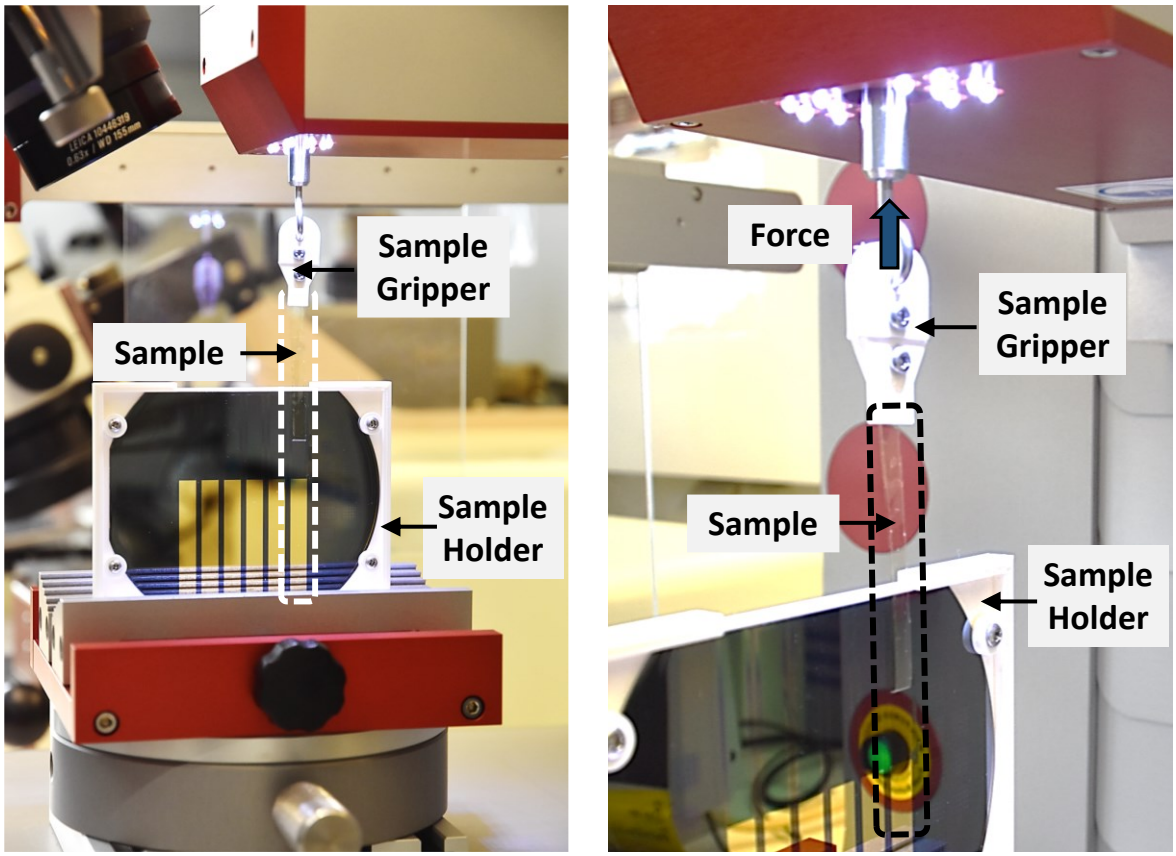

Fig. 2.8 Experimental setup for peel test of PI films.

The average peel strength of reference PI films was 22.7 mN/mm, which agrees with the peel strength range previously reported for this material [49,55]. The samples treated with PEI solution did not show an appreciable change in peel strength (22.4 mN/mm) in comparison with the pristine films, indicating no improvement of the material adhesion. On the other hand, the combination of KOH and HCl solutions produced a significant improvement of the material adhesion, as the force for peeling the samples was about 7 times the force (peel strength of 164 mN/mm) required by the pristine films.

Regarding the plasma treatments, the films modified with microwave plasma showed higher peel strength (29.3 mN/mm) in comparison to the reference samples, but it was only about a

29 % force improvement. Finally, the PI films treated with RIE plasma were not peeled as the applied force was above the mechanical resistance of PI films. This result agrees with the results from Ree et al. [56]. It also indicated that the treatment with RIE plasma is the best procedure for the adhesion of the PI layers. The average values of peel strength of the peelable samples are shown in Fig. 2.9a, and the representative force measurements are presented in Fig. 2.9b.

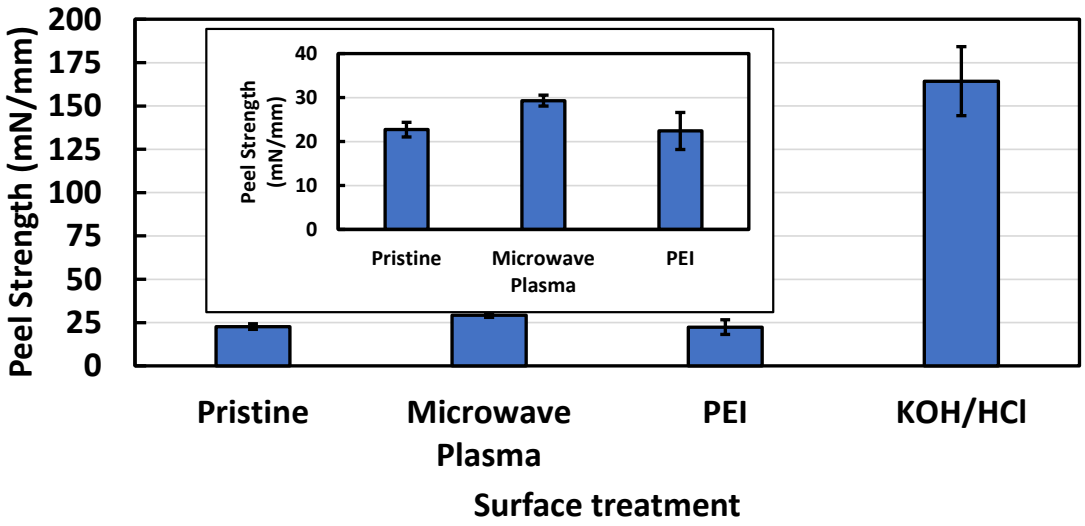

a)

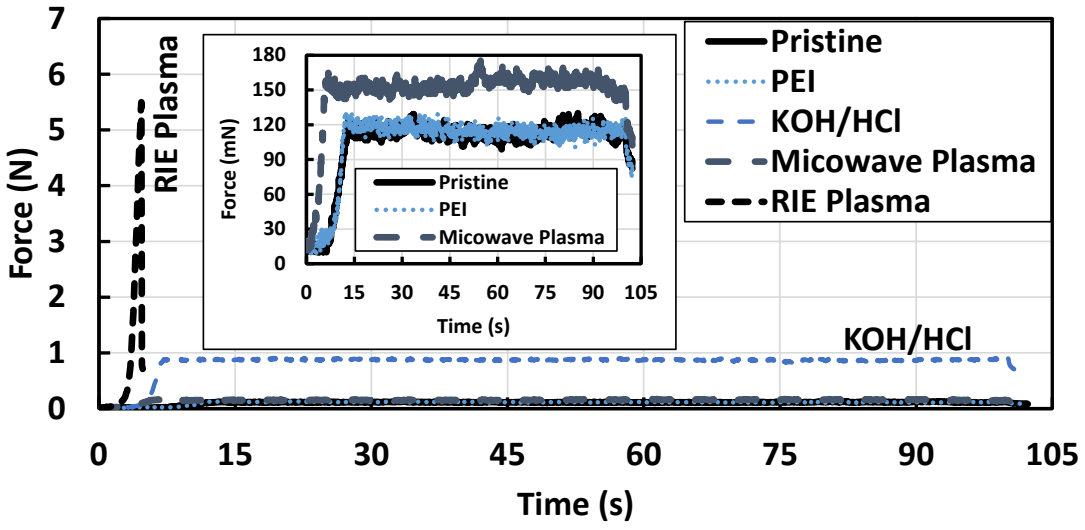

b)

Fig. 2.9 Results of peel test for PI films. a) Average peel strength of samples. B) Representative force plots during the test.

In addition to the presented 180° peel test, a scratch test was proposed for the two-layered PI samples as an alternative characterization. The top PI layer was structured as circles with a diameter of 750 µm, and they were manually scraped with a needle. Although this test was rather qualitative, it provided quicker information about PI adhesion since it does not require a gold layer (see Appendix A).

Chapter 3: Modeling of CNT/PI Composites

The second part of this work was the fabrication of the piezoresistive films using a combination of CNTs and PI. To better understand this material, two models were proposed to predict its electrical behavior. The idea was to produce a simple representation of the material that can be implemented without requiring specialized software, i.e. finite element analysis software. Two modeling approaches were used, the first one based on an array of resistors and the second one on the Montecarlo method.

The results of the Montecarlo-based model were partially presented at the conference: M. Cen-Puc, M.G.V. Gleason, A. Schander, W. Lang, Online Cure Monitoring of Carbon Nanotube/Polyimide Films, in: 2022 IEEE Sensors, IEEE, Dallas, TX, USA, 2022: pp. 1–4.

3.1 Parallel Resistors Model and Rule of Mixtures

This first model was inspired by the models used for the prediction of the mechanical properties of fiber polymer composites [13,14]. The representative element of the model is a square prism with a side equal to the CNT length and a thickness equal to the CNT diameter as represented in Fig. 3.1. As a simplification, the CNTs are considered to be vertically aligned inside the representative element, allowing the computation of its electrical resistance as a circuit of parallel resistors R_{CNT} and R_{PI} for the CNTs and the polymer matrix, respectively.

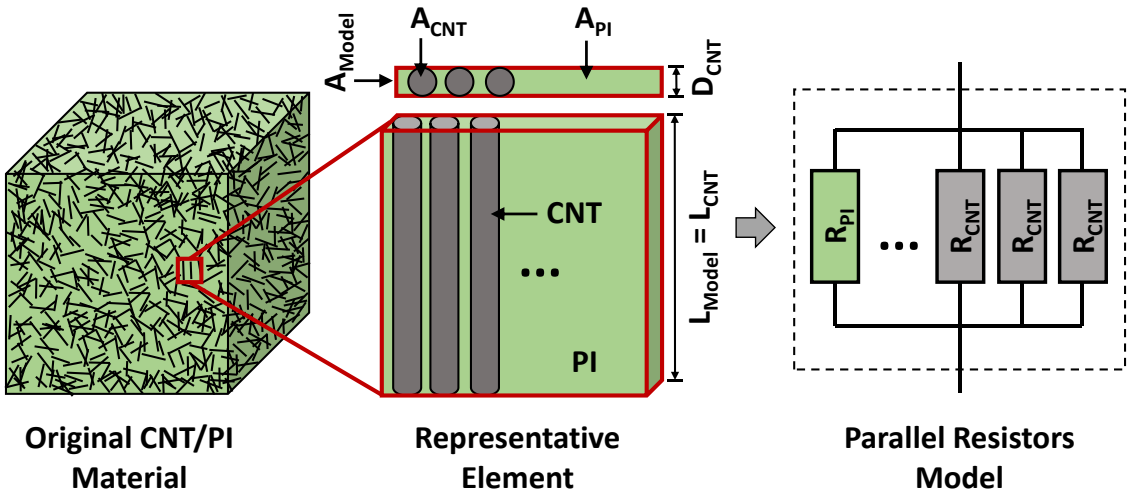

Fig. 3.1 Schema of the resistor Model for CNT/PI nanocomposites.

The weight fraction of CNTs for the model was obtained with the volume of the CNTs and their density (2100 kg/m^3 [57]). For the volume computations, each CNT was considered as a cylinder with a diameter D_{CNT} = 65 nm and length L_{CNT} = 6.5 µm.

In the case of the PI, the volume of the CNTs was subtracted from the model volume, and the mass of the PI was computed using a density of 1100 kg/m^3 [21]. The relationship between the mass of CNTs (m_{CNT}) and the mass of the PI (m_{PI}) gave the CNT content as a weight percentage (wt.%) using the expression:

$$f_{wt} = m_{CNT}/(m_{CNT} + m_{PI}) \qquad \text{Eq. 3.1}$$

In the model, the electrical resistance of a single CNT was set as R_{CNT} = 100 kΩ [58]. For the resistance of the PI (R_{PI}), its cross-sectional area (A_{PI}) and the model length (L_{Model}) were used together with the polymer resistivity ρ_{PI} = 1x10^{14} Ωm [21]:

$$R_{PI} = (\rho_{PI} L_{Model})/A_{PI} \qquad \text{Eq. 3.2}$$

The values of electrical conductivity for the model (κ_{Model}) were computed using the total resistance of the model (R_{Model}) obtained from the parallel resistor circuit, the cross-sectional area A_{Model} and the length L_{Model}:

$$\kappa_{Model} = L_{Model}/(R_{Model} A_{Model}) \qquad \text{Eq. 3.3}$$

The resistor model was implemented as an Excel file to obtain the data for electrical conductivity plotted in Fig. 3.2.

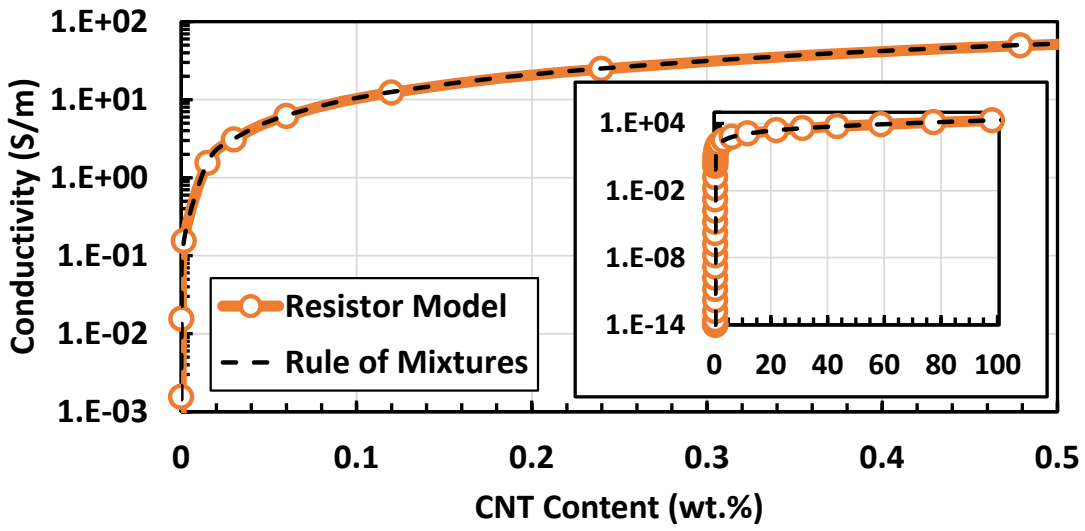

Fig. 3.2 Resistor model predictions for electrical conductivity of CNT/PI films.

The resistor model indicated an electrical conductivity of $\kappa = 1x10^{-14}$ S/m for a composite without CNTs, corresponding to an insulator material (see inset plot). If the CNT is increased, the predicted conductivity is steeply increased to the conductivity range of $\kappa = 1x10^{1}$ S/m for a CNT content of 0.1 wt.%, which can be considered in the range of semiconductors. After this transition zone, the electrical conductivity shows a slower increment to the range of $1x10^{4}$ S/m for a model with 100 wt.% CNT content, which is comparable to the electrical conductivity of graphite [59].

The resistor model can be further simplified as a standard rule of mixtures equation for electrical conductivity. Since the model does not consider any CNT misalignment, particle agglomerations, or contact resistance, the conductivity of the model can be represented as the direct relationship between particle filler and the polymer [13]. For this rule of mixture, one section of the material containing a single CNT only is considered as shown in the schema of Fig. 3.3. The geometry element has a length of L, the CNT cross-sectional area is represented as A_{CNT}, while the PI is represented by A_{PI}.

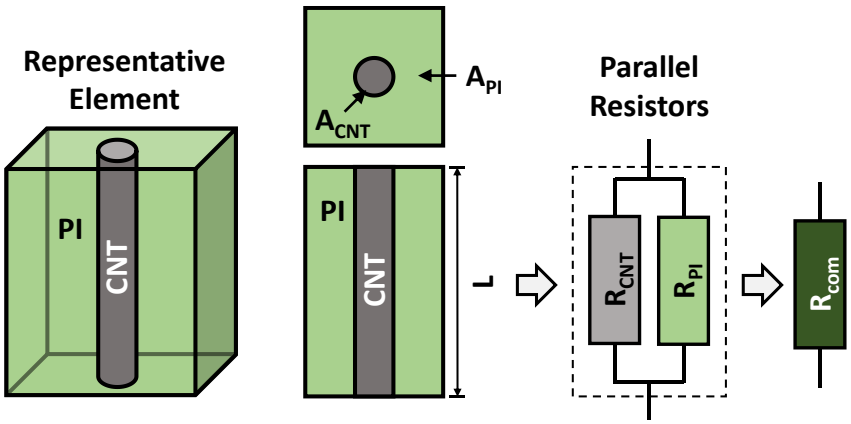

Fig. 3.3 Schema for the formulation of the rule of mixtures.

The electrical resistance of the model is the combination of one resistor for the CNT (R_{CNT}) and a second one for the PI (R_{PI}) connected in parallel, being the equivalent electrical resistor:

$$1/R_{com} = (1/R_{CNT}) + (1/R_{PI}) \qquad \text{Eq. 3.4}$$

The value of each resistor can be calculated as:

$$R_{CNT} = \rho_{CNT} L/A_{CNT}$$
$$R_{PI} = \rho_{PI} L/A_{PI} \qquad \text{Eq. 3.5a-b}$$

After the substitution of Eq. 3.5a-b in Eq. 3.4, the expression can be re-written in terms of the electrical conductivities (κ) of the materials:

$$1/R_{com} = (1/L)[\, A_{CNT}/\rho_{CNT} + A_{PI}/\rho_{PI}\,] = (1/L)[\, A_{CNT}\kappa_{CNT} + A_{PI}\kappa_{PI}\,] \quad \text{Eq. 3.6}$$

The electrical conductivity of the model (κ_{com}) can be obtained from its resistance R_{com}, the model length L, and the model cross-sectional area $A_{com} = A_{CNT} + A_{PI}$:

$$K_{com} = (1/R_{com})(L/A_{com}) \quad \text{Eq. 3.7}$$

Therefore, the combination of Eq. 3.6 and Eq. 3.7 produced:

$$K_{com} = (A_{CNT}/A_{com})\kappa_{CNT} + (A_{PI}/A_{com})\kappa_{PI} \quad \text{Eq. 3.8}$$

If each cross-sectional area of the Eq. 3.8 is now multiplied by the model length, the model conductivity can be described by the relationship between the particle content (volume fraction) and the electrical conductivities of the model constituents:

$$K_{com} = \kappa_{CNT}v_{CNT} + \kappa_{PI}(1 - v_{CNT}) \quad \text{Eq. 3.9}$$

where v_{CNT} is the volume fraction of the CNT in the model. The volume fraction of the PI (v_{PI}) was replaced by the relationship $v_{PI} = 1 - v_{CNT}$. This expression can be easily converted into a function of the weight fraction (wt.%) by considering the densities of the materials.

To show the agreement between the resistor model and the rule of mixtures (Eq. 3.9), a conductivity of $\kappa_{CNT} = 2\text{x}10^4$ S/m was used to produce the plot in Fig. 3.2. This conductivity was taken from the output of the resistor model. The curves in the Fig. 3.2 overlapped, indicating that the Eq. 3.9 can be used to describe the relationship between electrical conductivities of the resistor model.

The resistor model (and the rule of mixtures) can give a general idea about the expected electrical conductivity of the CNT/PI material. The model predictions suggested that CNT contents above 0.2 wt.% may be enough to produce the nanocomposite materials, with an electrical conductivity several orders of magnitude above the insulation of the polymer matrix. This outcome agrees with the reported data (Appendix B) about CNT/PI composites, as a percolation threshold for such material combination can be reached with CNT concentrations below 1 wt.% [29,31].

Unfortunately, the percolation threshold itself cannot be extracted from the resistor model since this type of model is not particularly good for particulate composites at low

concentrations. For the prediction of the percolation threshold, another model based on Montecarlo is presented in the following section.

3.2 Montecarlo Model

For the prediction of the percolation threshold of the CNT/PI composites, a 2D model was developed using the Montecarlo method. This method has been widely used for modeling the conductivity of nanocomposite materials [60–65]. However, this version of the model only computes the probability of CNT connection as a function of the CNT content.

Unlike the resistor model, the Montecarlo-based model considered the random orientation of the CNTs. To minimize the effect of CNT intersections [60,61], the model considers a square prism as a representative element, with a thickness of 2 times the diameter of the CNTs, allowing their overlapping. In the Fig. 3.4, the model is represented for the case of 2 CNTs with a low and a high concentration of CNTs, which leads to a case with low and high connection probability, respectively. The first version of the model considered only 2 CNTs, but it was later expanded to more nanoparticles.

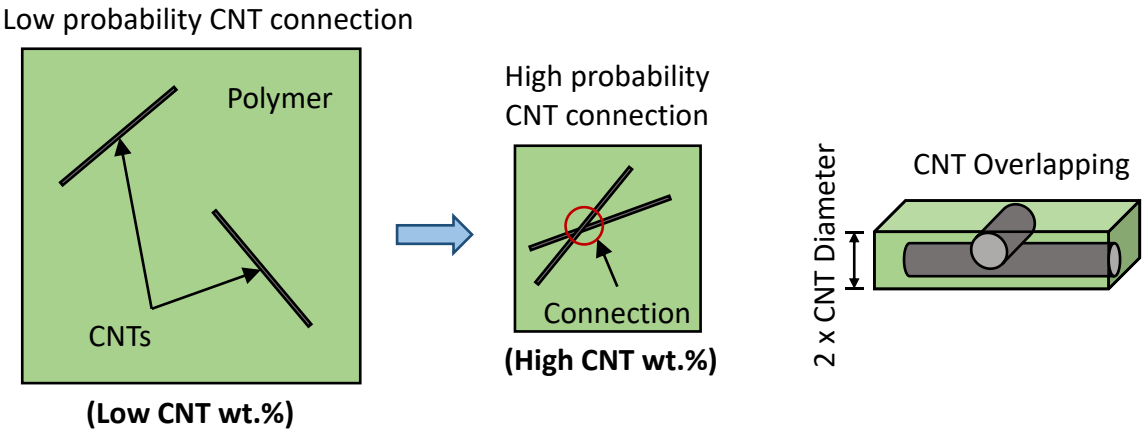

Fig. 3.4 Representation of the Montecarlo model for CNT/PI composites.

The model was developed in the MATLAB software, following the summarized algorithm in Fig. 3.6. The model starts with the definition of the number of nanoparticles and the CNT content (wt.%). The volume of the CNTs was computed considering them as cylinders with an average diameter D_{CNT} = 65 nm and length L_{CNT} = 6.5 µm. Then the mass of the CNTs was obtained using a density of 2100 kg/m^3 [57], allowing the computation of the mass for the PI required for that CNT content. The area of the model was obtained by adding the volume of

the PI (density of 1100 kg/m^3 [21]) to the volume of CNTs, and the total volume was then divided by the model thickness.

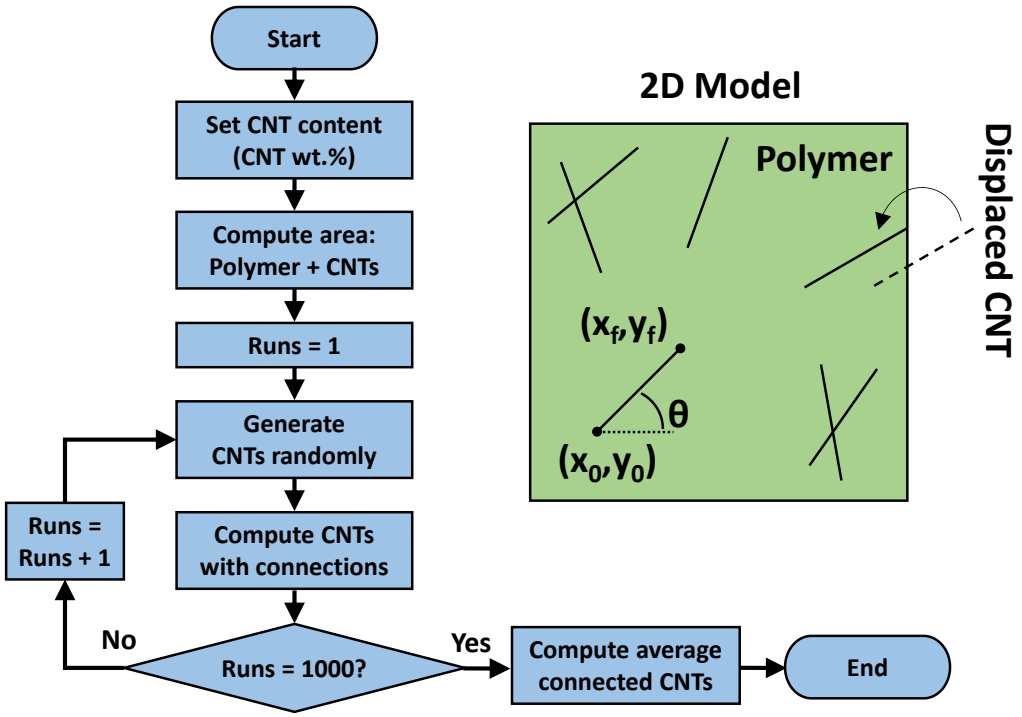

Fig. 3.5 Summarized algorithm of the Montecarlo-based model.

After defining the model area, each CNT is randomly generated with an initial coordinate point of the line (x_0, y_0) and a random angle orientation θ from 0° to 360°. The final point of the CNT is computed using its length and the orientation angle as $x_f = L_{CNT}Cos\theta + x_0$ and $y_f = L_{CNT}Sin\theta + y_0$. To avoid the generation of CNTs outside the model, the CNTs are shifted if necessary.

On each run, each CNT was checked to determine if there was another nanoparticle connected to it. This process was repeated for 1000 runs to compute the probability of CNT connections. The connection probability was obtained by dividing the number of times the nanoparticles had a connection by the total number of runs.

3.2.a Convergence Analysis for Montecarlo Modeling

A convergence analysis was performed to evaluate the effect of the number of runs and the number of CNTs on the output of the model. In this evaluation, contents of 0.1 and 1 wt.% CNT were considered. The model had as a parameter variation the number of CNTs as n_{CNT} = 2, 10, 100 and 1000 CNTs, for a total of 10000 runs.

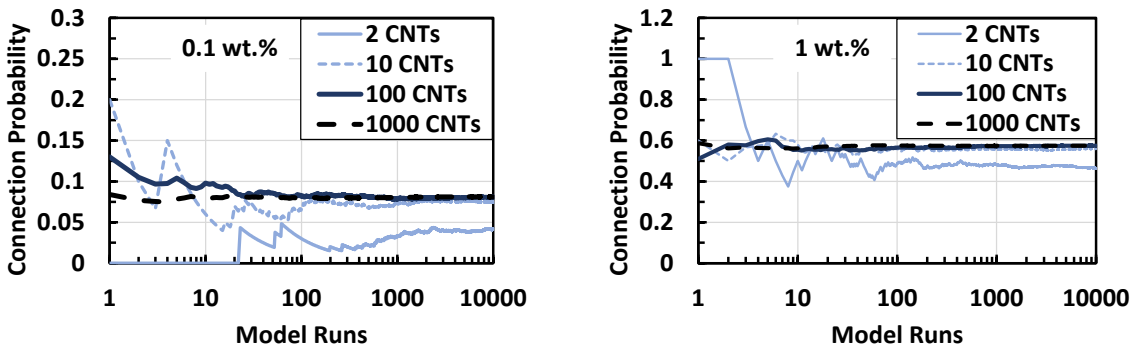

a) b)

Fig. 3.6 Convergence of the connections probability of CNTs. a) Simulations for a model with 0.1 wt.%. b) simulations for a 1 wt.%.

The model output for a condition of n_{CNT} = 2 CNTs and 0.1 wt.% (Fig. 3.6a) showed that a fairly stable output was achieved only after 2000 runs. However, if the model has more CNTs, the number of runs is significantly reduced, being approximately 100 runs for 10 CNTs, 20 runs for 100 CNTs, and only 10 runs for a model with 1000 CNTs. Another important outcome is that the models with 10 CNTs or more tended to reach the same connection probability (close to 0.08) after 10000 runs, while the model with only 2 CNTs reached only half of that value.

In the case of a model with 1 wt.% CNTs (Fig. 3.6b), it was noticed that a model with 2 CNTs provides again a lower stable output (0.47) in comparison with more CNTs (0.57). The model with only 2 CNTs requires more than 100 runs to achieve a stable output in comparison to the 10 runs for models with 100 or 1000 CNTs. Taking into consideration these results, the Montecarlo-based model was configured with 100 CNTs and 1000 runs in order to save computing time at all concentrations.

3.2.b Results of the Montecarlo Model

The predictions of the Montecarlo model are plotted in Fig. 3.7. For a better visualization, the plot has a logarithmic scale for CNT content. Examples of the 2D generated models are also included for some CNT loadings (0.1, 1 and 3 wt.%).

The model predictions show a nonlinear increase in the connection probability. For contents below 0.01 wt.%, the connection probability is close to zero. However, this probability is noticeably increased for particle concentrations above 0.1 wt.%. The connection probability reaches a value of 0.9 at 3 wt.%, and it saturates at around 5 wt.%.

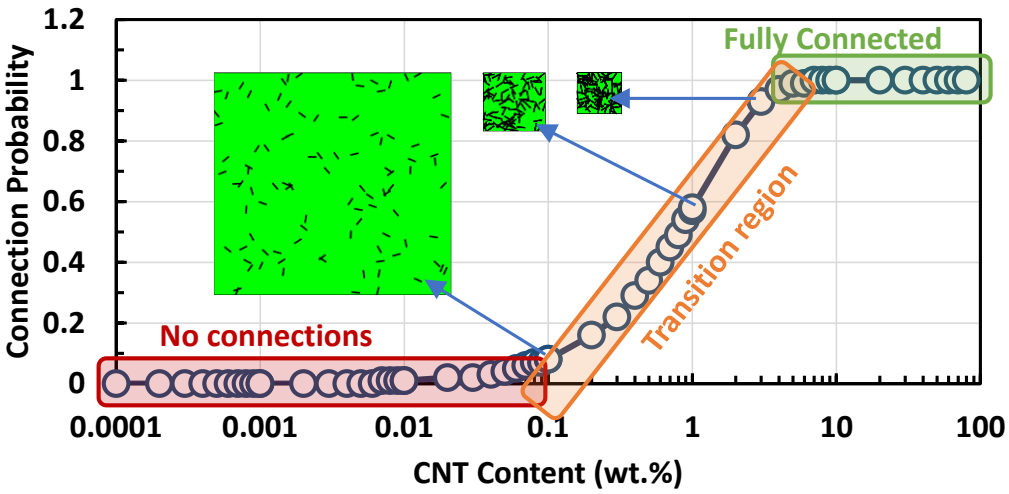

Fig. 3.7 Montecarlo predictions for the connection probability of nanoparticles.

The results resembled a typical electrical percolation behavior of polymer materials loaded with electrically conductive particles [66–69], showing the three regions of the percolation theory. In the first one, there is a large separation between the particles due to their low concentration, and the material behaves as an electrical insulator due to the low particle connections. The second section of the plot is the transition region where the particles start to form a network inside the polymer matrix and the composite exhibits an abrupt change in its electrical conductivity. The last region describes a composite state where the particles are fully connected, and the conductivity of the composite reaches a plateau.

The proposed Montecarlo model did not consider other features like particle agglomerations or computation of the electrical resistance. However, it provided a hint about the CNT content range for the fabrication of electrically conductive polymer films.

For the next steps, which focused on the fabrication of the nanocomposite films and their characterization, the range of CNT concentration of 0.1 wt.% up to 10 wt.% was selected based on the results of the Montecarlo model. Subsequent electrical measurements of the material (Chapter 6) showed qualitative agreement with the predictions.

Chapter 4: Fabrication of Polymer Nanocomposite Films

For the project, a piezoresistive nanocomposite film was proposed as material for the fabrication of strain sensors. The film was based on a combination of CNTs and PI, trying to use the lowest amount of nanoparticles to keep the structuring parameters of the layer close to those for pristine PI films.

The CNTs were chosen as fillers due to their high aspect ratio (length/diameter), which allows the use of amounts around 1 wt% [29] to produce electrically conductive polymers. This particle content is considerably lower than the amount required by other particles like carbon black (5 wt.% to 20 wt.%) [70–72] to produce electrically conductive mixtures.

The main challenge during the manufacture of CNT/polymer composites is to achieve a proper dispersion of the CNTs, which can highly influence the percolation threshold of the polymer composites [31]. For this purpose, different methods can be used depending on the nature of the polymer and the available laboratory facilities [73–76].

Ultrasonication is widely used to disperse CNTs into liquids with low viscosity. The polymer is diluted before adding the CNTs, and ultrasonication waves are applied with an ultrasonication bath or a probe. In this method, the main limitations are the toxicity of the solvents and the difficulty in removing them from the mixture. In addition, this process can produce heat and CNT breakage.

Another approach is calendaring, where a machine with three roll mills disperses the particles in a viscous material. The narrow gaps between the rolls and the mismatch of their angular velocity produce shear forces to disperse the nanoparticles. However, limitations of the gap between the mills (a few μm) can limit the reduction of agglomerate sizes.

A third method is ball milling, typically used to grind materials into fine powders. The collision between rigid balls produces high pressure, which generates particles as small as 100 nm. However, the particles can be broken or change their structure.

Mechanical stirring is used to disperse particles in liquid materials. Several parameters, such as the mixing time, speed, size and propeller type influence the material dispersion. There are

some limitations regarding this approach, for example, high shear forces are needed for dispersion and the particles can re-agglomerate after some time.

Polymer extrusion is a method in which the polymer is molten for its mixing inside a polymer extruder. The machine has twin crews that rotate to produce shear forces to disperse the nanoparticles. However, the shear forces can lead to a degradation of the polymer.

In this work, ultrasonication with solvent and mechanical stirring were evaluated for the fabrication of CNT/PI films. This chapter was partially published in a conference as: M. Cen-Puc, T. De Rijk, M.V. Gleason, W. Lang, Carbon Nanotubes/Polymer Films for Microsensors Applications, in: 2021 IEEE Sensors, IEEE, Sydney, Australia, 2021: pp. 1–4.

4.1 Ultrasonication Dispersion of CNTs with PI

Most of the published works on CNT/PI films are based on ultrasonication for the dispersion of the CNTs as seen in Table B.1 in Appendix B. Hence, ultrasonication was proposed as the first approach for the fabrication of CNT/PI films.

A solubility test for the PI was performed to find suitable solvents considering the available materials at the institute: isopropanol, acetone, N-Methyl-2-pyrrolidon (NMP) and DMSO. An amount of 5 gr PI precursor was placed in a glass beaker with 1 ml solvent and allowed to stand for 4 h at room temperature. The experiment showed that the isopropanol produced the precipitation of the PI instead of diluting it, and in the case of acetone, a partial dilution was obtained. On the other hand, the samples with NMP and DMSO diluted the polymer. However, the NMP was discarded due to the health risks involved, leaving the DMSO as the solvent for fabricating the polymer nanocomposites.

For the fabrication of films, 10 gr of the PI precursor with a nanoparticle concentration of 1 wt.% were proposed. The CNTs were multiwalled nanotubes (Sigma-Aldrich Chemie GmbH) with a purity >95 % and were used as received. The amount of CNTs per mixture was computed by considering a polyamic acid content of 18 wt.%. This CNT concentration was expected to be above the percolation threshold of the material according to the model predictions and the literature data [29–31].

Different parameters for the dispersion of the CNTs, such as the solvent amount and ultrasonication times, were considered during the material mixture. Those variations of the ultrasonication method were sorted into four groups according to the mixing order: US1, US2, US3 and US4. These mixing variations are described on the following pages.

Ultrasonication variation US1. The PI precursor was placed in a glass beaker with the DMSO and the CNTs. The amount of DMSO was varied from 2 ml up to 4 ml. The mixture was placed in an ultrasonication bath from ROAG, FASELEC AG. The beaker was sealed to avoid water entering the sample. The ultrasonication time ranged from 15 min up to 60 min, and after that, the mixture was spin-coated on a silicon wafer at 3000 RPM for 60 s. This layer was then thermally cured in a vacuum hot plate with a standard temperature program of the PI. Although PI films were produced, the nanoparticles were not dispersed as CNT clusters were observed. This process variant is represented in Fig. 4.1.

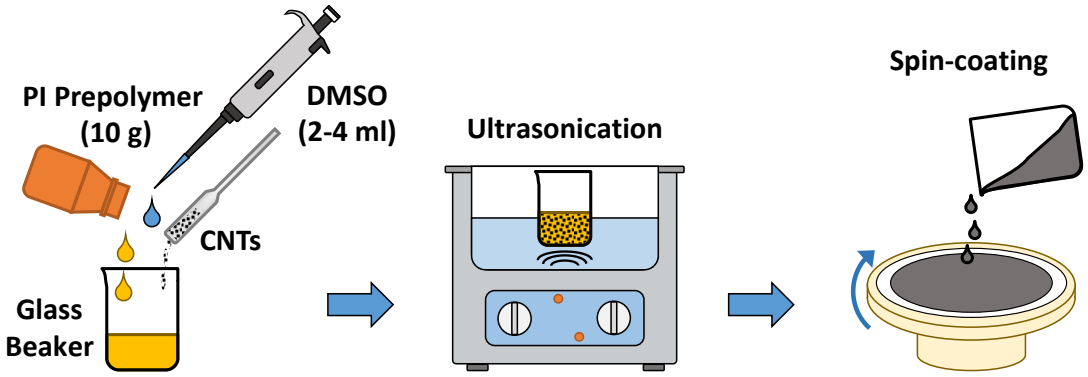

Fig. 4.1 Schema for CNT/PI mixing by method variation US1.

Ultrasonication variation US2. This method changed the order of the mixture, first diluting the PI precursor with the DMSO (ranging from 2 ml to 4 ml DMSO), while the ultrasonication ranged from 30 min up to 60 min. After the dilution of the PI, the CNTs were added, and the ultrasonication bath was used (from 30 min up to 60 min) for CNT dispersion. The mixture was spin-coated on a silicon wafer and thermally cured. In this method variation, a slight improvement of the CNT dispersion was observed. This suggested that the viscosity of the mixture was not adequate. This method variant is represented in Fig. 4.2.

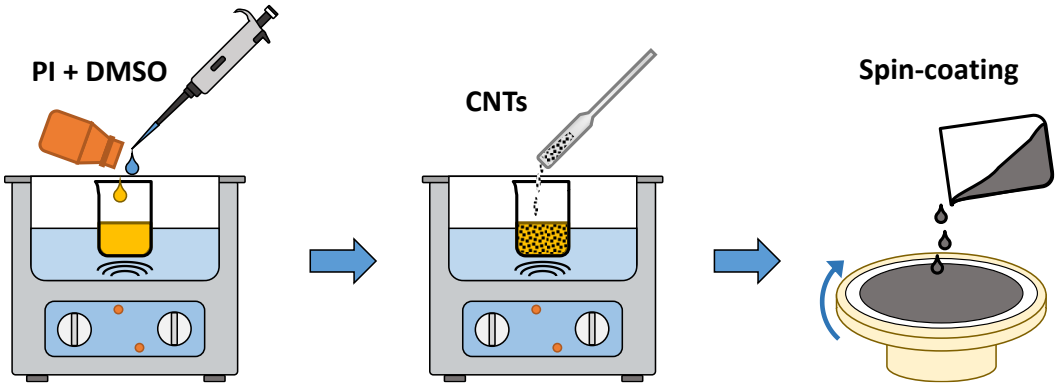

Fig. 4.2 Mixing of CNT/PI method variation US2.

Ultrasonication variation US3. The CNTs were dispersed in the DMSO (5 ml to 8 ml) for 60 min using ultrasonication, and the PI precursor was added slowly while using ultrasonication for another 60 min (Fig. 4.3). After spin-coating and thermal curing, the CNTs were dispersed in the PI. This indicated that a first dispersion of the CNTs using a minimum amount of 5 ml solvent for 10 gr PI precursors is required. However, the films could not be produced due to the amount of solvent used for the mixture.

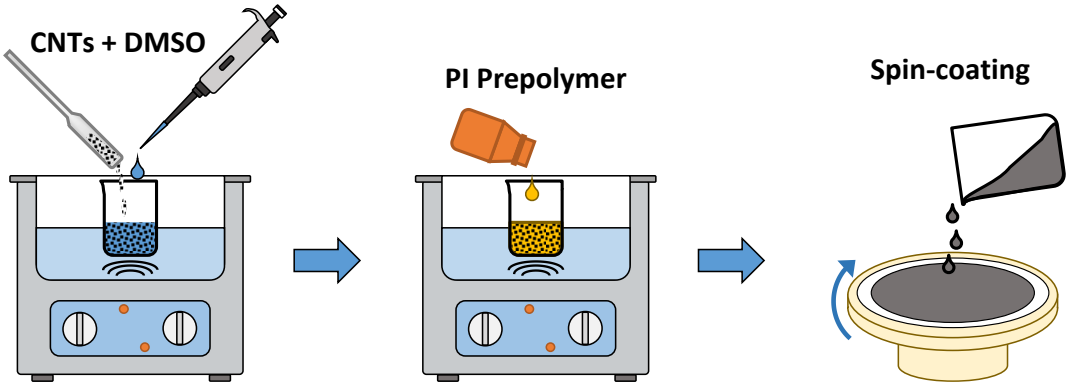

Fig. 4.3 Proposed CNT/PI mixing variation US3.

Ultrasonication variation US4. The DMSO was combined with acetone due to their miscibility [77,78] using a mixture ratio of 1:1. The acetone was proposed to be removed before the spin coating since its evaporation occurs at 56 °C, which is considerably below the temperatures for evaporation of the DMSO or curing of the PI.

An amount of 10 ml solvent mixture was used to disperse the CNTs for 60 min by ultrasonication. The PI precursor was slowly added also with ultrasonication for 60 min. Afterwards, the mixture was heated at 120 °C (from 4 h to 12 h) while stirring at 200 RPM. (see Fig. 4.4). The mixture was spin-coated on a silicon wafer and thermally cured.

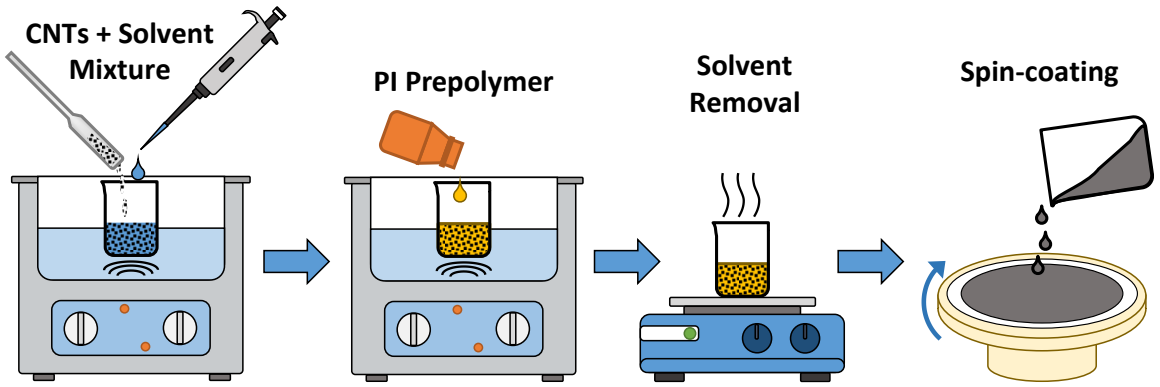

Fig. 4.4 Schema for CNT/PI mixing variation US4.

With this method variation, the CNTs were finally dispersed, although CNT clusters were observed. One limitation was the film thickness due to the remaining solvent since four layers were required for a thickness of 5 µm. The first layers were partially cured at 120 °C, and the full-curing cycle was used after the fourth layer. This last method variation produced the best results for the fabrication of the CNT/PI films by ultrasonication, and it was further tested for CNT amounts up to 3 wt.%. An overview of the results obtained by the variants of the ultrasonication-based dispersion is presented in Table 4.1.

Table 4.1. Variants of the solvent based dispersion of CNTs within PI.

Method variation	**Conditions**	**Results**
US1	10 g PI + 2 - 4 ml DMSO + CNT in UB, time = 15 - 60 min	PI films produced CNTs not dispersed
US2	20 g PI in 4 - 8 ml DMSO in UB time = 30 - 60 min Then + CNT in UB, time = 30 - 60 min	PI films produced CNTs slightly dispersed
US3	10 - 15 ml DMSO + CNT in UB, time = 60 min then + 20 g PI in UB, time = 60 min	PI films not produced CNTs dispersed
US4	5 ml DMSO + 5 ml acetone + CNT in UB time = 60 min then + 20 g PI in UB , time = 60 min then solvent evaporation 4 - 12 h at 120 °C	PI films produced Best CNT dispersion Required 4 - 5 layers.

The dispersion of the CNTs in samples was qualitatively inspected with pictures taken with a light microscope. Differences in the cluster size were observed depending on the method variation used for CNT dispersion (US1 to US4). The small agglomerates or particle clusters indicated a good CNT dispersion. Some samples with poor nanoparticle dispersion had clusters that could be seen with the naked eye.

Pictures of the samples were transformed into a grayscale format for easy viewing of the clusters; examples are presented in Fig. 4.5. The large photos were taken with a magnification of 50x, and the small ones were taken with a 2.5x magnification. In Fig. 4.5a, the film was produced with the method variation US1, where the CNTs, PI prepolymer and solvent were put together in the ultrasonication bath. The main characteristic of the samples is the large size of the CNT clusters, with almost no individual CNTs in the area between clusters.

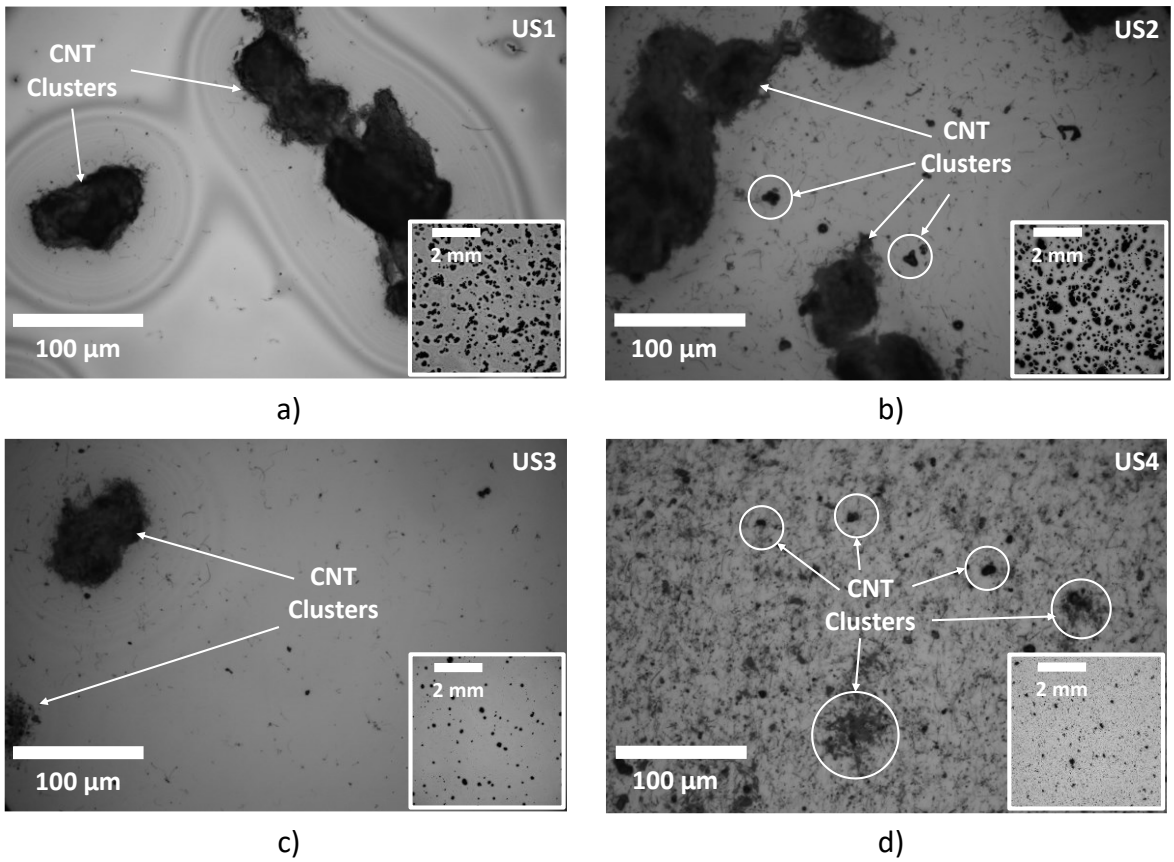

Fig. 4.5 Micrographs of films produced by ultrasonication method. a) Variation US1. b) Variation US2. c) Variation US3. d) Variation US4.

The second method variation US2 (Fig. 4.5b) consisted of the first dilution of the PI precursor before adding the CNTs. With this mixing order, the dispersion of the nanoparticles was

improved as individual CNTs can be found in the areas between clusters. However, larger clusters (>500 µm) were also observed in the films.

The third method variation US3 (Fig. 4.5c), where the CNTs were first dispersed in the solvent and then the PI was added, also showed individual CNTs within the polymer. Moreover, there was a reduction in the cluster size. However, the drawback is that films were not properly produced, as some areas of the wafer were not covered due to the amount of solvent.

Finally, the method variant US4 (Fig. 4.5d), which included a solvent mixture and partial evaporation, represented a remarkable improvement compared to the previous attempts. The cluster size was further reduced (below 300 µm), but more importantly, the CNTs were dispersed and can be found in the whole area of the film.

The dispersion effectiveness of the method variations was compared by taking the size of their CNT clusters. The cluster dimensions were obtained from sample pictures using the software ImageJ and the average cluster sizes are plotted in Fig. 4.6.

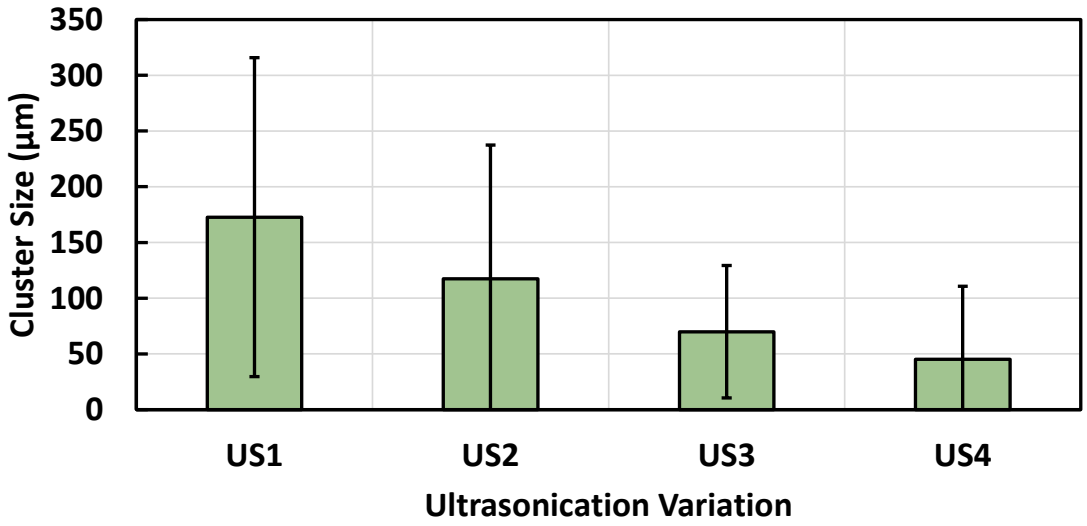

Fig. 4.6 Cluster size of the CNT/PI films produced by ultrasonication method.

All samples presented a wide dispersion of the cluster size. However, the smallest average cluster size was achieved by the variation method US4 (<50 µm), which, combined with the particle distribution all over the film, made it the best variation of the ultrasonication method.

4.2 Direct Mechanical Stirring of CNTs with PI

Usually, material melting is required for the direct mixing of the polymers with particles. However, the dispersion of CNTs may be produced in thermosetting polymers like epoxy resins before their curing [65]. For this approach, a mixing paddle was designed in CAD software and fabricated with a 3D printer using commercial polyactic acid (PLA), which can stand the mixing process. The paddle design had 2 blades with an angle of 45°, aimed to produce a combination of axial and radial flow of the mixture [79,80], which is desired for the dispersion of the CNTs and the mixture homogeneity (see Appendix D).

For this method, 15 gr PI precursor were poured into a glass beaker with an amount of 1 % wt. CNTs. The mixing blade was attached to an electric stirrer IKA RW 20n (IKA Works GmbH). After stirring, the material was placed in a vacuum chamber for 10 min to remove the trapped air. The polymer mixture was finally spin-coated on a silicon wafer for its thermal curing. The general process is depicted in Fig. 4.7.

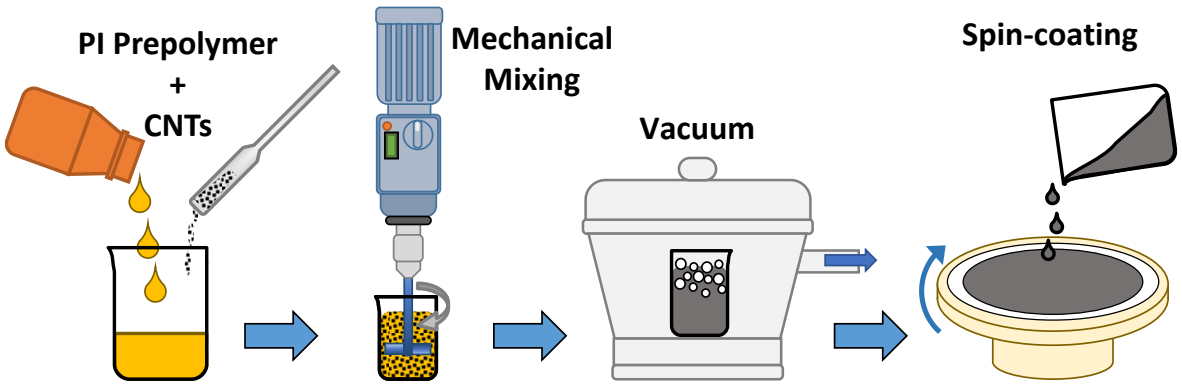

Fig. 4.7 Schema of the mixing steps by the direct mixing method.

For the optimization of the CNT dispersion, several mixing times and spinning speeds were evaluated. The combinations of the mixing parameters are listed in Table 4.2.

Table 4.2. Parameters for the direct mechanical mixing of CNT/PI.

Mixing spinning speed (RPM)	Mixing time (min)
240	2, 10, 30
600	2, 10, 30
1200	2, 10, 30

After optical inspection of the CNT/PI films, it was observed that all samples showed a distribution of the CNTs in the whole sample area and the clusters had a narrower size distribution, which is an improvement in comparison to the previous results by ultrasonication. Regarding the cluster size, larger clusters were observed at lower mixing RPMs and shorter mixing times. The cluster size was significantly reduced by increasing both the mixing time and RPMs of the stirrer.

Examples of the CNT/PI films are shown in Fig. 4.8, with large pictures taken at 50x magnification and small images at 5x magnification. The first picture (Fig. 4.8a) shows a film produced with a mixing speed of 240 RPMs and 2 min mixing, while Fig. 4.8b shows the results for the same mixing RPM, but for a 10 min mixing time. The third picture (Fig. 4.8c) shows a film mixed at 600 RPMs for only 2 min. The last picture (Fig. 4.8d) is a film mixed at 1200 RPMs for 2 min.

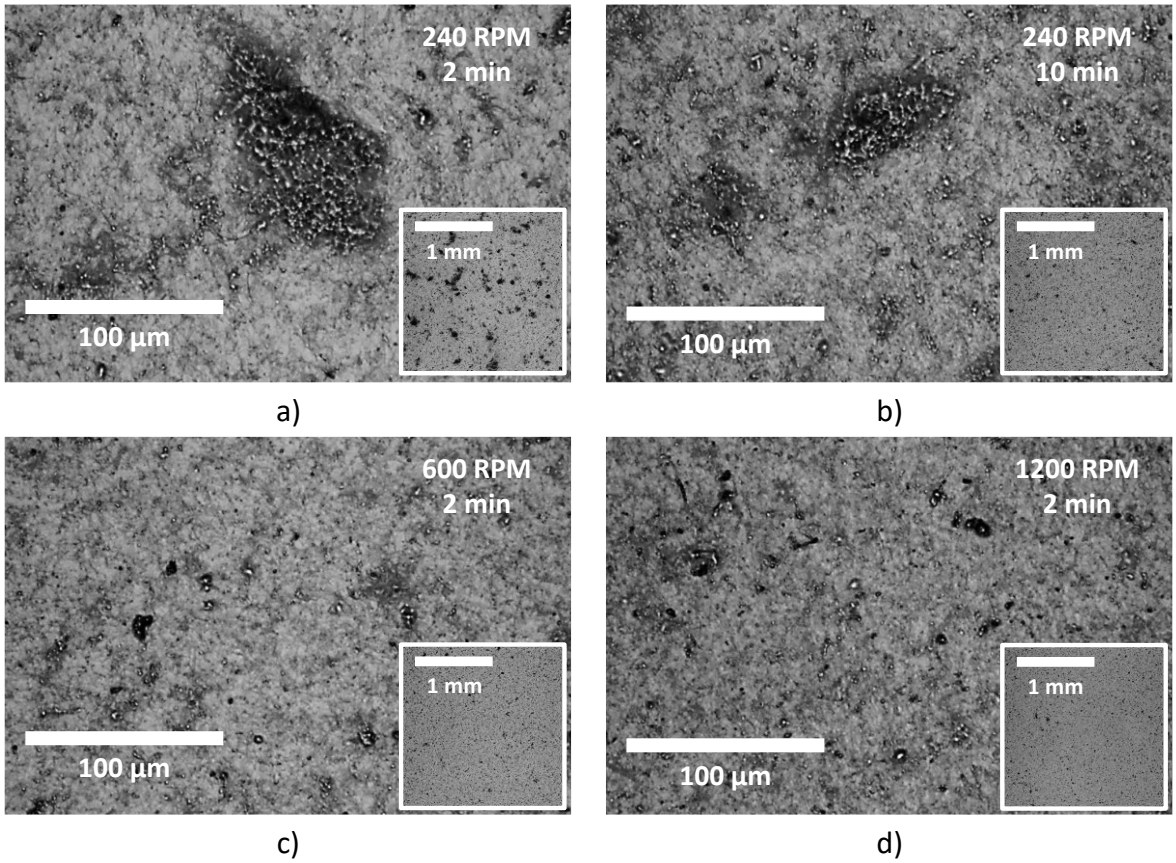

Fig. 4.8 Micrographs of CNT/PI films produced by the mechanical mixing. a) 240 RPM for 2 min. b) 240 RPM for 10 min. c) 600 RPM for 2 min. d) 1200 RPM for 2 min.

In the case of mixtures produced with higher RPMs, increasing the mixing times had a lower influence on the reduction of the cluster size. The clusters were measured from the micrographs using the software ImageJ. The average cluster size, depending on the mixing RPMs and time, is plotted in Fig. 4.9.

The largest clusters (120 µm) were observed when the lowest mixing speed (240 RPM) and shortest time (2 min) were combined. However, if the mixing time is increased to 10 min, the cluster size is reduced to half (63 µm), and if longer mixing times (30 min) are used, the cluster size is further reduced to 54 µm.

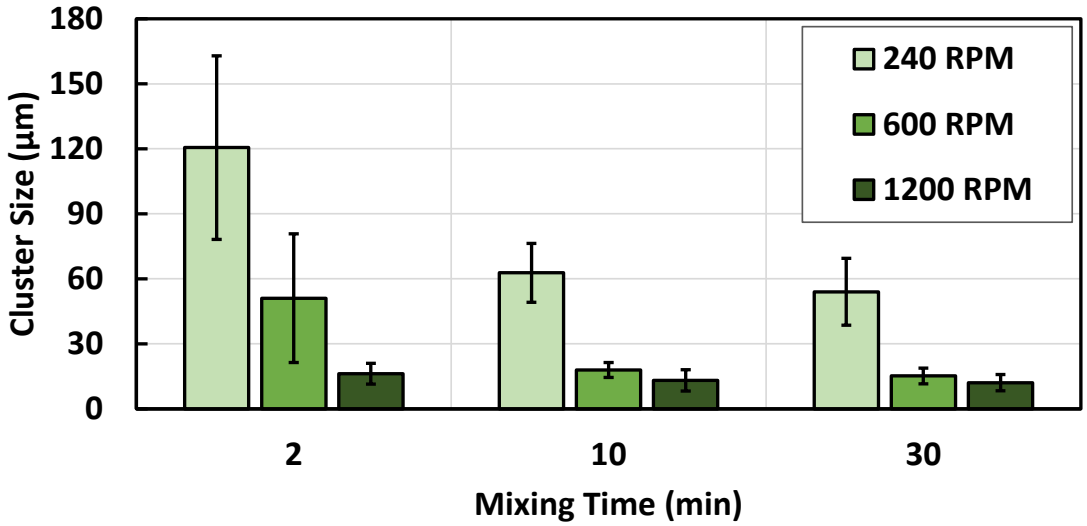

Fig. 4.9 Effect of the mixing speed and time on the cluster size of CNT/PI films.

When a higher mixing speed of 600 RPM is used for 2 min, the largest average cluster size was 51 µm. This indicates that increasing the mixing RPM is more effective for the dispersion of CNTs than longer mixing times. For this RPM condition, if the time is increased to 10 min, the clusters are reduced to 18 µm, while for longer times (30 min), the cluster size is reduced to 15 µm.

At the highest mixing speed of 1200 RPM, further reduction of the clusters was observed. The mixing for 2 min produced clusters of about 16 µm. However, the switching to longer mixing times did not lead to larger changes since the clusters were 13 µm and 12 µm for the mixing times of 10 min and 30 min, respectively. This suggests that the optimum mixing time is between 10 and 30 min, if a speed of 1200 RPM is used for mixing.

Given the improvement in the distribution of CNTs and the reduction of their cluster sizes in the films, the mechanical stirring was selected instead of the ultrasonication approach for further film fabrication. The chosen conditions were a mixing speed of 1200 RPM and a mixing time of 30 min, as they produced the smallest CNT clusters.

A comparison between fabrication methods is presented in Fig. 4.10. In both cases, a good distribution of the CNTs can be observed in the whole material area. The CNT clusters in the sample by mechanical mixing of Fig. 4.10a are about 15 µm (seen with a 50x magnification), and they are similar to the small clusters in the case of the ultrasonication-based film in Fig. 4.10b. However, when checking both films at 5x magnification, it is evident that the ultrasonication-based sample (Fig. 4.10b) has a considerably wider range of cluster size, being the larger ones around 200 µm. In contrast, the sample based on mechanical stirring showed a narrower size range of clusters, having smaller agglomerates.

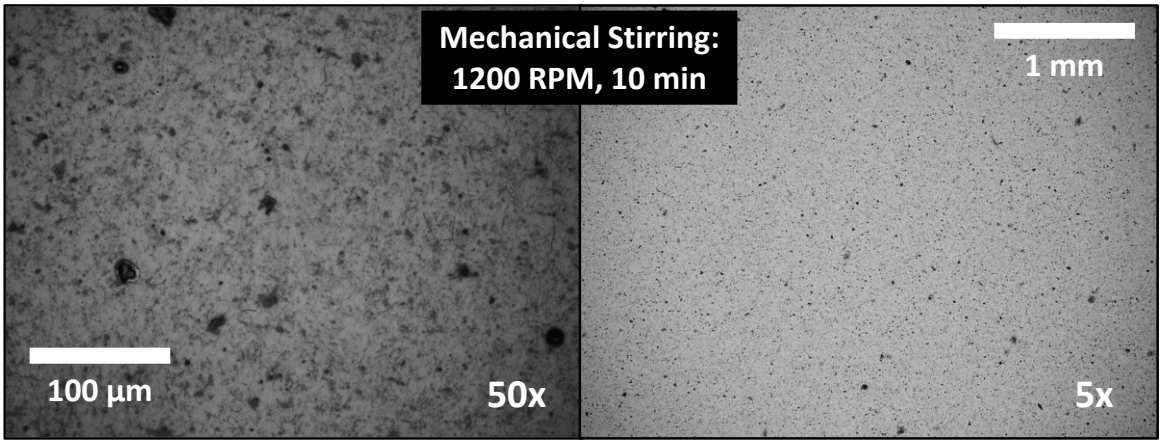

a)

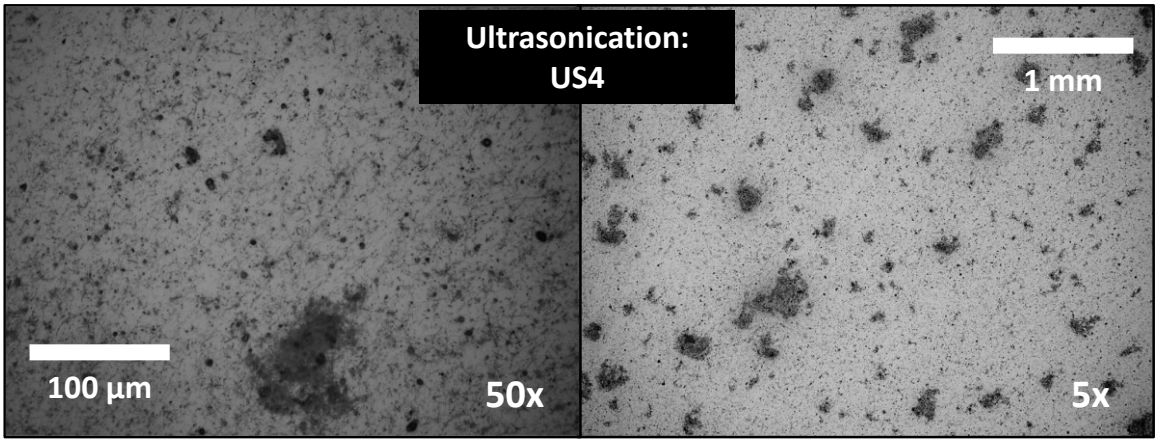

b)

Fig. 4.10 Comparison between dispersion methods for fabrication of CNT/PI films. a) Direct mechanical stirring. b) Ultrasonication-based method.

In addition to the smaller CNT clusters achieved by the mechanical stirring, this method presented further advantages. The first one is that solvent is not required since the viscosity of the PI precursor likely helps in the dispersion of CNTs due to the shear forces during the mixing. Another advantage is that the processing time is reduced because solvent removal or partial curing of the films is not required, as a single spin-coating produced films with a thickness of 5 μm, similar to the thickness of the pristine PI films.

Chapter 5: Fabrication Test for GNP/PI Films

Graphene has been reported as a promising nanomaterial to fabricate piezoresistive polymer nanocomposites [32]. For this work, this material was also tested for the fabrication of PI films. The commercially available material consists of stacks of graphene sheets [81] instead of a single layer, and they are called graphene nanoplatelets (GNP). Some characteristics of this material are a few nm thickness and a particle size below 2 µm. The GNPs were purchased from Sigma-Aldrich Chemie GmbH and used as received.

5.1 Fabrication of Films

Given the difficulties of working with solvents for the mixture of nanoparticles and the PI precursor, the GNP/PI films were produced by the direct mechanical mixing approach presented in Chapter 4. The mixing conditions were a mixing speed of 1200 RPM and a time of 30 min. For the material mixture, 15 g PI prepolymer with different GNP weight content was considered, from 1 to 8 wt.%. After the material mixing, it was spin-coated on silicon wafers (3000 RPM for 60 s) and then thermally cured following the standard procedure depicted in Chapter 4.

Micrographs of cured films were taken using a light microscope and they are presented in Fig. 5.1 in a gray scale format. The large pictures correspond to micrographs taken with a magnification of 50x and the small ones with a 2.5x magnification. In Fig. 5.1a, a film with a GNP concentration of 1 wt.% is shown. Although some individual GNPs of approximately 2 µm diameter are visible, the other larger elements of about 10 µm are GNP clusters.

A sample with a GNP load of 2 wt.% can be seen in Fig. 5.1b. The GNP clusters of the same size range remained in this sample. However, a larger amount of smaller elements (5 µm range) were observed, probably large individual GNPs or few-particle agglomerates.

For a sample with 4 wt.% (Fig. 5.1c), elements with a size of about 5 µm are more noticeable, and the area between the large agglomerates is filled with the small elements. Finally, when the film was produced at the higher amount of 8 wt.% (Fig. 5.1d), more clusters in the range of 10 - 15 µm were observed, making it difficult to see the individual particles.

This suggests that for GNP concentrations >4 wt.%, the mixing method has a limit in its effectiveness to break down the GNP agglomerates. Nevertheless, it should be mentioned that the cluster size is comparable to the one observed with CNT/PI films.

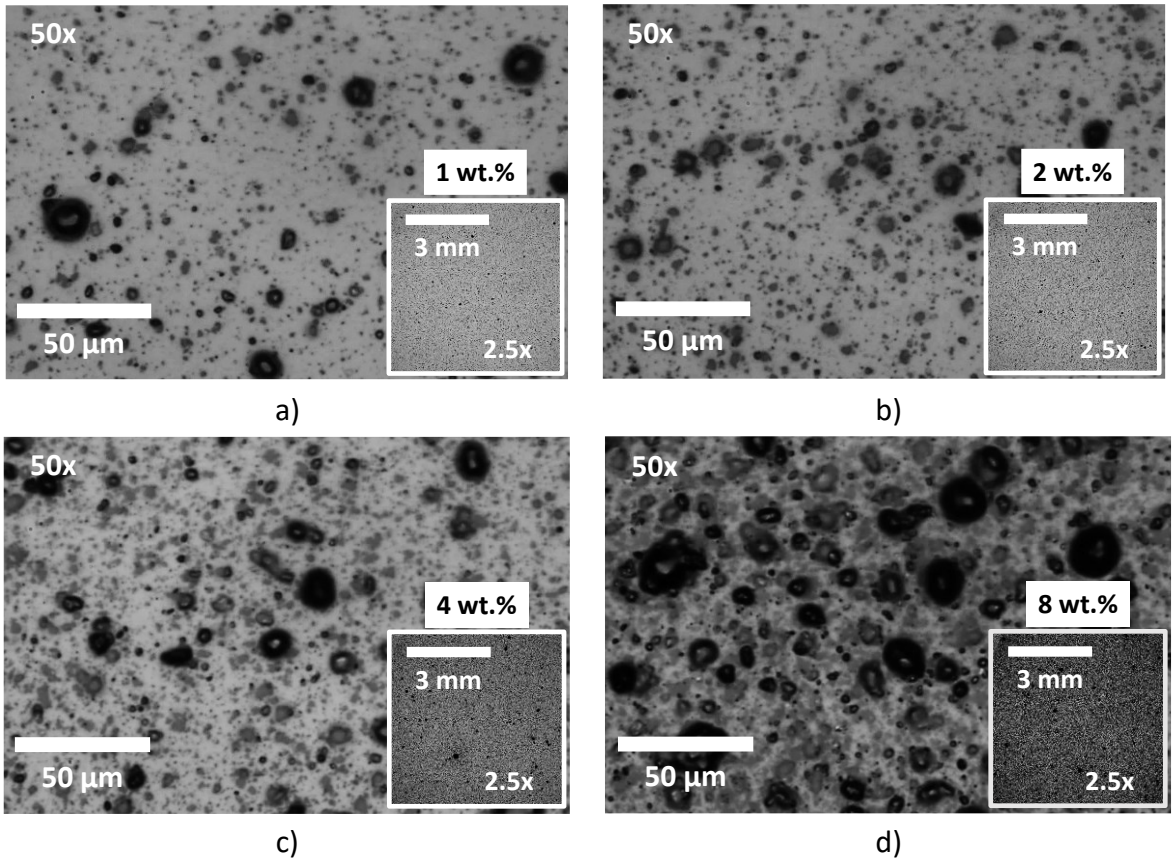

Fig. 5.1 Micrographs of GNP/PI films with different concentrations. a) 1 wt.%. b) 2 wt.%. c) 4 wt.%. d) 8 wt.%.

A measurement of the electrical resistance of the GNP/PI films showed that the electrical resistance of the samples was above the measuring range. Although a higher GNP content should improve the electrical conductivity of the films, it has the drawback of increasing the material viscosity. Therefore, this material was not considered for further fabrication of the films.

5.2 Percolation Modeling of GNP/PI Films

A possible explanation for the low electrical conductivity of the GNP/PI films is a higher electrical percolation threshold for this material combination, since the particle size and its aspect ratio influence the percolation threshold of polymer nanocomposites [66,82,83].

The GNP/PI percolation threshold was estimated by a 2D Montecarlo model, with the GNP/PI composite considered as a square area. This model followed the approach described in Chapter 3, but adapted to the GNP geometry as represented in Fig. 5.2.

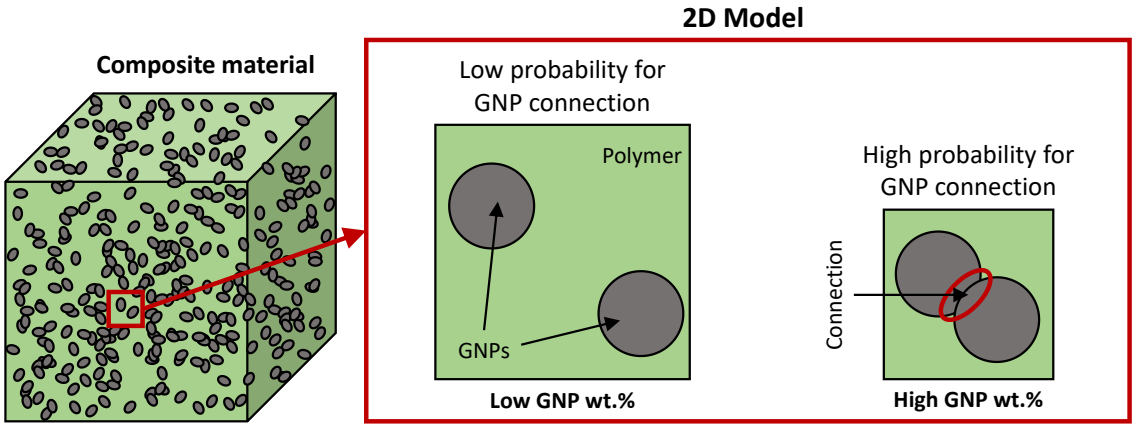

Fig. 5.2 Schema for the GNP percolation model based on Montecarlo.

For the model, the number of particles was set to n = 100, and its area was adjusted to different GNP concentrations. The GNPs were generated as discs in random locations inside the model area, and the percentage of GNPs with at least one connection to another particle was saved. The process was repeated for 1000 times to compute the connection probability.

The geometry considered for the GNP was a circle with a radius of 2 µm and a thickness of 10 nm. To compensate for particle intersection, the model was considered with a thickness equal to 2 times the GNP thickness. The material densities for the computation of the model area were P_{PI} = 1100 kg/m^3 [21] and P_{GNP} = 2100 kg/m^3 [81] for PI and GNP, respectively. The model predictions are plotted in Fig. 5.3 with some examples of the generated 2D model.

The model indicated that for a GNP content below 1 wt.%, the electrical properties of the GNP/PI film are expected to be close to an insulation material, as the connection probability is close to zero. However, for a concentration of 20 wt.% or more, the connection probability of GNPs is above 50 %, which should result in an electrically conductive material as this region corresponds to the transition insulator-to-conductor. Finally, the GNPs should be fully connected at concentrations of 80 wt.%, reaching a saturation.

When comparing with the previous predictions of CNT/PI model, it was observed that the percolation curve of the GNPs is shifted to the right by a factor about 20 times the CNT concentration (wt.%).

Moreover, as reported in the following chapters, for practical use of the CNT/PI films, concentrations of 1.5 wt.% or above should be considered, corresponding to a particle connection probability of 70 %. By assuming a similar requirement for the GNP/PI films, concentrations above 30 wt.% would be used. However, such GNP amounts are not practical due to the viscosity of the mixtures.

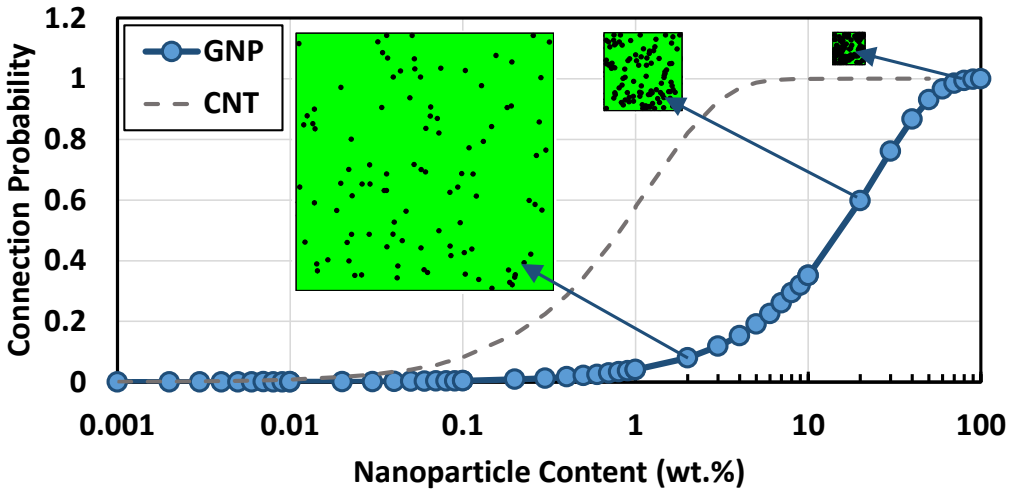

Fig. 5.3 Percolation predictions of GNP/PI composites by Montecarlo modeling.

Besides the different percolation predictions, the micrographs of films with 1 wt.% (see Fig. 5.4) also showed differences. The GNP films (see Fig. 5.4a) appear to be rather isolated elements, which agrees with the simulations. In contrast, the CNTs (see Fig. 5.4b) are interconnected, forming a particle network. For this reason, the CNTs were chosen above the GNPs for the fabrication of the PI films.

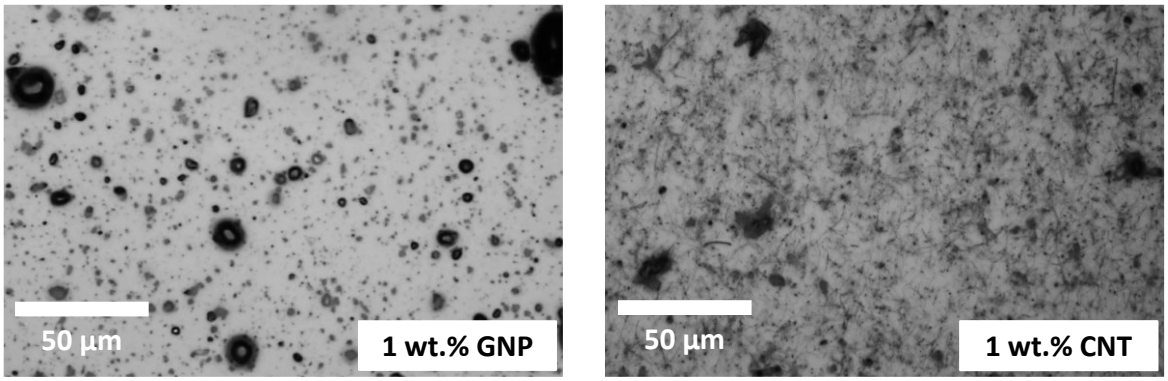

a) b)

Fig. 5.4 Comparison of films with different particles. a) GNPs. b) CNTs.

Chapter 6: Characterization of CNT/PI Films

This chapter discusses the characterization of the CNT/PI composite films as a bulk material. The first measurement was the electrical resistance of the samples for its comparison with model predictions. Selected CNT concentrations were further evaluated for their piezoresistive and thermoresistive properties. The effect of the film thickness and changes in the mechanical resistance were also studied.

The piezoresistive response of the CNT/PI films was partially presented in an international conference: M. Cen-Puc, T. De Rijk, M.V. Gleason, W. Lang, Carbon Nanotubes/Polymer Films for Microsensors Applications, in: 2021 IEEE Sensors, IEEE, Sydney, Australia, 2021: pp. 1–4.

6.1 Electrical Conductivity of CNT/PI Films

A set of films with a thickness of 5 µm was produced using the mechanical mixing method previously described (Chapter 4). The CNT content of samples ranged from 0.1 up to 10 wt.%. The films were produced on silicon wafers without adhesion promoter and manually cut using a 3D printed tool (see Appendix C). Rectangular samples (3 by 1 cm) obtained by this method are shown in Fig. 6.1. Fabrication of samples above 10 wt.% was avoided due to the high viscosity of the mixture.

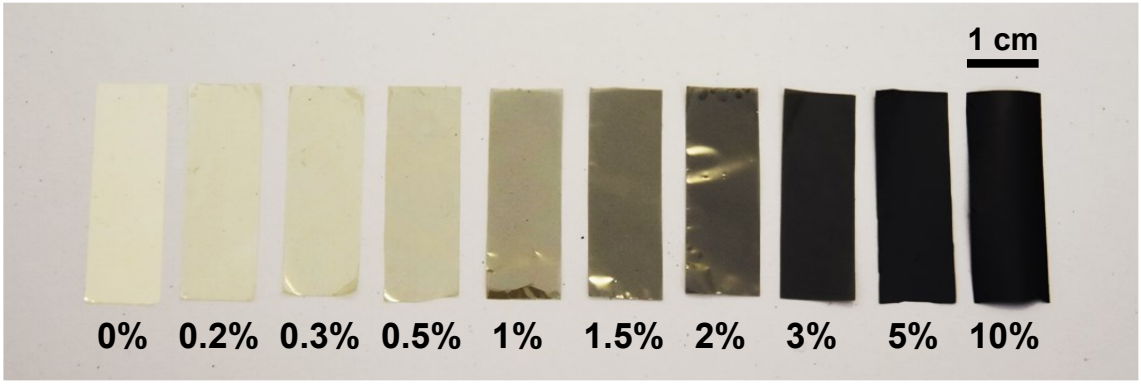

Fig. 6.1 Example of films produced by mechanical mixing.

The measurements were performed with a digital multimeter Keithley 6500 with a measuring range of 120 MΩ. Due to the limitation of the measuring device, the samples with a high electrical resistance (1 wt.% CNT content and below) were cut as squares of 1 by 1 cm, and their electrical resistance was measured through their thickness (5 µm), as schematized in Fig.

6.2. Two copper wires were attached with silver glue (Elecolite 327) at the top and bottom of the sample for the connections with the multimeter.

For samples with a low electrical resistance, rectangles of 1 by 3 cm were cut from the films. Two copper wires were attached at the ends of the rectangles with the silver glue, leaving a distance of 1 cm between the glued areas as represented in Fig. 6.2.

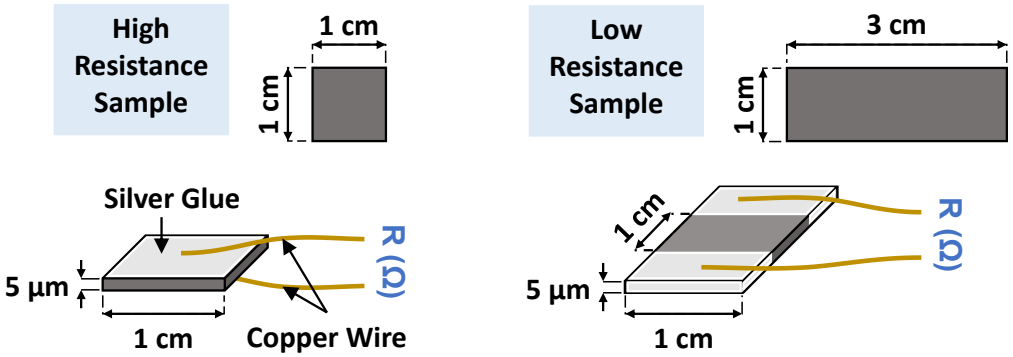

Fig. 6.2 Schema of sample preparation for percolation characterization.

The electrical resistance of samples was used to compute their electrical conductivity κ_{dc} considering the sample geometry as $\kappa_{dc} = L/(RA)$, R being the electrical resistance, A the cross-sectional area, and L the distance between silver areas. Their electrical conductivity showed a dependence on the CNT concentration (Fig. 6.3), following the percolation law [84]:

$$\kappa_{dc} = \kappa_0(f_{wt} - f_c)^{\mu} \qquad \text{Eq. 6.1}$$

where κ_{dc} is the electrical conductivity of the composite, κ_0 is a proportionality constant, f_{wt} is the filler concentration, and f_c is the critical filler concentration or percolation threshold. The exponent μ is attributed to the dimensionality of the material system, with values close to 1 related to a 2D system and values close to 2 related to a 3D composite.

Eq. 6.1 was fitted (see Fig. 6.3) to the experimental data considering a CNT percolation threshold f_c = 0.1 wt.% [85] and an electrical conductivity of $\kappa_{dc} = 1x10^6$ S/m for the ideal case of a 100 wt.% CNT sample. The fitted exponent of the percolation equation was around μ = 1.7, which agrees with the reported values range [29]. The rule of mixtures (Eq. 3.9) was also included in Fig. 6.3, considering a CNT conductivity of $\kappa_{CNT} = 1x10^6$ S/m and $\kappa_{PI} = 1x10^{-14}$ S/m for the PI.

Both expressions follow the general electrical behavior of the CNT/PI film composites, with the percolation equation showing a better correspondence to the experimental data. However, both curves did not predict well the electrical conductivity for CNT concentrations lower than 3 wt.%, since they overestimate the electrical conductivities of the samples.

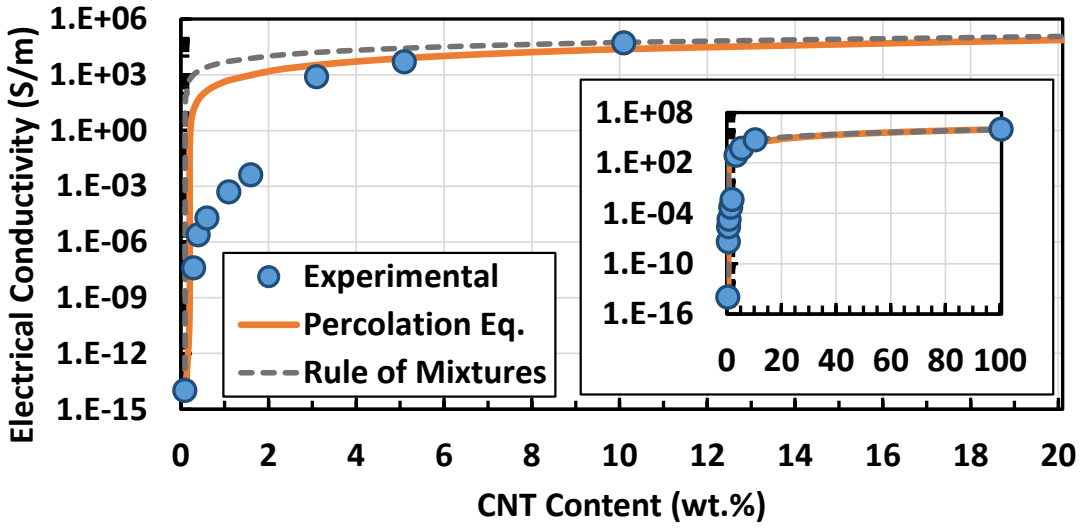

Fig. 6.3 Electrical conductivity of the CNT/PI films and fitting to percolation equation.

Although a better fitting of the percolation equation can be accomplished by taking a narrower range of the CNT concentrations, this results in an overestimation of the conductivity for higher CNT concentrations. Therefore, it can be concluded that the expressions for the electrical conductivity are more useful for the predictions of a composite film with particle concentrations significantly above the electrical percolation threshold.

The predictions of the Montecarlo-based model were also compared to the experimental data. Although a quantitative comparison between the datasets is not feasible, a qualitative comparison of their behavior as a function of the CNT concentration is presented in Fig. 6.4.

The scale of the electrical conductivity was adjusted to show how it follows the behavior of the Montecarlo model. For CNT concentrations below 0.1 wt.%, the CNT-to-CNT connection probability was close to zero, and for concentrations above that, the probability increased nonlinearly, reaching a saturation close to 10 wt.%. Similarly, the electrical conductivity of the films with a concentration above 0.1 wt.% was higher than the pristine PI and increased nonlinearly. Although a saturation of the electrical conductivity is not expected for a

composite concentration of 10 wt.%, this comparison showed that the Montecarlo-based model can predict the insulator-to-conductor transition region of the CNT/PI composite films.

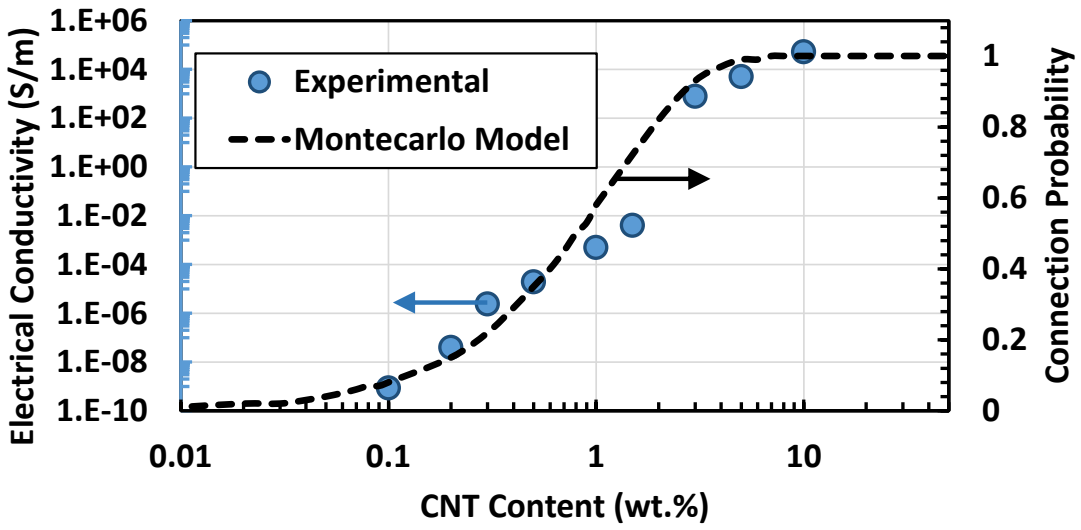

Fig. 6.4 Montecarlo predictions and the experimental data of electrical conductivity.

The measurements indicated that electrical conductive films with CNT concentrations below 1 wt.% are feasible due to the low electrical percolation. However, their electrical resistances were high (MΩ), and therefore, it was decided to continue the further characterizations with higher CNT contents (> 1 wt.%).

6.2 Piezoresistive Properties of CNT/PI Films

The piezoresistive characterization of the material was performed with rectangular samples cut from films with 1.5 wt.%, 2 wt.% and 3 wt.% CNT content. The sample dimensions were 6 cm in length and 1 cm wide, manually cut from films (Appendix C). For testing the influence of sample thickness, the CNT/PI mixtures were spin-coated on silicon wafers at speeds of 1000 RPM, 1500 RPM and 3000 RPM, which yielded film thicknesses of 10, 8 and 5 µm, respectively.

In the case of the films produced with 1.5 wt.% and 2 wt.% CNT concentrations, their thinnest samples (5 µm) were outside the measuring range of the multimeter (Keithley 6500) and therefore discarded. On the other hand, all the proposed thicknesses for the 3 wt.% CNT films were measurable with the multimeter and hence used for characterizations.

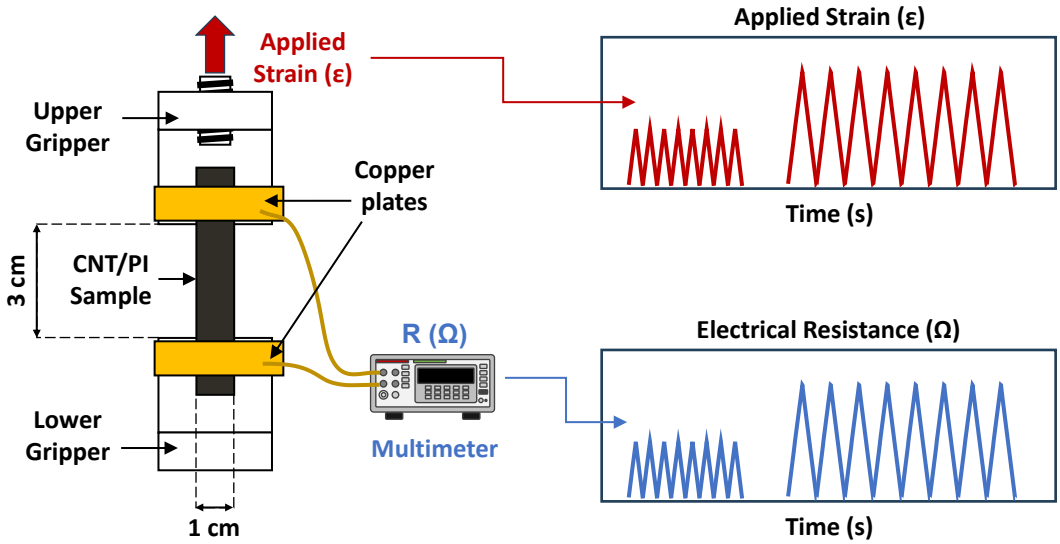

Fig. 6.5 Experimental setup for piezoresistive characterization of CNT/PI films.

The piezoresistive characterization was performed with the Condor 100 XYZTEC bond tester with a load cell of 100 N. The proposed strain levels were 0.5, 1, 1.5, 2, 2.5 and 3 %, and they were sequentially applied for 10 pull-release cycles per stain level. For fixation of the samples to the bond tester, a pair of custom grippers were designed and fabricated with a 3D printer (Appendix C). The initial separation between the grippers was 3 cm, and the rate for strain and release was 30 µm/s. The schema characterization setup is presented in Fig. 6.5.

The electrical connection between the multimeter and the film samples was achieved using two rectangular copper plates with 1 cm width and 4 cm length, placed at the upper and lower grippers. The electrical resistance of the samples was recorded using the data acquisition software of the multimeter.

The values of electrical resistance (R) of the samples were normalized according to their initial value (R_0) as $\Delta R/R_0$, being $\Delta R = R - R_0$ the electrical resistance change. The normalized data of samples are presented in Fig. 6.6. The missing data in Fig. 6.6a for deformations $\varepsilon > 2$ % is because the measurements were outside the range of the instrument.

The normalized results are organized with the CNT concentration increasing from top to bottom, i.e., the 1.5 wt.% samples in the upper row, the 2 wt.% samples in the middle row, and the lower row presents the results of films with 3 wt.%. The thickness is arranged to show the 10 µm thick layers on the left column and the 8 µm thick layers on the right one.

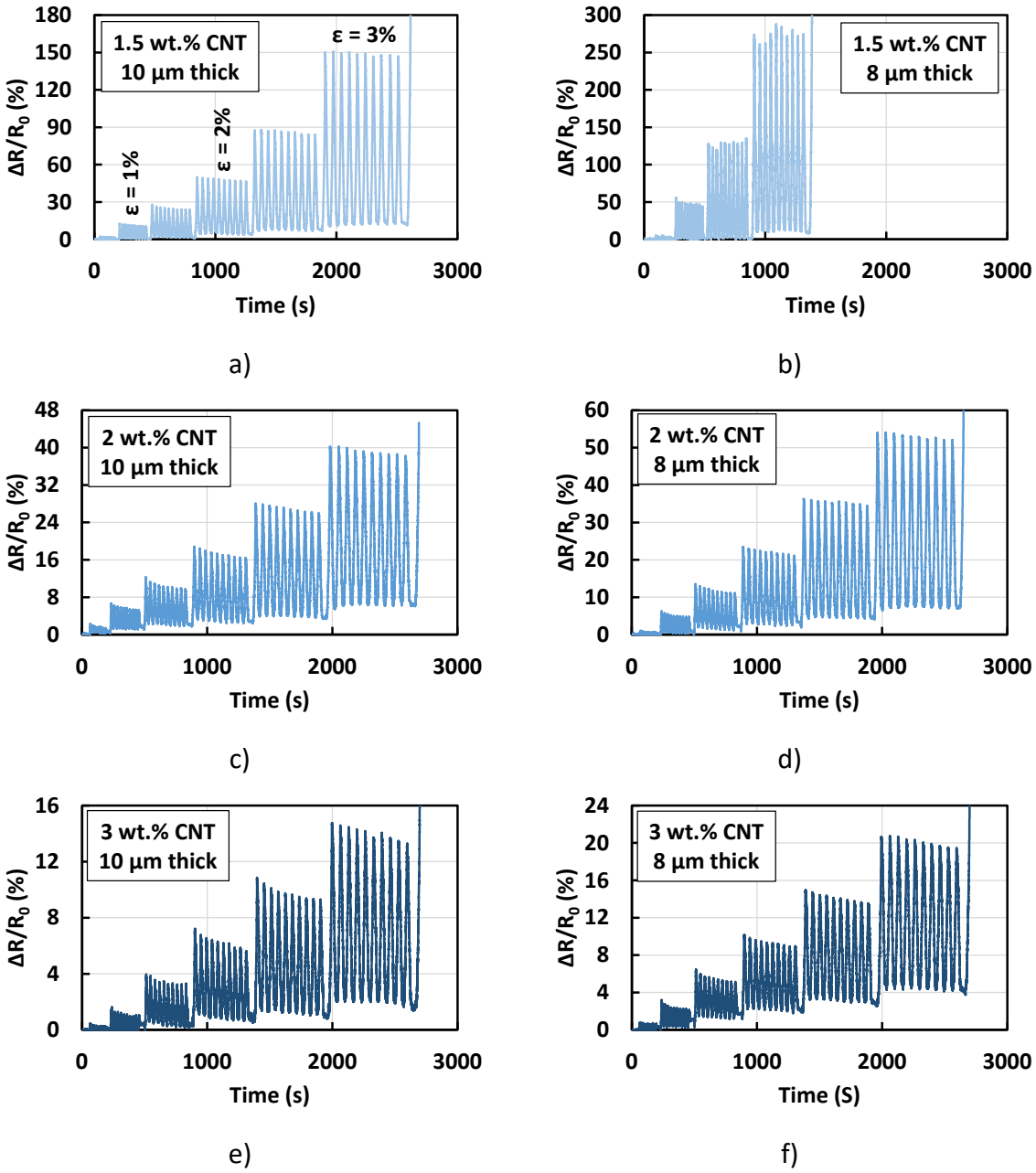

Fig. 6.6 Normalized values of piezoresistive characterization of CNT/PI films. a) 1.5 wt.% with 10 µm. b) 1.5 wt.% with 10 µm. c) 2 wt.% with 10 µm. d) 2 wt.% with 8 µm. e) 3 wt.% with 10 µm. f) 3 wt.% with 8 µm.

All the samples exhibited an increment of their electrical resistance as a function of the applied strain, but the samples with lower amounts of CNTs showed a higher sensitivity. For example, in the case of the 10 µm thick layers, a strain of ε = 2 % leads to an electrical resistance change of around 48 % in samples with 1.5 wt.% (Fig. 6.6a). Nevertheless, the same strain produced a change of 17 % in the 2 wt.% sample (Fig. 6.6c) and only 6 % for the highest CNT concentration of 3 wt.% (Fig. 6.6e).

The material thickness also influenced the piezoresistive response of samples, making the thinner films more sensitive to deformation. For example, in the case of films with 1.5 wt.% CNT, a 10 µm thick film (Fig. 6.6a) with an applied strain of ε = 2 % showed a change of 48 %, while for a sample with a thickness of 8 µm (Fig. 6.6b), the same deformation produced an impressive change of 280 %.

For higher CNT concentration samples, the effect of film thickness was still present but reduced. For example, under a deformation ε = 2 %, a film with 2 wt.% CNT and 10 µm thickness exhibited a resistance change of 17 % (Fig. 6.6c), while for a sample with 8 µm thickness, the change was 22 % (Fig. 6.6d). Finally, for a sample with 3 wt.% and a thickness of 10 µm, its electrical resistance changed by around 6 % under a deformation ε = 2 % (Fig. 6.6d), while the change of a layer with 8 µm thickness was only 9 % (Fig. 6.6f).

By considering the average peak values of the normalized electrical resistances, the gauge factor K of the samples was extracted as described by Eq. 1.2. The K factors were grouped by layer thickness, with values of 10 µm thick samples in Fig. 6.7a and data of 8 µm thick samples in Fig. 6.7b. To facilitate comparison between curves, the graphs used a logarithm scale.

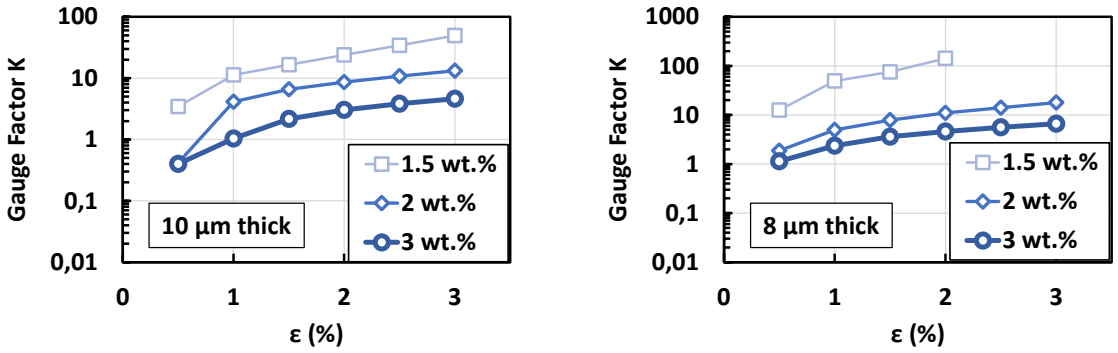

a) b)

Fig. 6.7 Extracted gauge factor K of CNT/PI films as a bulk material. a) Samples with 10 µm thickness. b) Samples with 8 µm thickness.

From the gauge factor plots, it can be seen that there is a trend to higher gauge factors K for samples with lower CNT concentrations. For example, the 10 µm thickest samples (Fig. 6.7a) under a deformation ε = 1 % exhibited a gauge factor of K = 11.3, K = 4.1 and K = 1 for CNT concentrations of 1.5, 2 and 3 wt.%, respectively. However, the average gauge factors are

higher for the 8 µm thick layer under a deformation ε = 1 %, being those K = 49.5, K = 5 and K = 2.4 for CNT concentrations of 1.5, 2 and 3 wt.%, respectively.

Further characterizations were carried out with the 5 µm thick films at 3 wt.% CNT. After the extraction of the gauge factor (Fig. 6.8a), the same trend of higher sensitivity with thinner layers was observed. For this CNT concentration, the gauge factor for a strain ε = 1 % was K = 1 for a 10 µm thick sample, then increased to K = 2.4 for the 8 µm thick film and reached a maximum value of K = 7.6 for the sample with 5 µm thickness.

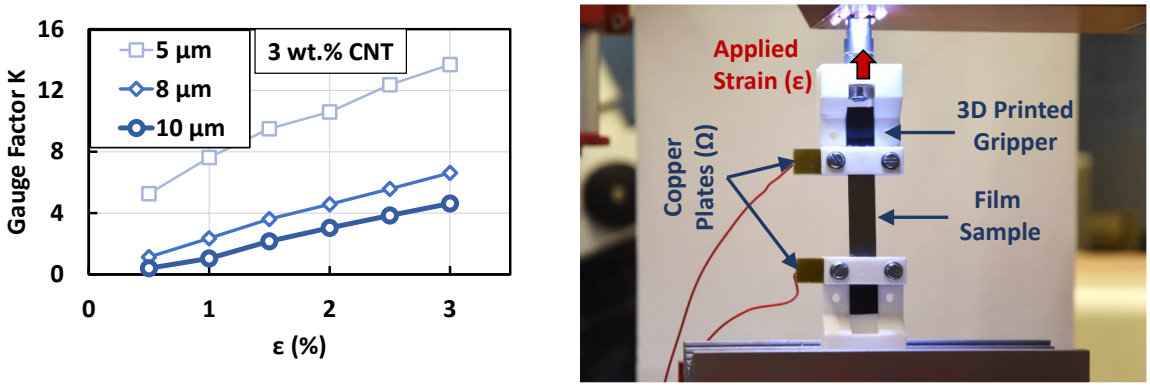

a) b)

Fig. 6.8 Piezoresistive response of 3 wt.% films. a) Influence of thickness on the film sensitivity. b) Actual sample during the characterization.

Although the results in Fig. 6.7 indicated that the samples with 1.5 wt.% are the most sensitive layers to the applied strain, they are not suitable for the aimed application. The first criterion for selecting a piezoresistive layer is a minimum thickness of 5 µm, which rules out both 1.5 wt.% and 2 w.t% samples. This layer thickness is preferred because it matches the thickness of pristine PI films and likely also the known microfabrication parameters. The second limitation is the electrical resistance of the films since thinner layers have electrical resistances above the capabilities of the multimeter and can not be measured.

6.3 Cyclic Piezoresistive Response of Films

During the piezoresistive characterization of the films, the drift of their initial electrical resistance was observed after each strain cycle. This behavior has been reported in other polymers loaded with CNTs [86–89] and short carbon fibers. This change can be attributed to the straightening or rearrangement of the fillers [90], which leads to irreversible changes of

the particle connections. To better understand this behavior, longer cyclic strain experiments were proposed.

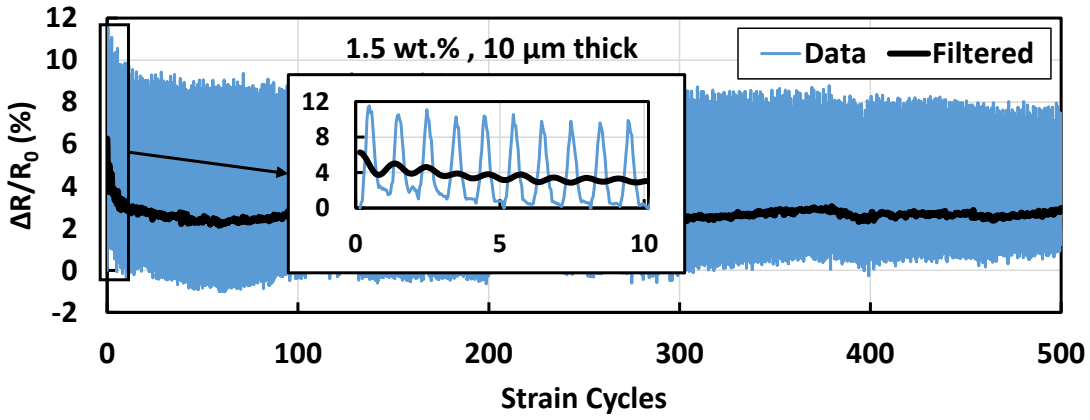

a)

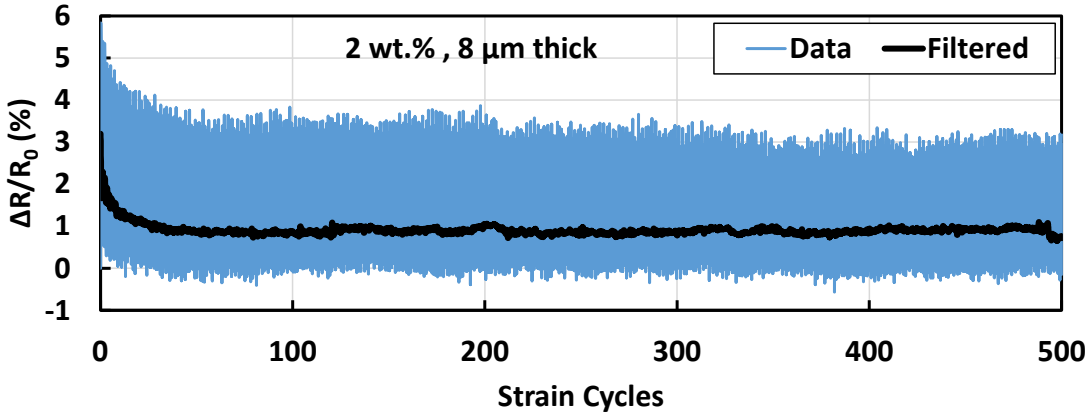

b)

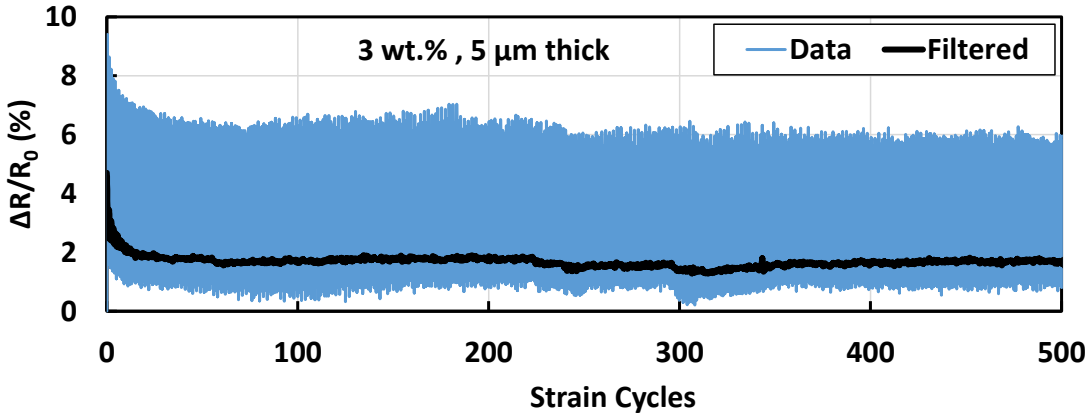

c)

Fig. 6.9 Results of the long cyclic piezoresistive test. a) 1.5 wt.% CNT and 10 µm thick sample. b) 2 wt.% CNT and 8 µm thick sample. c) 3 wt.% CNT and 5 µm thick sample.

To study the drifting of the electrical resistance of the CNT/PI films, a custom routine was programmed for the bond tester (Condor 100 XYZTEC). This program applied a strain of ε = 1 % for 500 cycles to the films. The geometry of the samples and the testing parameters were the same as the previous characterization.

For better visualization of the data plots, the electrical measurements were normalized using their initial electrical resistance, and a low-pass filter was applied to show the plot trend. Examples of the curves of different films are presented in Fig. 6.9.

Independently of the CNT content or material thickness, the base resistance of all the samples increased after the first cycle up to 2 % of the normalized data (see inset in Fig. 6.9a). This change was gradually reduced in the following cycles, reaching a fairly constant value around the 25th cycle. After this on-set period, the remaining drift was corrected by adding a linear function to the data.

After the first 25 cycles, the measurements did not reach their initial normalized value ($\Delta R/R_0 = 0$ %). The measurements of some samples oscillated during the whole experiment, like the 1.5 wt.% CNT sample in Fig. 6.9a, where the data was negative during the first 100 cycles but remained positive after 300 cycles. On the other hand, some samples reached stable values, like the film with 2 wt.% CNT in the Fig. 6.9b with an value of $\Delta R/R_0 = -0.1$ % and the sample with 3 wt.% CNT in Fig. 6.9c with a normalized electrical data that remained around $\Delta R/R_0 = 1$ %.

Another characteristic observed was the amplitude reduction of the electrical signal after the first 100 cycles, which was suspected to be dependent on the mechanical properties of the material and therefore, the mechanical data of the cyclic test was reviewed.

The mechanical data was exported from the Condor 100 XYZTEC bond tester, and a custom script written in MATLAB assisted in extracting the peak force from each strain cycle. The peak forces were then normalized using the data of the first cycle. The values for some samples are presented in Fig. 6.10a. Experiments with pure PI films as a reference were also performed.

The force measurements were fairly constant during the first 20 to 30 cycles, but then they increased, indicating a material stiffening. After approximately 100 cycles, the force applied to the samples was gradually reduced until the end of the experiment.

The increment in force can be attributed to a material strengthening, which in the case of polymers is produced due to the local alignment of their molecular chains under applied stresses [91–93]. The force reduction can be explained in terms of material fatigue, since polymers have viscoelastic characteristics, their heating during energy dissipation can produce material softening and failure [94,95]. Such material changes are not easy to see in a typical stress-train plot of the samples (Fig. 6.10b).

Interestingly, the stable force region (<30 cycles) agrees with the cycles where the most pronounced electrical changes occur, so the electrical changes are likely due to the re-arrangement of the particles inside the polymer. After that, the force reduction after 100 cycles also matches the region at which the electrical measurements had an amplitude reduction, which is likely related to a change in the mechanical properties of the polymer.

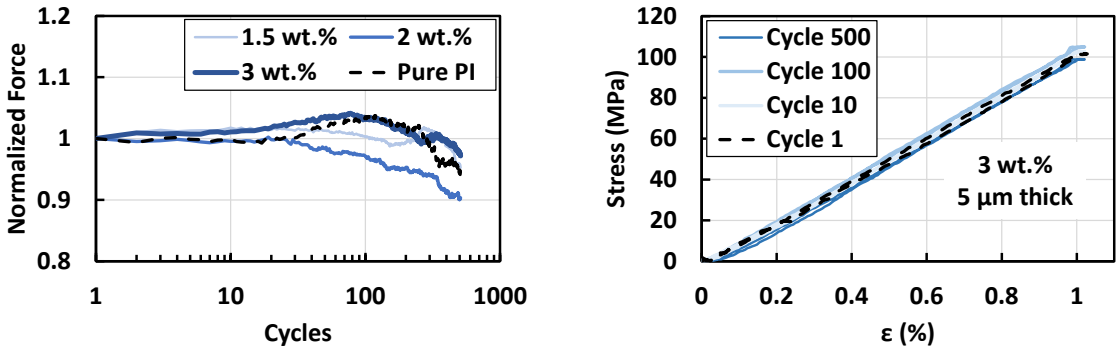

a) b)

Fig. 6.10 Mechanical behavior of films under cyclic ε = 1 % strain. a) Normalized peak forces. b) Stress-strain plots for cyclic loadings.

Given these results, it can be concluded that the sensors based on these materials would probably require a recalibration during their use or even a pre-aging step.

6.4 Influence of CNTs on Mechanical Properties of Films

For a typical composite material, the expected properties (density, elastic modulus, thermal expansion, etc.) are a combination of its constituents. Since the piezoresistive films are produced from a combination of PI and CNT, their mechanical properties are expected to be different from the neat PI.

The influence of the CNT content on the mechanical properties of the film was determined by performing destructive mechanical tensile tests. The experiments are based on the ASTM

norm D882 [96], but adapted to smaller samples. The tests were performed with films loaded with 0.5, 1, 2 and 3 wt.% CNT, samples of pure PI were also evaluated.

Unlike the previous manually cut samples, the new samples were produced by RIE etching to reduce the influence of edge defects that might downgrade the mechanical resistance of the samples. After the thermal curing of the films, a photoresist AZ92960 layer of 10 µm was spin-coated, UV-exposed and developed. The films were etched with O_2/CF_4 gas with the Multiplex ICP Reactive Ion Etcher, leading to rectangular samples of 75 mm in length and a width of 5 mm. The samples were manually peeled from the silicon wafers using small tweezers.

The samples were evaluated with the Condor 100 XYZTEC bond tester with a 100 N cell, an initial grippers separation of L_0 = 40 mm and a strain rate set to 60 µm/s. The force data was used to compute the material stress as $\sigma = F/A$, with F as the applied force and A as the cross-sectional area of the sample. The cross-sectional area A was obtained for an average film thickness of 5 µm and a width of 5 mm. The gripper displacement (ΔL) was used to calculate the applied strain as $\varepsilon = \Delta L/L_0$.

At least three samples per CNT concentration were evaluated to obtain the average mechanical resistance (Fig. 6.11a) and strain (Fig. 6.11b). The general trend indicated that the use of CNTs influences on the mechanical resistance and the maximum strain of the films. The CNTs reinforced the PI, as a higher mechanical resistance was observed with higher CNT contents.

The reference PI film (0 wt.% CNT) had an average σ = 170 MPa, which is lower than the data of the manufacturer (σ = 256 MPa) [21] but still in the expected range, and it was consistent for all the evaluated samples. For samples with 0.5 wt.% CNTs, the mechanical resistance increased to σ = 180 MPa, which is about 6 %. For a 1 wt.% CNT content, the film increased more its mechanical resistance, achieving σ = 212 MPa, which represents 24 % in comparison with the pure PI. This mechanical resistance improvement continued with the 2 and 3 wt.% CNT samples, achieving the mechanical values of σ = 247 MPa and σ = 263 MPa, respectively.

Regarding the maximum strain of the films, the pure PI sample had a strain of ε = 3.23 %, which is lower than the data of the material manufacturer (ε = 35 %). However, it can be seen that the samples loaded with CNTs have higher strains in comparison to the pristine PI. The samples with 0.5 wt.% CNT content had a maximum strain ε = 3.82 %, and the films with

1 wt.% CNT had a slightly higher strain ε = 3.87 %. In the case of the films with 2 and 3 wt.%, the maximum strains were ε = 4.64 % and ε = 4.68 %, respectively.

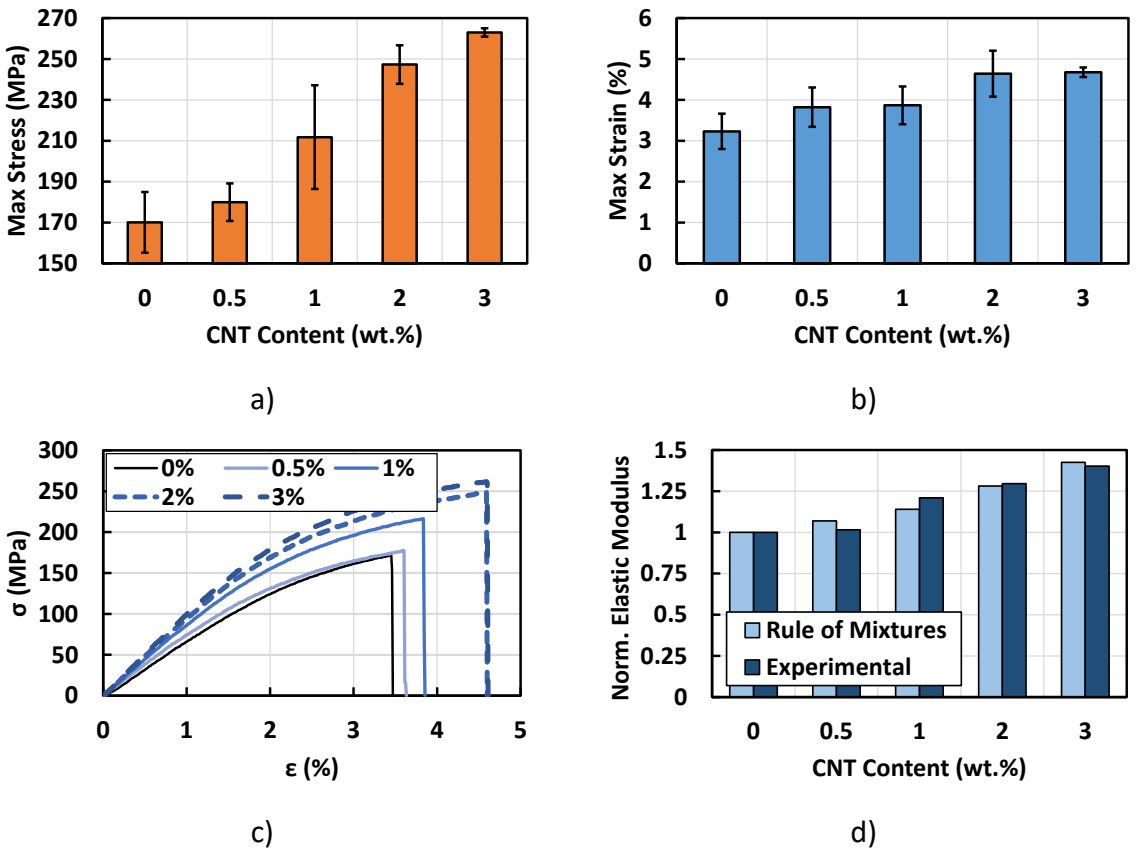

Fig. 6.11 Mechanical properties of the CNT/PI films. a) Mechanical resistance. b) Maximum strain. c) Representative stress-strain curves. d) Normalized elastic modulus and predictions of the rule of mixture.

Looking at the example curves of mechanical behavior in Fig. 6.11, it is noticed that samples failed at different strain levels, therefore reaching different stress values. A fairer comparison between the samples was proposed using their elastic modulus. This was achieved by obtaining the ratio between material stress and the strain by E = σ/ε.

The stress (σ) values measured at a deformation ε = 1 % were used to compute the elastic modulus of the pristine PI samples, which resulted in an average modulus E = 7.2 GPa. This value was lower than the data of the supplier E = 9.8 GPa, but still comparable, and it was used to normalize the elastic modulus of the CNT loaded samples as presented in Fig. 6.11d. The normalized data showed that the elastic modulus of films increased up to 40 % with a 3 wt.% CNT content.

Interestingly, the increase in the elastic modulus of the CNT-loaded films seems to follow the behavior described by the rule of mixtures for elastic modulus of composite materials, although it was originally proposed for continuous fiber composites [13,14,91]:

$$E_{com} = E_{CNT}v_{CNT} + E_{PI}(1 - v_{CNT}) \qquad \text{Eq. 6.2}$$

where E_{com} is the expected elastic modulus of the film, E_{CNT} is the elastic modulus of the CNT, E_{PI} is the elastic modulus of the polymer, and v_{CNT} is the CNT content as a volume fraction.

The predictions for the composite using Eq. 6.2 were computed by assuming a CNT elastic modulus E_{CNT} = 0.27 TPa, which is in the reported range for CNTs. For the PI, the elastic modulus was kept as reported by the manufacturer E_{PI} = 9.8 GPa. The normalized predictions are plotted in the Fig. 6.11d. The good agreement between the measured data and the predictions of the rule of mixtures indicates that this simple model can be used to describe the behavior of the films for the used CNT content range.

The use of CNTs influences the mechanical properties of the piezoresistive films, although it does not degrade them. On the contrary, this combination of materials reinforces the polymer since its failure occurs with higher deformations, and its mechanical resistance also increases.

6.5 Thermoresistive Response of CNT/PI Films

The thermoresistivity of a material describes its electrical resistance as a function of its temperature. For example, thermistors based on semiconductors have a nonlinear reduction of their electrical resistance with increasing temperature. On the other hand, metals present a positive linear relationship, increasing their electrical resistance with increasing temperature. Therefore, the temperature dependence of the CNT/PI films was evaluated.

The thermoresistive characterization of the films (1.5, 2 and 3 wt.% CNT) was performed using rectangular samples of 2 cm x 1 cm. The samples were manually cut, and copper wires were attached with a separation of 1 cm using silver glue, as represented in Fig. 6.12.

The samples were heated with an oven (Thermo Scientific Heratherm) from room temperature (22 °C) to 120 °C, with a heating ramp of 5 °C/min. The temperature was set for 1.5 h to simulate the curing process of carbon fiber/epoxy composites [97], and afterward, the oven was turned off to cool down until the initial temperature was reached. A commercial

temperature sensor (thermocouple type K) was placed close to the sample to measure the oven temperature. The heating process was repeated for 4 cycles.

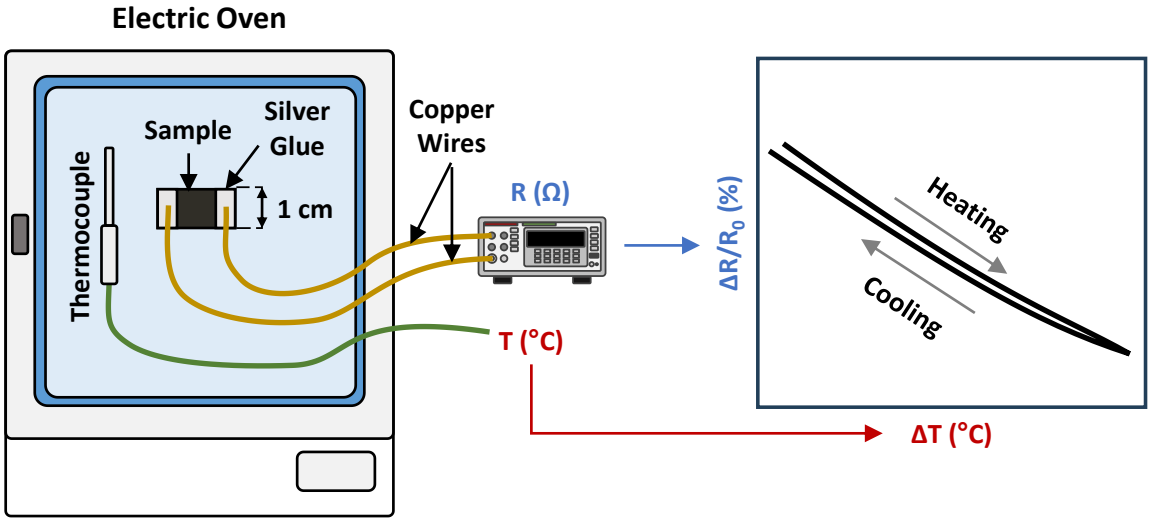

Fig. 6.12 Schema of the thermoresistive characterization of the CNT/PI films.

The electrical resistance of the samples and the temperature sensor were recorded simultaneously with a multimeter Keithley 6500 using its recording software. The electrical resistance of samples was normalized according to their initial value at room temperature as $\Delta R/R_0$ for each heating cycle as presented the Fig. 6.13.

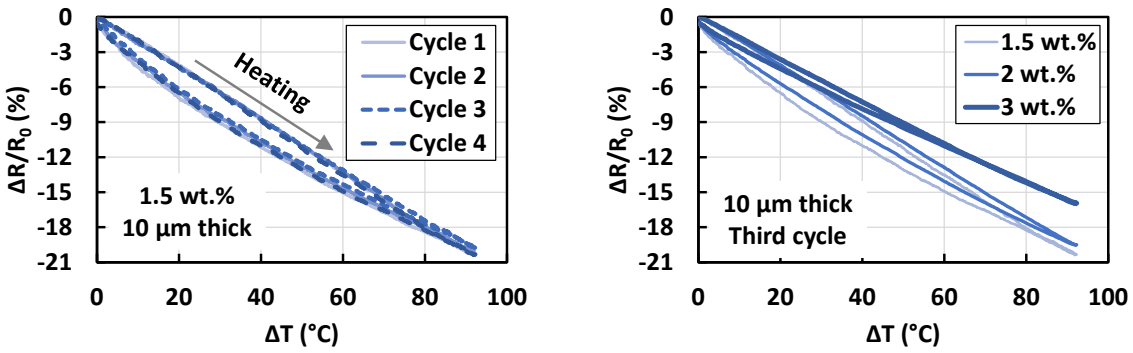

a) b)

Fig. 6.13 Normalized temperature response of CNT/PI films. a) Four continuous heating cycles of a 1.5 wt.% CNT sample. b) Effect of the CNT concentration on temperature response.

As shown in Fig. 6.13, the electrical resistance of samples exhibited a negative relationship with temperature, as their electrical resistance dropped when temperature was increased. This behavior resembles the thermosresistivity of individual CNTs in [58], suggesting that the temperature response of the films would be dominated by the CNTs.

In Fig. 6.13a, four continuous heating cycles of a 10 µm thick sample with a 1.5 wt.% CNT concentration is plotted. As can be seen, the behavior of the sample is reproducible, since the plots of all cycles overlap. Interestingly, the response during the heating has a linear behavior, while during the cooling, the path is nonlinear, thus producing some hysteresis.

Fig. 6.13b illustrates the influence of the CNT concentration on the temperature response of the 10 µm thick films. The normalized data of samples with 1.5, 2 and 3 wt.% during their third characterization cycle are plotted together, showing that 1.5 and 2 wt.% CNT samples are more sensitive to the temperature, having a maximum change of $\Delta R/R_0$ = -21 % and $\Delta R/R_0$ = -20 %, respectively. On the other hand, samples with 3 wt.% CNT showed a maximum change of $\Delta R/R_0$ = -16 %. Additionally, the hysteresis of the curves was reduced as the CNT content was increased.

For comparison of the sensitivity between samples, the maximum normalized resistance ($\Delta R/R_0$) of the films was used to compute a coefficient α. This coefficient indicates the sensitivity of the film to temperature changes (ΔT) and is related to the experimental values as [10]:

$$\Delta R/R_0 = \alpha \Delta T \qquad \text{Eq. 6.3}$$

After computing thermoresistivity coefficient α for films with 8 and 10 µm, the bar plot was generated as presented in the Fig. 6.14.

As indicated in Fig. 6.14a, the samples with concentrations of 1.5 and 2 wt.% CNT have higher coefficients α compared to the 3 wt.% samples. For 10 µm thick samples, the 1.5 wt.% films had an average α = -0.22 %/°C, while the 2 wt.% films had α =-0.21 %/°C, and those with 3 wt.% had α = -0.17 %/°C. By reducing the film thickness to 8 µm, the coefficient of the 1.5 wt.% samples was α =-0.20 %/°C, and for 2 wt.% it was α =-0.21 %/°C. In the case of 3 wt.% films, similar values to the thicker layers were found, α = -0.17 %/°C.

Finally, a thinner layer of 5 µm was investigated for a concentration of 3 wt.%, and their average α values are plotted in Fig. 6.14b. As mentioned before, the samples with 10 µm and 8 µm thickness had similar thermosresistivity coefficients around α = -0.17 %/°C, but the thinner 5 µm thick sample showed a higher coefficient α = -0.20 %/°C.

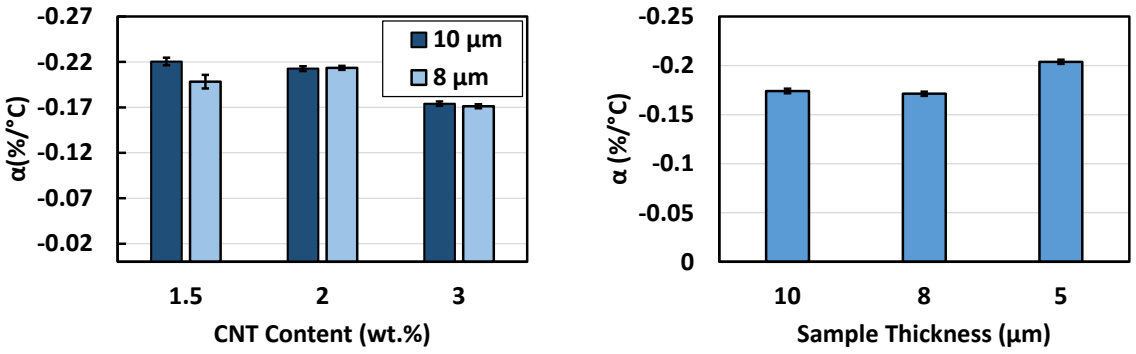

a) b)

Fig. 6.14 Thermoresistivity coefficient α of CNT/PI films. a) Factor α of the 8 µm and 10 µm thick samples. b) Factor α for the samples with 3 wt.% CNT.

After material characterization, piezoresistive films with 3 wt.% CNT content and a thickness of 5 µm were selected due to their low electrical resistance, and their thickness makes them compatible with the microfabrication methods for polyimide. However, the tests also indicated that the material is sensitive to temperature changes. In the following chapters, the use of this material for the fabrication of the strain sensors is explored.

Chapter 7: Fabrication of Strain Sensors

Commercial metal-based strain gauges are produced with meander structures, making their overall electrical resistance larger than a single line of the same length. This geometry has been proposed for strain sensors based on CNTs and their polymer composites [34–39].

This research took the meander geometry for the fabrication of strain gauges based on piezoresistive CNT/PI films. This chapter reports the findings about the manufacturing parameters and the characterization of the first version of the sensors based on the nanocomposite film. The results of this chapter were partially presented at the Conference: M. Cen-Puc, T.D. Rijk, A. Schander, M.V. Gleason, W. Lang, Strain Microsensors Based on Carbon Nanotube/Polyimide Thin Films, in: 2023 IEEE SENSORS, IEEE, Vienna, Austria, 2023: pp. 1–4.

7.1 Effect of CNTs on the Etching of Films

Before the fabrication of the sensors, the etching rate of the nanocomposite films was determined. For the etching rate test, the CNT/PI mixtures with 2 and 3 wt.% were produced using the mechanical mixing approach (Chapter 4). The mixtures were spin-coated on a silicon wafer for 60 s at 3000 RPM and thermally cured. The films were then etched with O_2/CF_4 gas in the ICP Etcher for 5 min. The thickness measurements before and after etching allowed the computation of the etching rate.

Measurements indicated that the etching rate of the nanocomposite layers is slightly slower than that of the pure PI film (0.5 µm/min). The etching rate decreased to 0.49 µm/min for the 2 wt.% CNT films and 0.48 µm/min for the 3 wt.% CNT samples. Therefore, for a 5 µm thick layer with 3 wt.% CNT, a running time of 10.5 min is expected to achieve the complete etching of the material layer.

This slowdown of the etching rate was attributed to the presence of the CNTs within the PI, as they act as a mask during the process since their etching rate is slower compared to polymers [98,99]. This masking effect was later observed in SEM micrographs of films with CNT contents of 0.5, 1, 2 and 3 wt.% that were etched for 2 min (Fig. 7.1).

The sample with 0.5 wt.% CNT (Fig. 7.1a, 8000x magnification) showed some exposed CNTs after etching. Interestingly, besides the CNTs, other thinner lines were observed on the

material surface, as shown in the micrograph. Those traces correspond to CNT locations before the etching that masked the polymer beneath them, leaving such patterns once the CNTs were removed.

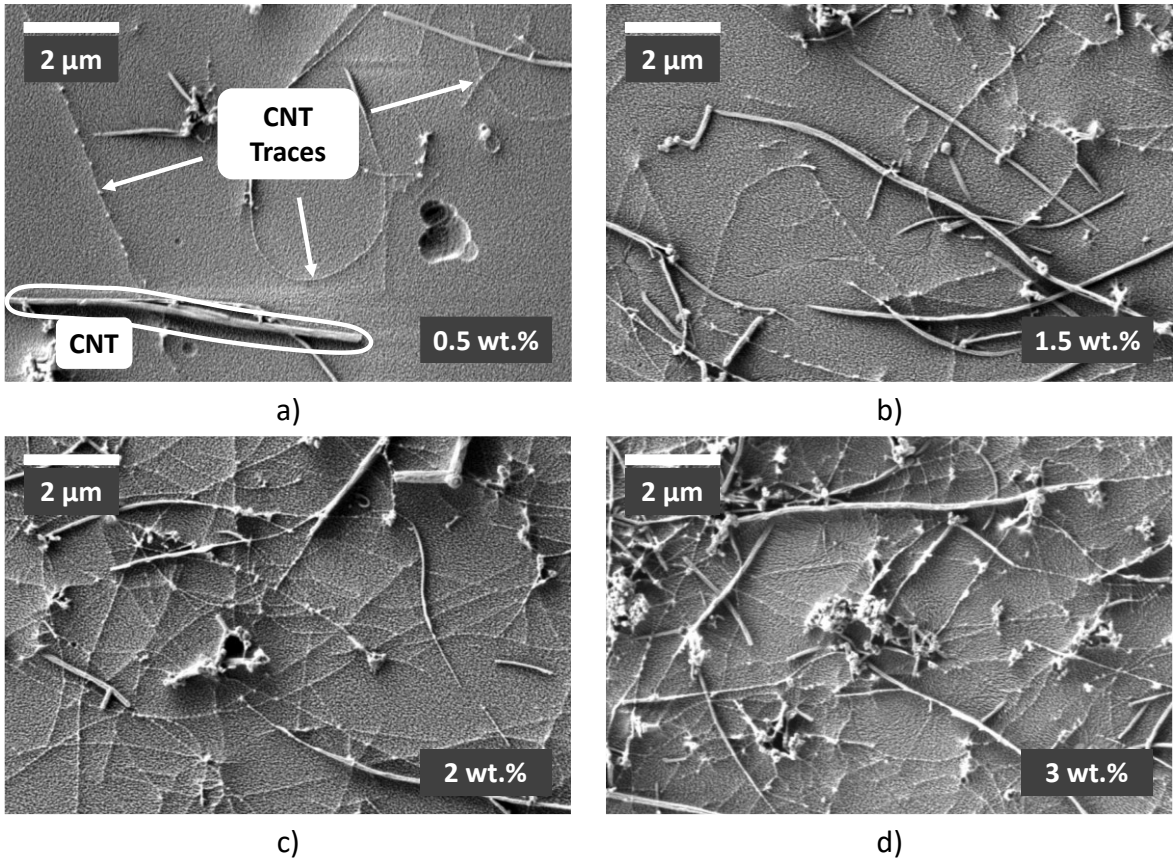

Fig. 7.1 SEM micrographs of CNT/PI films after partial etching by RIE. a) 0.5 wt.%. b) 1.5 wt.%. c) 2 wt.%. d) 3 wt.%.

Fig. 7.1b presents a sample with 1.5 wt.% CNTs, and as expected, more CNTs and CNT traces were observed after the etching. This continued to be observed in other samples with 2 wt.% film (Fig. 7.1c) and 3 wt.% (Fig. 7.1d). The CNT network inside the polymer was denser at higher CNT concentrations, which made the masking phenomenon more noticeable. This explains the similar etching rates between pure PI and the samples below 1.5 wt.% CNT, and the slower etching rate observed for the higher CNT concentration films.

7.2 Meander Structuring of the CNT/PI Layers

The CNT/PI layers were evaluated to produce meander structures, taking as reference the CNT-based sensors found in the literature. The available parameters of the reported sensors

are resumed in Table 7.1. The table includes the number of lines, linewidth, aspect ratio, fabrication method, gauge factor K and electrical resistance range.

Table 7.1 Geometry parameters of reported CNT-based strain gauges.

Matrix or substrate	**Fabrication method**	**Lines**	**Width (µm)**	**Line ratio L/W**	**R range**	**K**	**Ref.**
Parylene-C	RIE & Transfer	4 - 10	10 - 50	20 - 100	MΩ	4 - 6	[33]
Polyimide	Spray-coating & Plasma etching	4 - 8	50 - 200	15 - 60	kΩ	60	[34]
Polyimide	Spray-coating & CNC Milling	4 - 6	200 - 500	6.4 - 16	N/A	0.6 - 0.75	[35]
Polyimide	Inkjet printing & Thermal curing	4	200	40	kΩ - MΩ	1.4	[36]
Quartz fabric	Inkjet printing	N/A	>200	N/A	kΩ	N/A	[37]
Silicone	Magnetic casting	5	N/A	N/A	kΩ	6.5 - 103	[38]
Epoxy	Vacuum resin transfer molding	10	250	40	MΩ	2.5	[39]

The collected information showed that sensor meanders ranged from 4 to 10 lines, the linewidth was between 10 and 500 µm, and the line aspect ratios (length/width) were between 6.4 and 100. Moreover, their sensitivities varied widely, showing gauge factors from K = 0.6 up to K = 105. The base resistance of the sensors was higher than that of commercial ones, covering the range from kΩ to MΩ.

The RIE method was used in this work to fabricate meander structures from the CNT/PI films, using a photomask for photoresist structuring. The objective was to produce the smallest meander structure with an electrical resistance below 120 MΩ, the measuring limit of the multimeter (Keithley 6500). The meanders had five resistive lines with a line aspect ratio L/W = 10, as represented in Fig. 7.2. Seven meander sizes were proposed as a function of the linewidth: 10, 20, 50, 100, 200, 500 and 1000 µm. Contact pads (2 x 2 mm) were produced at the ends of the meanders for measurements.

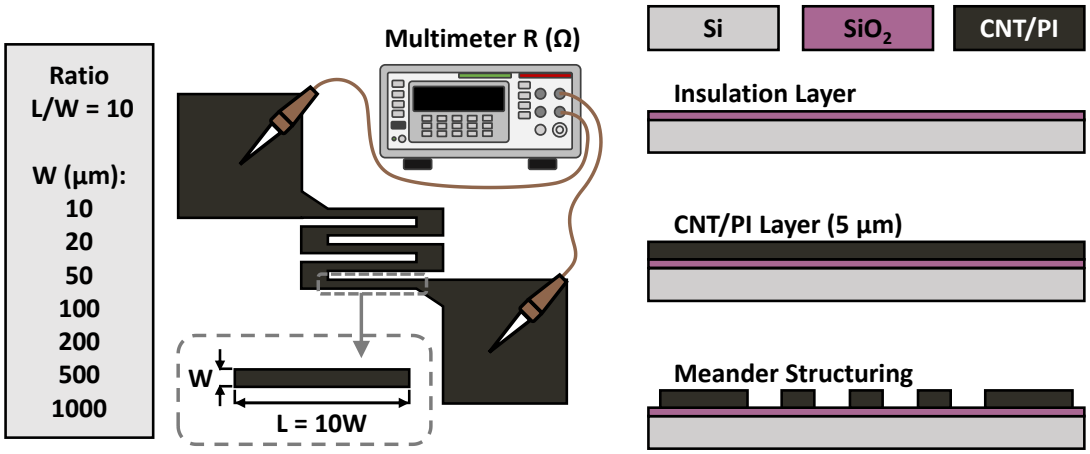

Fig. 7.2 Schema of structuring size test for CNT/PI films.

The CNTs and PI precursor were mechanically mixed and then spin-coated on oxidized silicon wafers for 60 s at 3000 RPM. The layer was thermally cured with a vacuum hotplate to obtain 5 µm thick CNT/PI films. The nanocomposite layer was coated with a 10 µm thick photoresist (AZ9260) for its UV-light exposure and development. The CNT/PI layer was etched using an O_2/CF_4 gas mixture by RIE, and the photoresist was later removed using AZ 100 Remover. This structuring process is represented in Fig. 7.2.

The second objective of the film structuring was the evaluation of the material homogeneity. Since all the meanders kept the same aspect ratio, they should theoretically have the same electrical resistance. This is exemplified by considering a single electrically resistive line with a length L, a width W, a thickness t, and the electrical resistivity ρ of the material. The electrical resistance of the line can be computed as:

$$R = \rho(L/A) \qquad \text{Eq. 7.1}$$

where A is the cross-sectional area of the line. However, Eq. 7.1 expression can be rewritten by considering the aspect ratio (length/width) of the line L/W = 10 and A = Wt:

$$R = (\rho 10W)/(Wt) = 10(\rho/t) \qquad \text{Eq. 7.2}$$

Since the aspect ratio of the lines is the same for all meander sizes, in the case of an ideal material, it would be expected that all structures have the same electrical resistance, as it only depends on the material thickness and its electrical resistivity.

After the electrical measurements, it was considered that meanders with a linewidth of 50 µm are the smallest reliable structures for a film with a 3 wt.% CNT content. Below this dimension parameter, most of the samples were above the measuring range of the multimeter. The

electrical resistance of the measurable samples (Fig. 7.3) ranged from 1.6 MΩ to 2.6 MΩ. The highest electrical resistance corresponds to the meanders with a linewidth of 50 µm, and the lowest value was achieved by the samples with a linewidth of 100 µm.

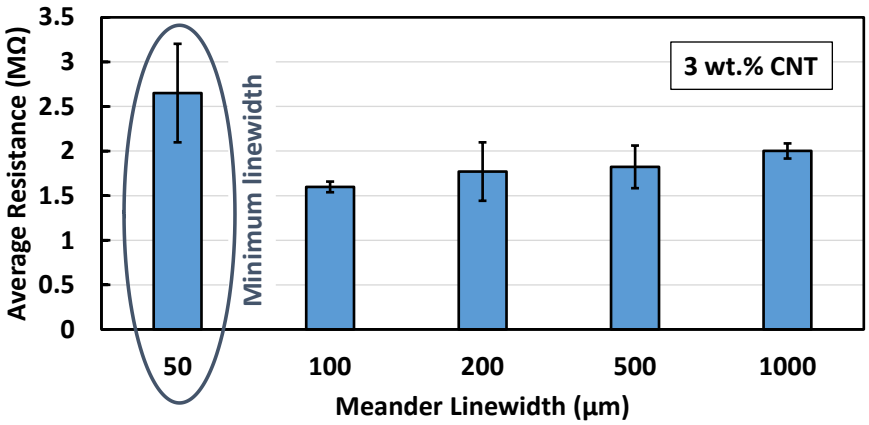

Fig. 7.3 Average electrical resistance of meanders as a function of the linewidth.

The variations of the electrical resistance between the structures are attributed to resistivity variations of the layer due to the use of a composite material rather than a single material. The high electrical resistance observed in structures with linewidth (50 µm and below) is because the homogeneity of the composite film can only be considered in a certain size range.

A macroscopic picture of a structured film with 3 wt.% CNT content is presented in Fig. 7.4. The figure includes two micrographs of structures with linewidths of 50 and 100 µm. Although the structures can be produced by the standard photolithography method, it was observed that the surface wafer has a noticeable roughness. Those spots are likely due to the masking effect of CNT clusters. Despite that, the electrical measurements indicated no electrical connection between the structures and the wafer surface.

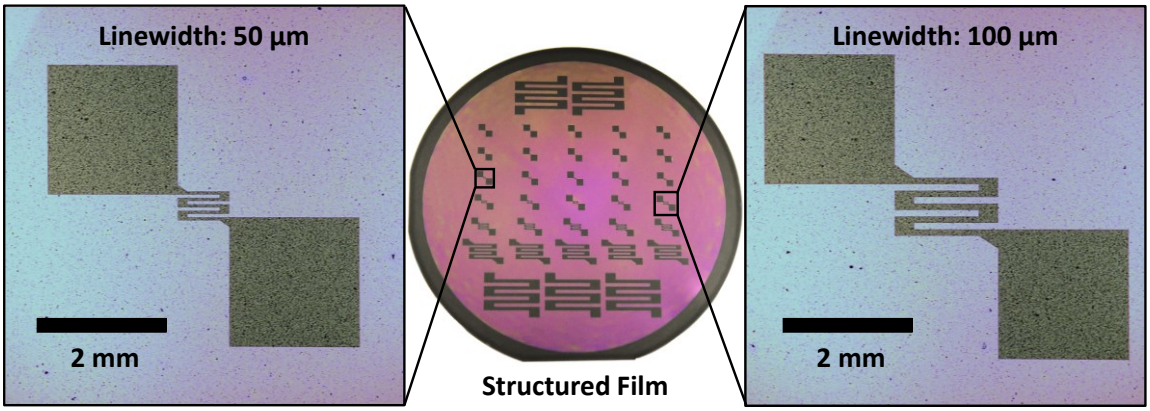

Fig. 7.4 Meander structures produced with a 3 wt.% CNT/PI film.

Meander structures with a 2 % CNT film were also produced, revealing that only a few of the large structures (500 and 1000 µm linewidth) are in the measurable range (R < 120 MΩ). Therefore, it was decided that the parameters for sensor fabrication are a meander with linewidths of 50 and 100 µm and a CNT concentration of 3 wt.% for the films.

7.3 First Design of the Strain Sensor

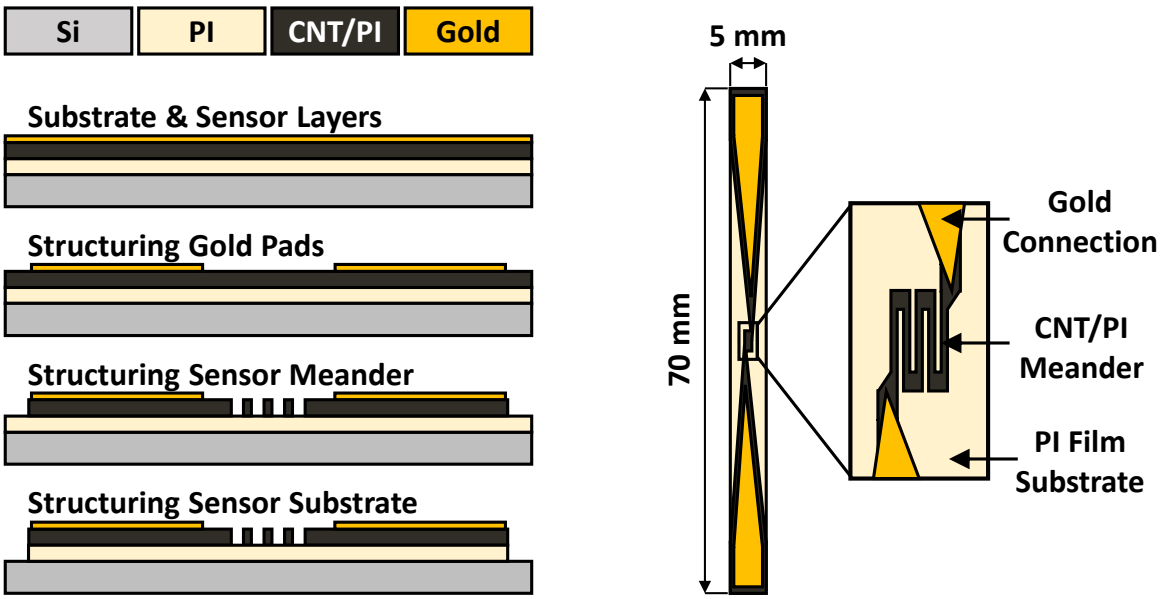

Fig. 7.5 Schema of sample fabrication and design for CNT/PI strain sensors.

The first generation of strain sensors was produced following the microfabrication parameters and the surface treatment previously presented. For this first version of the sensor, a polyimide layer (5 µm) was used as the substrate of the sensor, and a gold layer was used for electrical connection with the multimeter during the measurements. The schema of the microfabrication steps is shown in Fig. 7.5.

The PI substrate was produced by spin-coating the PI precursor on a silicon wafer for 60 s at 3000 RPM. The first PI layer was thermally cured in a vacuum hotplate and the material surface was treated using RIE oxygen plasma for 1 min and a bias power of 50 Watts, following the results of Chapter 2.

For the sensing layer, the PI precursor (15 g) was mechanically mixed with a load of 3 wt.% CNTs, using a mixing speed of 1200 RPM for 30 min, following the method of Chapter 4. The mixture was spin-coated on the plasma-treated substrate and thermally cured, using the same parameters for spin-coating and curing of the substrate.

A 100 nm thick gold layer was deposited by sputtering on top of the CNT/PI layer and structured using a 1.8 µm thick photoresist (AZ1518) and iodine solution as etchant. The photoresist was removed using AZ 100 Remover, leaving two contact pads for later electrical connections with a multimeter.

The meander structures were produced by photolithography with a 10 µm thick photoresist (AZ9260) and etched with O_2/CF_4 gas with the reactive ion etcher, using a slightly longer time (11 min) than for a pure PI layer to compensate for the slower etching rate. The photoresist was removed afterward with AZ 100 Remover. The photomask design had meander structures with 50 and 100 µm linewidths.

The last fabrication step made the rectangular shape of the PI substrate (70 mm length by 5 mm width), leaving the sensing structures in the middle section. The wafer was coated with a 20 µm thickness photoresist (AZ9260) and it was etched by RIE with O_2/CF_4 gas. Finally, the photoresist was removed from the wafer using AZ 100 Remover. After completing their fabrication, the rectangular samples were manually peeled from the wafer.

Optical microscope pictures of the produced samples are presented in Fig. 7.6, showing that the PI substrate had a rough surface, similar to that previously seen in Fig. 7.4. This was attributed to the presence of CNTs, especially their clusters, which left a rough surface after etching. However, the measurements of the electrical resistance between the pure PI layer and the sensing structures did not show any connection.

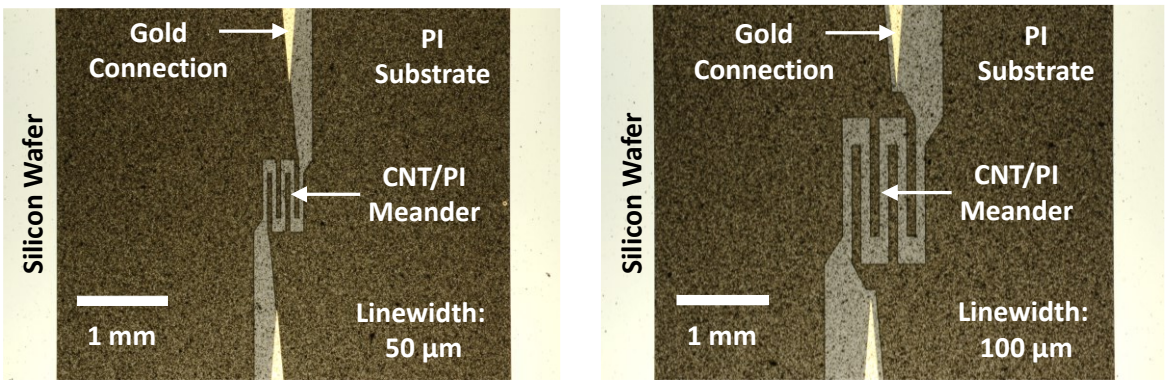

a) b)

Fig. 7.6 Micrographs of the CNT/PI strain sensor produced on PI substrate. a) Meander with 50 µm linewidth. b) Meander with 100 µm linewidth.

7.4. Piezoresistive Response of Strain Sensors

The sensors were tested under tensile force for characterizations with the Condor 100 XYZTEC bond tester. The gripper separation was 4 mm, and the speed for strain and return was 30 µm/s. The following strain levels were applied: ε = 0.25, 0.5, 0.75, 1, 1.5, 2 and 2.5 %, running ten cycles for each deformation level. The electrical resistance of the sensors was recorded with the digital multimeter Keithley 6500. Custom grippers with copper plates assisted with the connection between samples and the multimeter.

The initial resistance of samples was in the same range as the previous structures, and similarly, the smaller sensors had slightly higher values. After the normalization of their measurements as $\Delta R/R_0$ with $\Delta R = R - R_0$, it was noticed that the small meanders were about two times more sensitive than the larger ones. For example, for a deformation of ε = 1 %, the small sensor had a change $\Delta R/R_0$ = 36 %, whereas the larger changed only $\Delta R/R_0$ = 16 %.

Besides their higher sensitivity, it was noticed that the signal of the small structures was noisier than that of the large sensors. Furthermore, for strains greater than ε = 2%, the smaller sensors appear to have been partially damaged because their measurements became noisier, while the larger sensors were unaffected.

An actual sample during the characterization is shown in Fig. 7.7a, and its normalized resistance measurements are plotted in Fig. 7.7b. The average peak values $\Delta R/R_0$ were used to compute the gauge factor K (Eq. 1.2) of the samples, and they were plotted in Fig. 7.7c.

Similarly to the bulk films, the electrical resistance of the sensors increased with the strain. However, the meander structuring yielded higher sensitivity than the pure bulk film. For example, at the deformation of ε = 1 %, the gauge factor of films was K = 7.6, while a large structure sensor had a factor of K = 14, and the smaller meanders exhibited a factor of K = 33.6. This implied that in addition to a lower CNT concentration and thinner films, the structuring also increases the sensitivity of the samples, which agrees with the findings of Li [38], where meander-structured samples were more sensitive than patch-based sensors.

The smaller sensors showed the highest sensitivity of K = 64 at a strain of ε = 2 %. This result places this device in the upper range of sensitivities of the CNT-based sensors compiled in Table 7.1, only below the highly stretchable sensors based on elastomers. Therefore the fabrication of smaller structures can improve the sensitivity of the CNT/PI sensors.

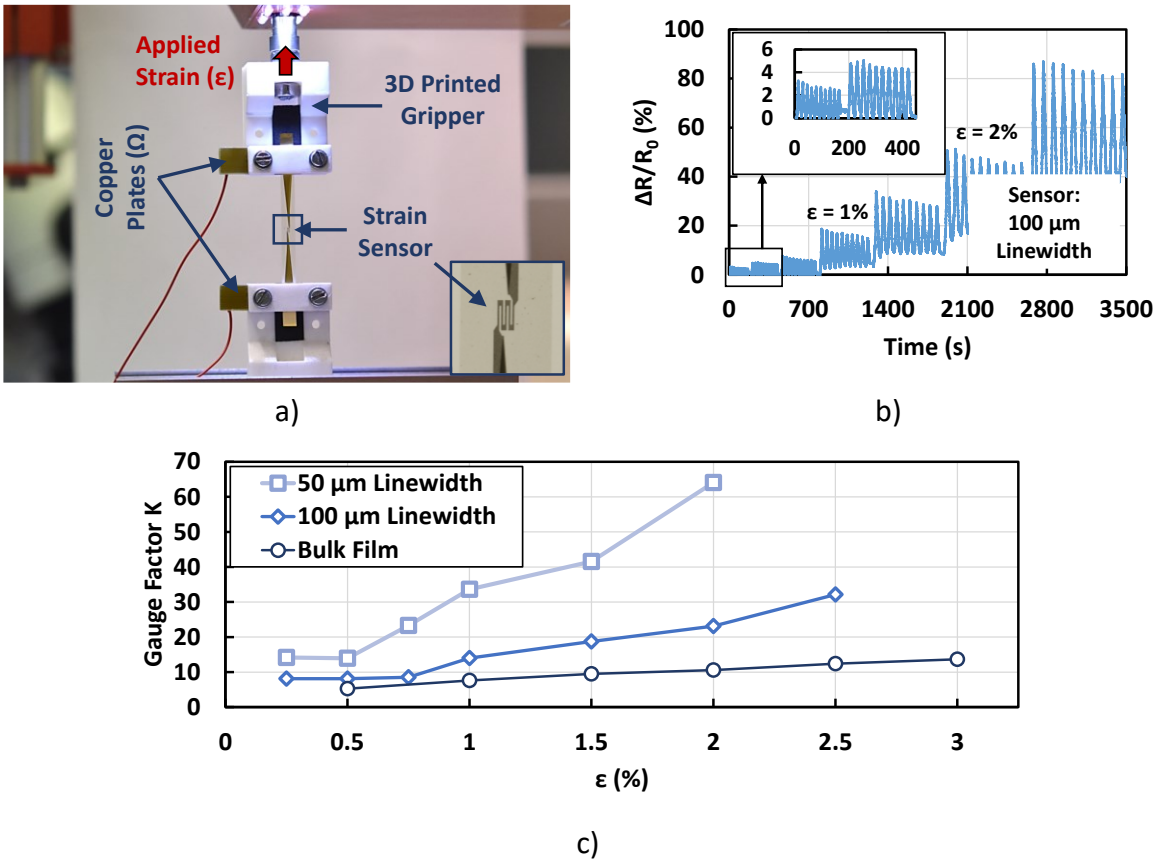

Fig. 7.7 Piezoresistive characterization of the meander-structured sensors. a) Experimental setup. b) Measurement for a 100 µm linewidth sensor. c) Comparison of gauge factor K between the sensors and the bulk film.

Another behavior observed during the strain test was the drift of the sensor signal, which was also previously observed on bulk films. This phenomenon was studied through cyclic strain tests considering two strain levels, ε = 0.5 % and ε = 1 %. The normalized measurements ($\Delta R/R_0$) of cyclic tested samples are plotted in Fig. 7.8a.

The normalized data showed that the signal dropped rapidly during the first 50 cycles. After that, the electrical resistance decreased slower and was fairly stable after 1000 cycles. These changes were easier to see by taking the peak values of the strain cycles as shown in Fig. 7.8b and Fig. 7.8c for samples deformed ε = 0.5 % and ε = 1 %, respectively. The corresponding force peaks were also normalized and included in the plots.

The normalized peak resistances showed that the electrical measurements tend to stabilize between 0.91 and 0.94 after 1000 cycles. Meanwhile, the mechanical data suggested that the samples slightly increased their stiffness during the first 500 cycles because the measured force increased. After that force increment, the peak forces were constantly reduced during

the remaining cycles, reaching a value of 0.65 for a deformation of ε = 0.5 % and 0.8 for a deformation of ε = 1 %.

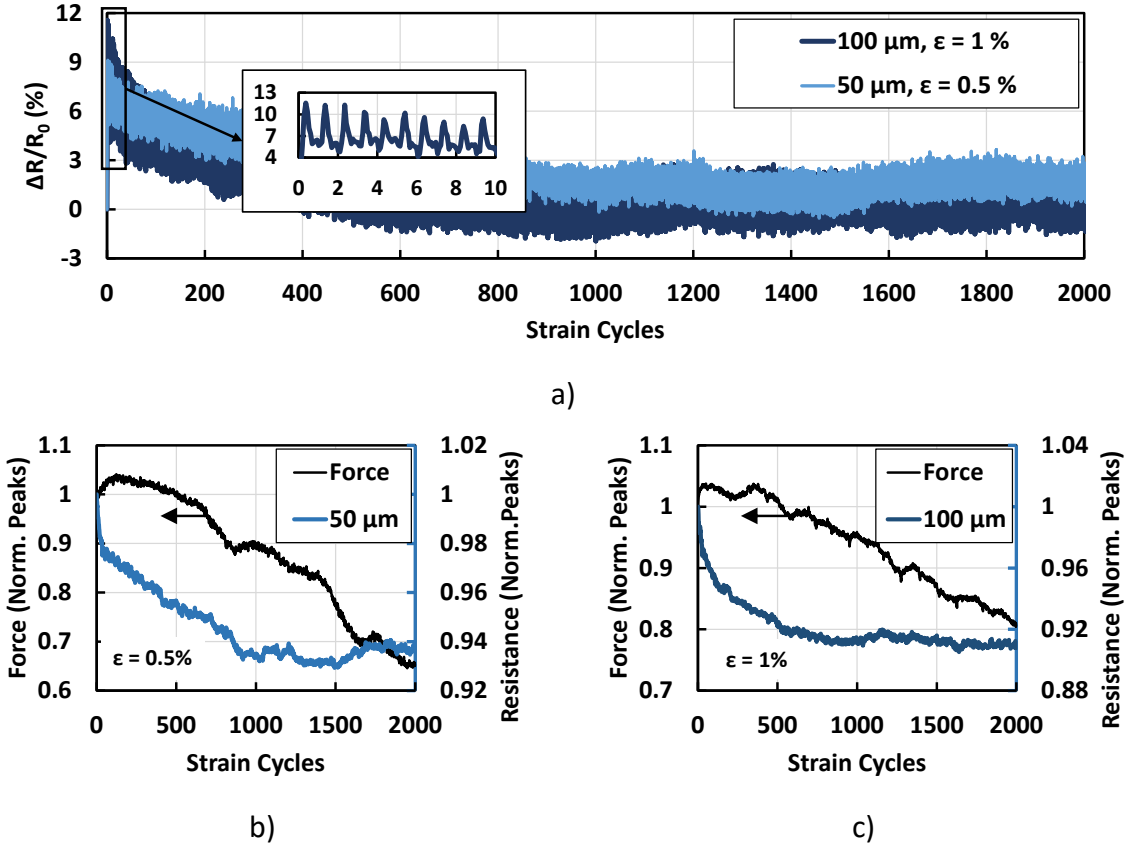

Fig. 7.8 Response of sensors under cyclic strain test. a) Normalized electrical resistance of samples. b) Normalized peak values for strain a ε = 0.5 %. c) Normalized peak values for a strain ε = 1.%.

The reduction in the peak forces could be caused by plastic deformations that accumulate during the cycles as represented in Figure 7.9a. At the beginning of the first strain cycle, the sample has zero deformation and zero stress σ, and then the sample is stretched up the maximum applied strain ε_A. However, after releasing, the strain at which the force drops to zero is not the same as at the beginning. This difference between the initial and final strains corresponds to the plastic strain ε_P. If this plastic deformation increases after each cycle, the elastic strain ε_E and the stress (or applied force) are reduced. This reduction in the elastic strain could also explain the reduction of the electrical measurements, due to the lower overall strain applied to the sensor.

The force and deformation data of all cycles were analyzed using a custom MATLAB script to search for the elastic ε_p and plastic ε_E deformations at each mechanical test cycle. The force

peaks and the elastic strains were normalized using their values of the first cycle and are presented in Figure 7.9b.

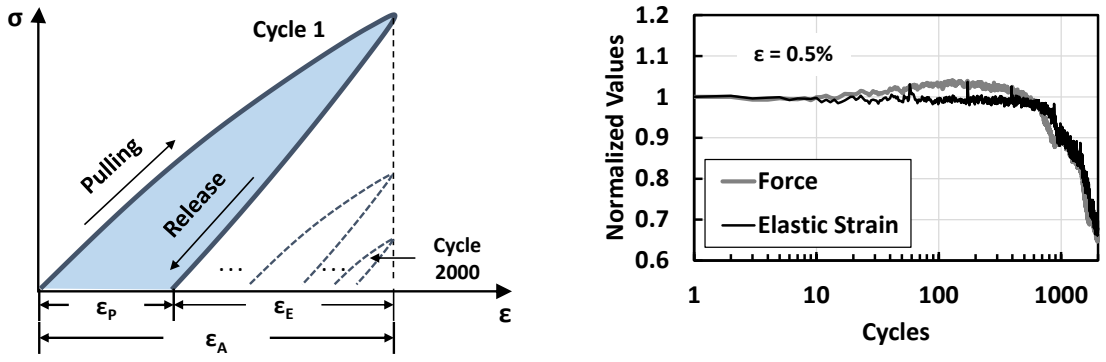

a) b)

Fig. 7.9 Mechanical behavior of the samples under cyclic test. a) Schema of the elastic and plastic deformations. b) Normalized force peak values and elastic strain during a cyclic test.

The extracted data showed that the elastic strain component was constant during the first 500 cycles, and only afterward there was a reduction. Therefore, plastic deformation is not the cause of the decrease in electrical resistance during the first 500 cycles. Other possibilities such as nanoparticle rearrangement [90] should be considered.

7.5. Temperature Response

For the thermoresistive characterization of the sensors, heating-cooling cycles were carried out. The sensors were attached to copper wires using silver glue. Then the samples were placed in a convection oven and heated up to 120 °C, simulating the curing cycle of the commercial carbon fiber/epoxy laminates. The electrical resistances were normalized according to their initial resistance at the beginning of the heating cycle.

As expected, the sensors exhibited a temperature dependence because their electrical resistance dropped with temperature. However, compared to the bulk films, the resistance change was lower because the maximum changes were around $\Delta R/R_0$ = -16 %, while the changes of the bulk films were $\Delta R/R_0$ = -19 %. In Fig. 7.10a, the thermoresistive responses of the sensors and bulk films are compared.

The average thermoresistivity coefficient α of the sensors was obtained following Eq. 6.3. As seen in Fig. 7.10b, both sensor sizes have similar coefficients α=-0.17 %/°C, the bulk film was α = -0.20 %/°C. This indicated that besides the material thickness, another factor influencing

the temperature sensitivity of the sample is the structuring, which could be exploited for applications with temperature sensors.

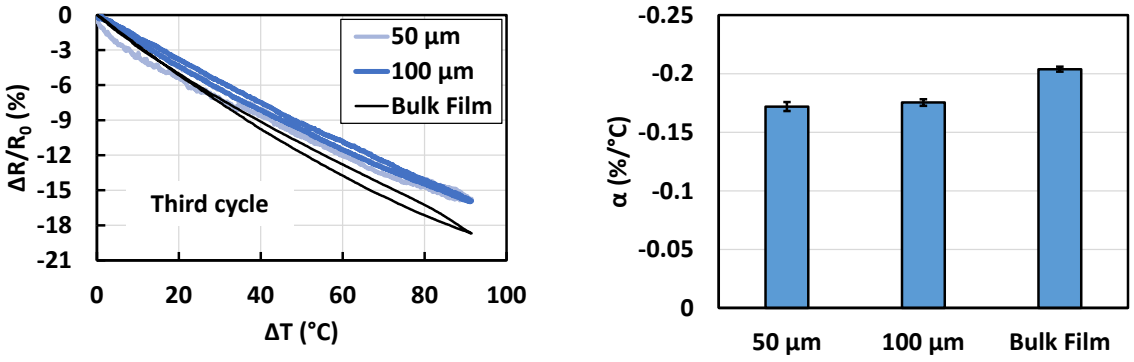

a) b)

Fig. 7.10 Thermoresistive response of sensors. a) Comparison of sensors for the third heating cycle. b) Average thermoresistive α coefficients.

Chapter 8: Sensor Integration into Fiber Composites

The final version sensor was embedded within carbon fiber/epoxy laminates as an example of an application. Design modifications for electrical insulation, size reduction, and resin flow were considered. During the cyclic strain test, commercial strain gauges were attached to the fiber composite samples as a reference.

8.1 Design of the Embedded Strain Sensor

Given that the aimed application is the measurement of the strain of carbon fiber composites, a modification of the original sensor design was required. The size of the sensor substrate was reduced to a rectangle of 30 by 5 mm, and a second top polyimide layer was added for electrical insulation purposes (see schema in Fig. 8.1). Another modification was the removal of the gold used as connections to the meander structures because the adhesion of polymer on gold is rather poor. For this new version, gold was used only for the contact pads to connect the copper wires to the measuring device.

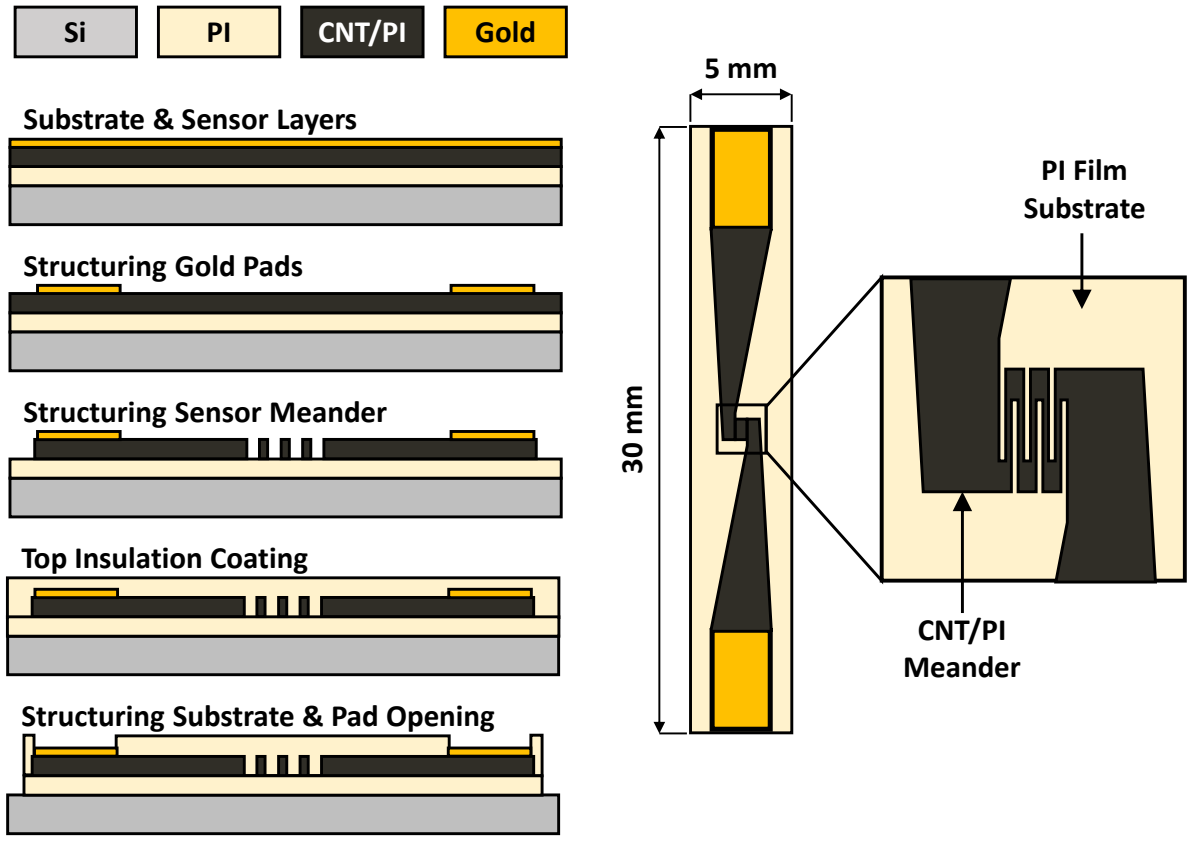

Fig. 8.1 Design and microfabrication steps of the sensors for embedding.

Further changes in this design iteration included wider connections to the sensing structures and circular holes of 100 µm diameter in the sensor substrate to allow the resin flow of the fiber composite. This change aims at improving the sensor integration into the fiber composites [7,100].

The first step for microfabrication consisted of a polyimide layer (5 µm) produced by spin-coating of the PI precursor at 3000 RPM for 60 s on a silicon wafer without adhesion promoter and thermally cured. This first layer works as the sensor substrate and its bottom insulation.

The surface of the first PI layer was activated with RIE oxygen plasm, then a mixture of CNT/PI at 3 wt.% CNT was spin-coated and thermally cured, producing a sensing layer of 5 µm. For fabrication of the rectangular connection pads (2.9 by 4.9 mm), gold was sputtered with a thickness of 100 nm and structured with photoresist AZ1218 (1.8 µm thick) and an iodine solution for etching. After pads structuring, the photoresist was removed using AZ 100 Remover.

The piezoresistive layer (CNT/PI) was structured using a 10 µm thick photoresist AZ9260. The sensing layer was etched by RIE with the O_2/CF_4 gas combination. Two meander sizes were produced, with linewidths of 50 and 100 µm and an aspect ratio length/width = 10. After removal of the photoresist, the sensor polymer surfaces were treated using the RIE oxygen plasma method. The third PI layer (5 µm) or top insulation was spin-coated and thermally cured using the same parameters as the first layer.

The final shape of the sensor was a rectangle of 30 by 5 mm. The wafer was coated with a thicker 20 µm photoresist layer (AZ9260). The etching through the sensor layers was carried out by RIE with the O_2/CF_4 gas. The gold pads worked as a stop layer for the etching of the top PI insulation of those areas.

The samples were manually peeled from the silicon wafer using small tweezers. Two copper wires (0.15 mm diameter) were attached to the gold pads using a silver glue Elecolite 327. The wire connections were covered with an epoxy resin and UV-light cured to provide electrical isolation before embedding the sensors.

8.2 Fabrication of Carbon Fiber Composites and Sensor Embedding

Commercial unidirectional carbon fiber/epoxy prepregs (Panex 35 50k) were obtained from UNIPREG to fabricate composite laminates with 10 layers. The prepreg was cut to obtain rectangular layers of approximately 25 by 27 cm. The vacuum bag method was used to produce unidirectional (0°) composite plates (see schema in Fig. 8.2). The layers were stacked on top of a metal plate as a support covered with a release layer, and the sensors were placed on top of the fifth prepreg layer following the fiber orientation. A set of 3D printed templates assisted the alignment of the sensor and the copper wires.

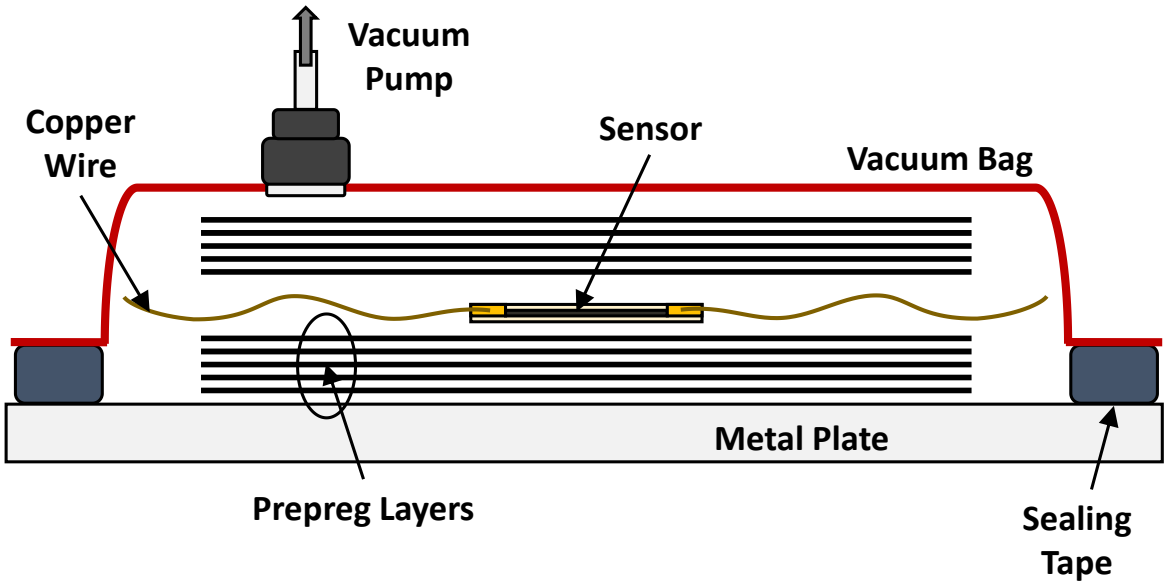

Fig. 8.2 Schema of the vacuum bag method for the fabrication of fiber composites.

After coverage of the sensors with the remaining prepreg layers, a sealing tape was applied around them to place the sealing bag on top. The bag was connected to a vacuum pump using a through valve, and the material was placed inside a convection oven. The curing process was carried out at 120 °C for 2 h, following the curing temperature profile of the manufacturer. The placing of the sensors during the fabrication of fiber laminates is shown in Fig. 8.3. The micrograph of a sensor with a linewidth of 50 µm shows the patterned holes for resin flow.

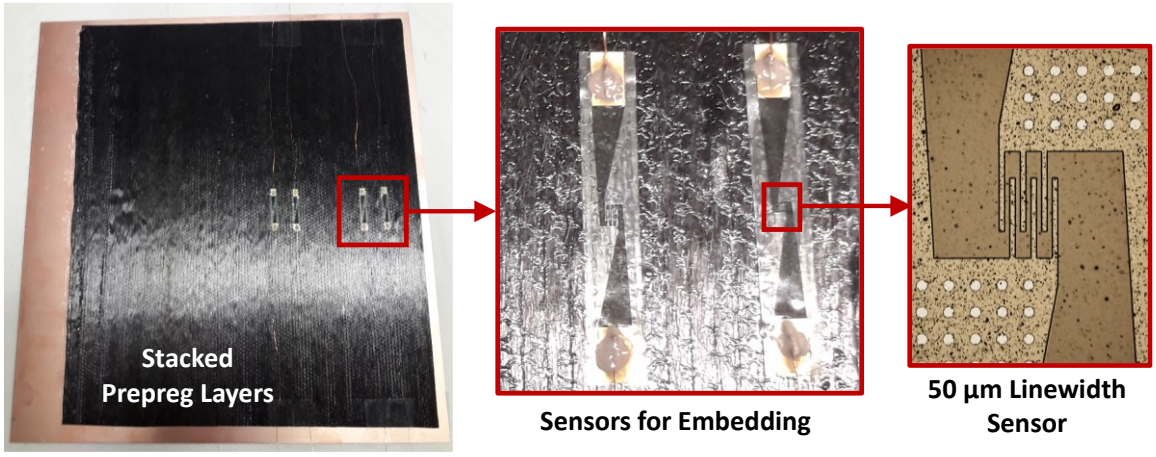

Fig. 8.3 Embedding process of CNT/PI sensors within carbon fiber laminates.

For the tensile characterization, the fiber composite laminates were cut following the ASTM norm D3039 [101]. Rectangular specimens were produced with a length of 250 mm, a width of 15 mm, and a thickness of 1.5 mm. The edges of the samples were sanded and glass fiber tabs (56 mm long and 1.5 mm thick) were glued using a two-component epoxy glue. The specimen geometry and a set of finished composite samples are presented in Fig. 8.4a and Fig. 8.4b, respectively.

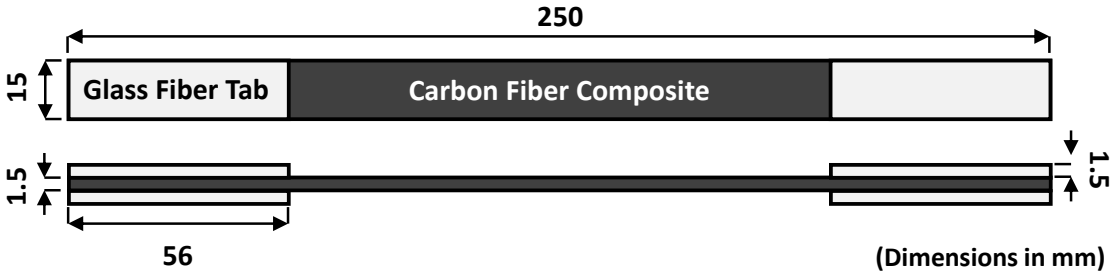

a)

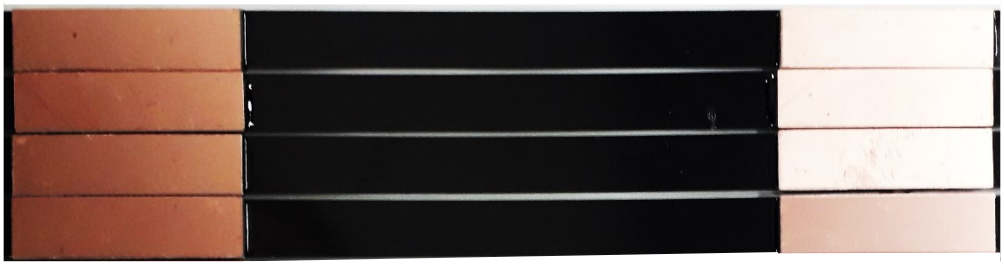

b)

Fig. 8.4 Fiber composites for tensile test. a) Sample dimensions. b) Finished samples.

After manufacturing samples for the tensile test, a commercial strain gauge (HBM 350Ω, K = 2.1) was glued on the specimens as a reference sensor. The fiber composite samples were tested with a pneumatic testing machine DYNA-MESS with a load cell of 10 kN, configured for

a cyclic tensile test by force control. The force program was a sine function with a frequency of 0.1 Hertz and 9 kN peak-to-peak amplitude. The program ran for 1000 cycles and the electrical resistance of both CNT/PI and commercial sensors was recorded with a multimeter Keithley 6500.

A few samples without embedded elements were tested as reference material. A picture of an actual sample is presented in Fig. 8.5a, while representative force and strain plots are presented in Fig. 8.5b. The force was obtained from the testing machine, while the strain was measured with the commercial strain gauge. Measurements indicated that a force of 9 kN produced a strain ε = 0.35 %. This was approximately half of the strain measured by the machine, showing that an external sensor is required for measurements.

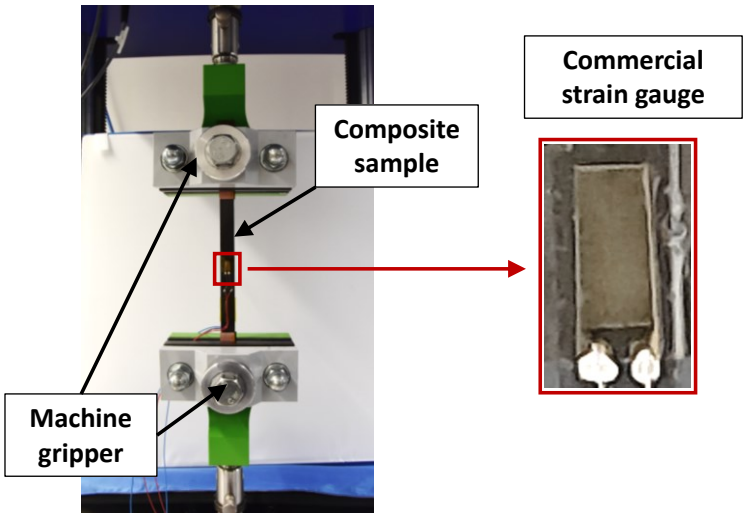

a)

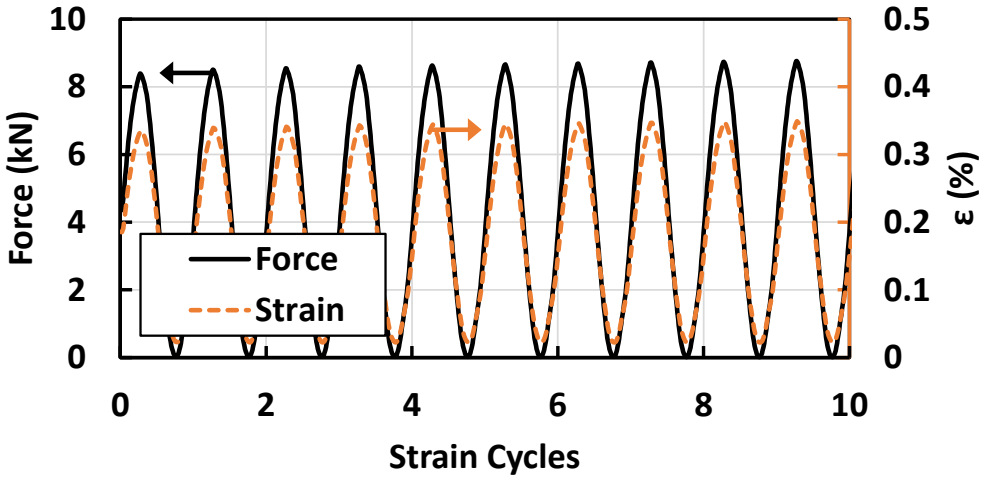

b)

Fig. 8.5 Mechanical characterization of carbon fiber composites. a) Picture of an actual sample. b) Force and strain cyclic curves.

8.3 Response of the Integrated Sensors

A few sensors survived the steps from fiber composite fabrication until the manufacture of samples for the tensile test. Sample handling was challenging as the copper wires of other sensors were damaged during the release of the compound from the vacuum bag or when cutting the material to its final geometry.

The electrical resistances of the surviving sensors were similar to the measurements before their embedding (MΩ range). This agrees with temperature experiments performed with some non-embedded sensors, which indicated that electrical resistance is recovered after cooling. In those experiments, the curing process cycle of fiber composites was simulated by heating the samples at 120 °C for 2 h in a convection oven. The plot in Fig. 8.6 presents the resistance changes $\Delta R/R_0$ during two heating cycles.

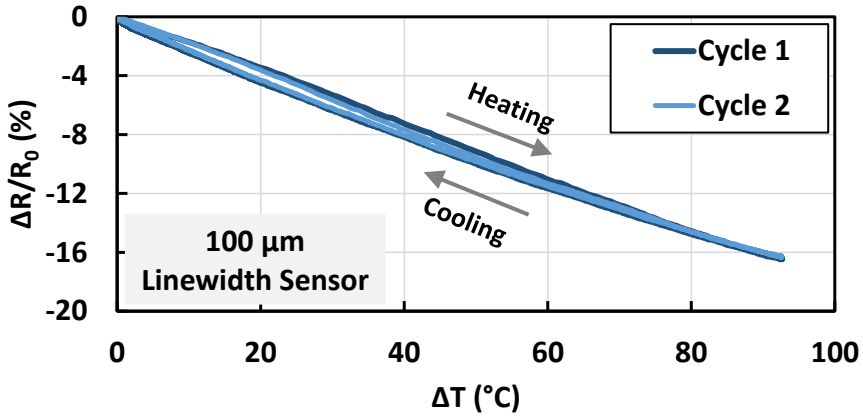

Fig. 8.6 Temperature response of a non-embedded sensor with top PI insulation.

The strain and force measurements of composite samples with and without embedded sensors were similar, indicating that the embedded sensors had no impact on the mechanical properties of the fiber composites under the selected testing conditions. The samples were tested under a cyclic force test with a 9 kN peak-to-peak amplitude, and the electrical resistance data of the embedded sensors was normalized, i.e., $\Delta R/R_0$.

An example of the normalized data of the sensors is presented for 200 cycles in Fig. 8.7a, and the first 10 cycles are plotted in Fig. 8.7b. The plots showed that the CNT/PI sensors have a significantly higher sensitivity than the commercial strain gauges. The smaller sensor was the most sensitive, although its signal was also the noisiest. For example, the commercial strain

gauge had a maximum resistance change of $\Delta R/R_0$ = 0.7 %, while the large embedded sensor exhibited a change of $\Delta R/R_0$ = 1.2 %, and the smaller one showed a change of $\Delta R/R_0$ = 1.7 %.

The gauge factor of the embedded sensors was computed by taking the peak values of the normalized electrical resistance during the first 20 strain cycles. For the corresponding strain measurements, the data from the commercial sensors was used instead of the direct data from the testing machine. The extracted gauge factors K are presented in Table 8.1.

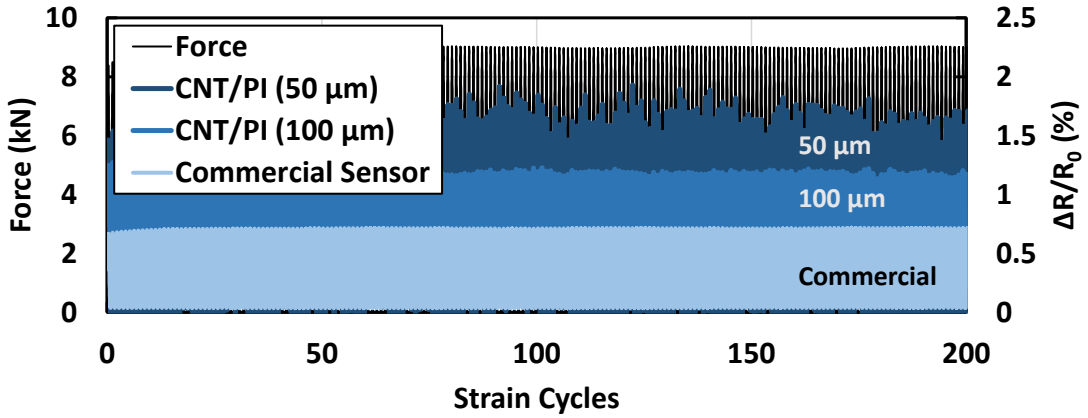

a)

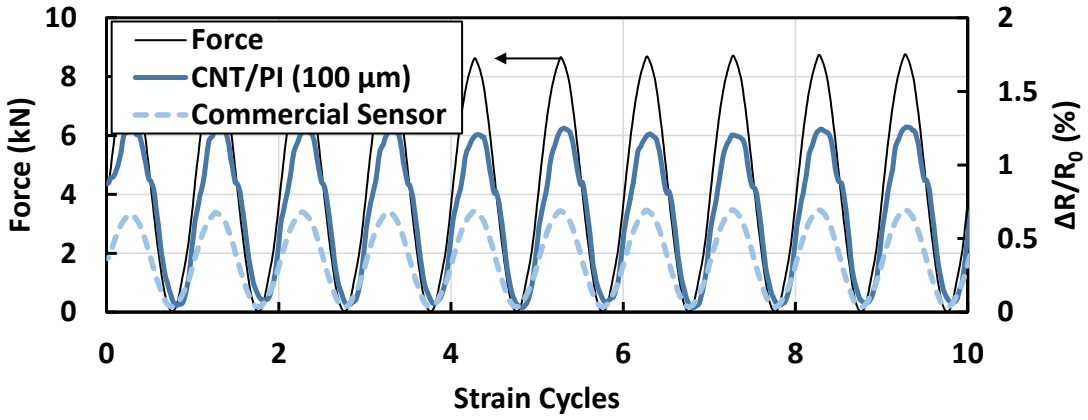

b)

Fig. 8.7 Piezoresistive response of embedded CNT/PI sensors. a) Measurements of two sensors for 200 cycles. b) Response of the 100 µm linewidth sensor under 10 cycles.

Table 8.1. Gauge factors of the embedded sensors within fiber composites.

Sensor linewidth (µm)	Embedded sensor (with top insulation)	First sensor design (without top insulation)
100	3.6	8.1
50	10.7	14.2

Although the sensitivity of the embedded sensors is higher than the commercial strain gauge, their gauge factors K were lower than those obtained with the previous sensors without the top PI insulation. This lower sensitivity could be attributed to several factors. For example, the strain measurements used an external sensor instead of the measurements of the testing machine. Another consideration is that the embedded sensors have an additional PI layer, which may influence their overall mechanical properties. Other possibilities are defects during the embedding or a poor adhesion to the fiber composites that could lead to inadequate transfer of the forces from the host composite. An attempt to find a possible explanation for the lower sensitivity of the embedded sensors is presented in the following sections.

8.4 Characterization of Non-embedded Sensors

For a fair comparison between the sensors with and without the top PI layer, a batch of long samples (70 by 5 mm) with top PI insulation was produced for piezoresistive characterization without embedding. The specimens did not have patterned voids in the body since they were fabricated based on the design explained in section 7.1, but adapted for connection tracks without the gold layer.

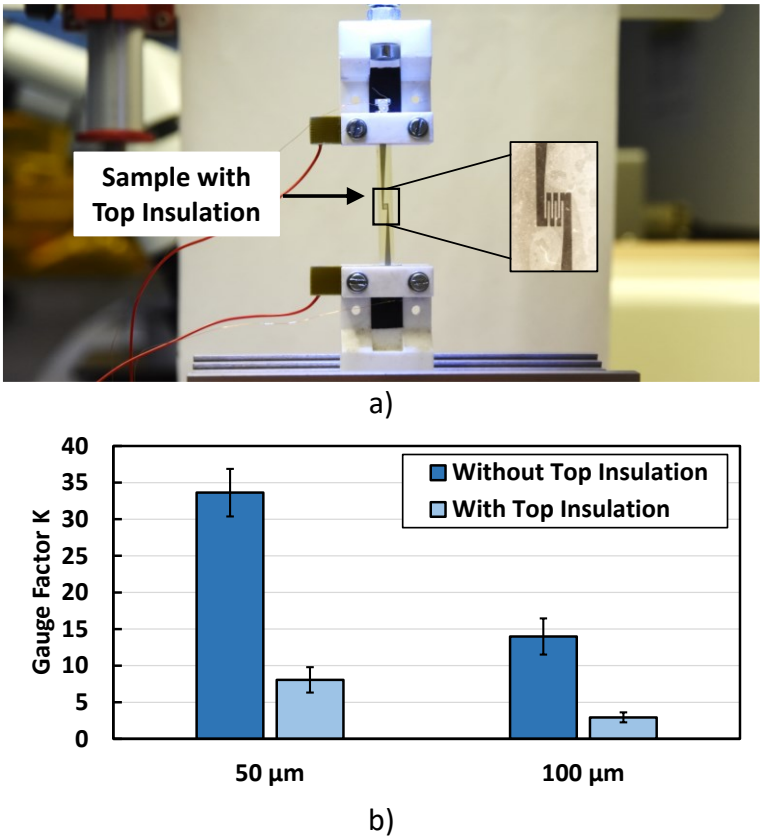

Fig. 8.8 Piezoresistive characterization of sensors without embedding. a) Picture of sample during the test. b) Gauge factors of samples with and without top PI insulation.

To discard the possible influence of the method for strain measurement, the samples were tested with a bond tester (Condor 100 XYZTEC), and their strain data was taken directly from the machine. The specimens were fixed with grippers with a separation of 40 mm, following the characterizations in section 7.4. After normalization of their electrical resistance, the average gauge factor K of the samples was computed for a strain of ε = 1 %. A sample with top PI coating during its characterization is shown in Fig. 8.8a, and the gauge factors for sensors with and without top PI insulation are plotted in Fig. 8.8b.

After the piezoresistive characterization of the sensors with the top PI layer, it was observed that their strain gauge factors were still lower in comparison to the sensors without the top PI insulation. However, the gauge factors were in the range of the values observed in embedded sensors, and they followed the trend of higher sensitivity with the smaller sensors. This suggested that the methodology used for strain measuring was not the explanation for the lower gauge factor of the sensors, and further analysis is required.

8.5 Strain Modeling of the Sensors

The design of the sensors for embedding added a top PI layer for electrical insulation purposes. However, it was suspected that this layer could influence the mechanical behavior of the samples. Therefore, a model was proposed as a tool to study the strain of the different sample designs.

Taking firstly the sample design without top PI coating, the model considered a 70 mm length and 5 mm width specimen, fixed between two grippers with a 40 mm separation. The grippers apply a force F and their deformations are neglected, producing only the deformation of the specimen portion between them. The model is represented in Fig. 8.9.

One specimen section was simplified as a three-layered composite with perfect adhesion between the layers. The first layer corresponds to the PI substrate, the second layer represents the CNT/PI film, and the third layer is the sputtered gold. Each material layer has an elastic modulus E1, E2 and E3. The cross-sectional area of the layers is simplified as constant, represented as A1, A2 and A3.

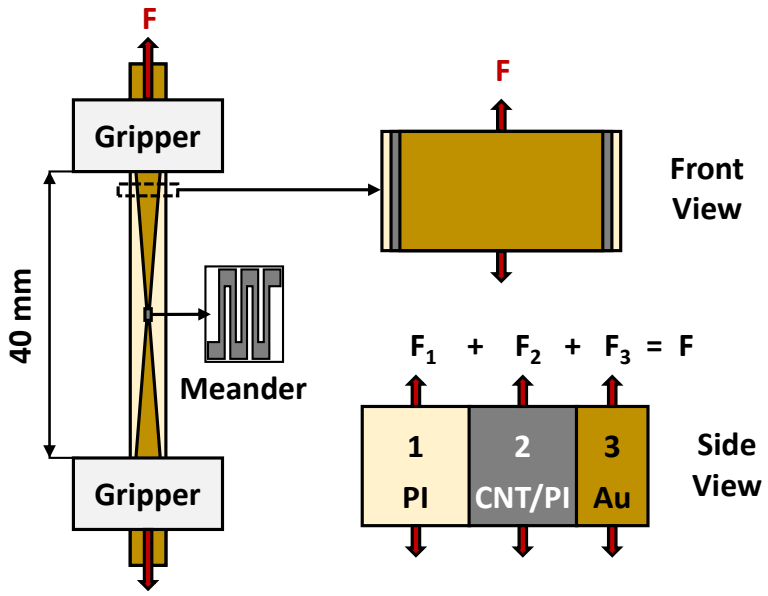

Fig. 8.9 Schema of the three-layered model for computation of strains.

Each layer of the model is under a force F1, F2 and F3, respectively. However, since the complete section is under a total force F, the sum of forces is written as:

$$F = F_1 + F_2 + F_3 \qquad \text{Eq. 8.1}$$

By taking the expression $\sigma = \varepsilon E$, which relates the stress σ, the strain ε and the material elastic modulus E, the stress of each layer can be represented with the following expressions:

$$\begin{aligned} \sigma_1 &= \varepsilon_1 E_1 \\ \sigma_2 &= \varepsilon_2 E_2 \\ \sigma_3 &= \varepsilon_3 E_3 \end{aligned} \qquad \text{Eq. 8.2a-c}$$

However, the definition of stress σ in a material with a constant cross-section is $\sigma = F/A$, and it can be used to compute the stress of each layer as:

$$\begin{aligned} \sigma_1 &= F_1/A_1 \\ \sigma_2 &= F_2/A_2 \\ \sigma_3 &= F_3/A_3 \end{aligned} \qquad \text{Eq. 8.3a-c}$$

The Eq. 8.2a-c can be combined with the Eq. 8.3a-c, producing a new expression for the force on each material layer:

$$\begin{aligned} F_1 &= \varepsilon_1 E_1 A_1 \\ F_2 &= \varepsilon_2 E_2 A_2 \\ F_3 &= \varepsilon_3 E_3 A_3 \end{aligned} \qquad \text{Eq. 8.4a-c}$$

If the Eq. 8.4a-c is substituted in the Eq. 8.1 for the force, it leads to:

$$F = \varepsilon_1 E_1 A_1 + \varepsilon_2 E_2 A_2 + \varepsilon_3 E_3 A_3 \qquad \text{Eq. 8.5}$$

Since a perfect adhesion between the layers has been considered, the strain of the analyzed section is the same for each layer, leading to:

$$\varepsilon_{Local} = F/(E_1A_1 + E_2A_2 + E_3A_3) \qquad \text{Eq. 8.6}$$

In the last expression, ε_{Local} represents the local strain experimented by the sample section. The sample was divided into 1 µm length sections to compute their local strain ε_{Local}, producing the plot in the Fig. 8.10. For this strain simulations, the force F was adjusted to produce a total deformation of ε = 1 % of the 40 mm length section between the grippers, which represents the data recorded by the machine during the characterizations. This modeling approach was also applied to samples with a top PI coating and single-material specimens, their simulations are included in the plot.

The mechanical properties considered for the model layers were an elastic modulus E_1 = 9.80 GPa [21] for the PI substrate and E_3 = 78 GPa [102] for the gold. The thickness of the PI substrate and the PI/CNT film was 5 µm and 100 nm for the gold. The width of the PI substrate had a constant value of 5 mm, while the PI/CNT and gold layers had a lineal function with a maximum width of 3.4 mm close to the grippers and a minimum width of 0.3 mm at the center of the sample. For the CNT/PI layer, the elastic modulus was considered as $E_2 = 1.4E_1$, since the previous characterizations showed that the stiffness of the CNT/PI films was increased.

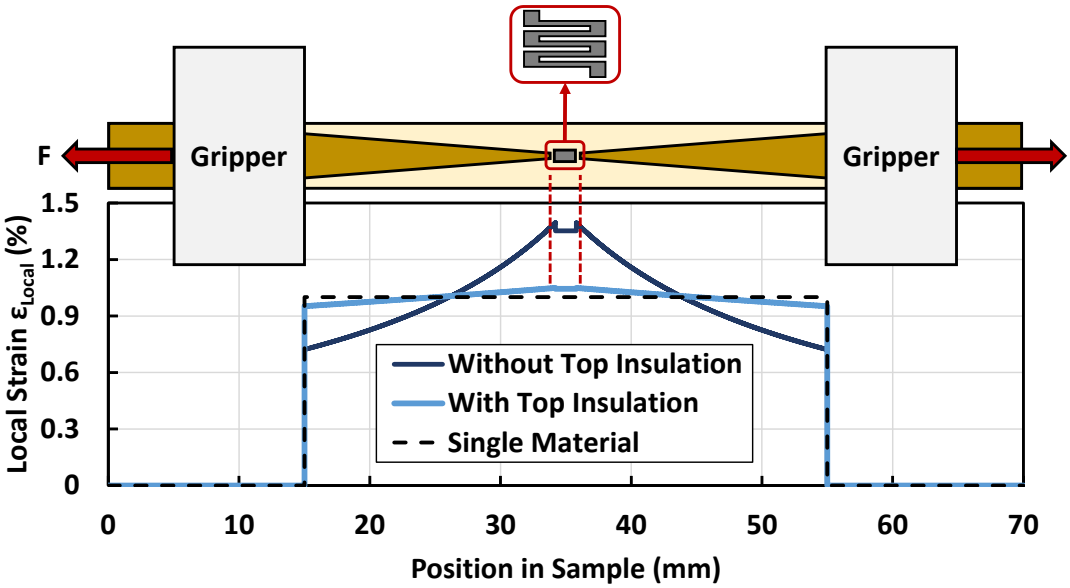

Fig. 8.10 Simulation of the local strain of the sensors.

For the simulation of a sample with top PI coating, the data for PI (E_1 = 9.80 GPa) was used for the substrate, the top PI coating and the gap filling of the CNT/PI layer. For the CNT/PI layer, a value of $E_2 = 1.4E_1$ was considered. For this simulation, the gold was discarded because it was only used for the pads at the end of the samples.

In the case of a sample produced with a single material, the simulation of strains considered only the elastic modulus of a PI layer E_1 = 9.80 GPa.

The model without top PI insulation indicated that the lowest local strains are produced in the region in contact with the grippers, which is ε_{Local} = 0.72 %. When moving towards the central section of the sample, the local strain increased non-linearly, reaching a maximum ε_{Local} = 1.4 % where the meander structures are located.

This phenomenon is attributed to the narrowing of the cross-section of the CNT/PI layer towards the center of the sample. Therefore, although the total strain of the whole sample was ε = 1 %, it is higher in the middle of the specimen.

If the sample has a top PI coating, the strain variations are reduced, approaching the results of a sample produced with a single material and a uniform cross-section (dashed line). The upper layer of PI can compensate for changes in the cross-sectional area of the sample, and lower local stress is applied to the meander structure, which explains the lower changes in electrical resistance.

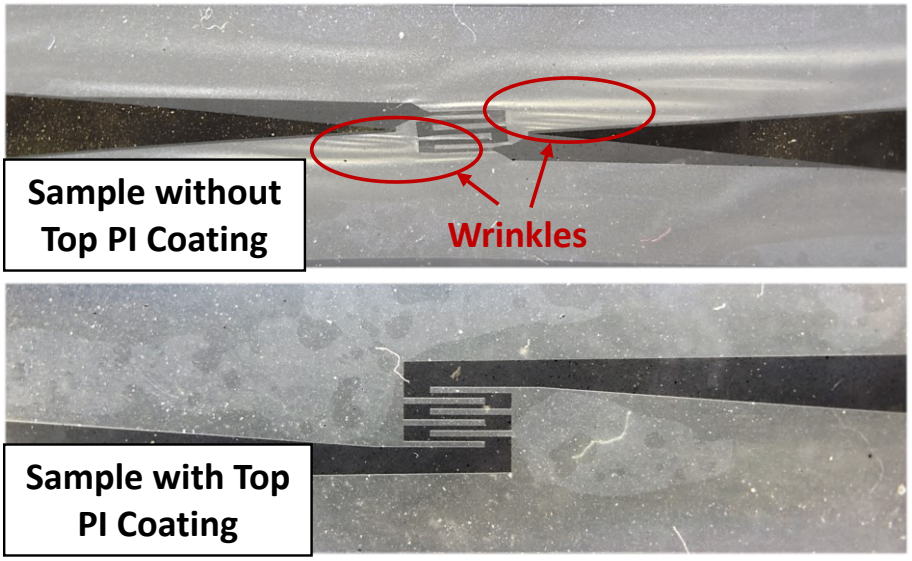

Fig. 8.11 Micrographs of samples after piezoresistive characterization.

These results also explain why wrinkling was observed at the central section of some samples without top the PI coating, which likely resulted from the larger deformations produced in that location. A comparison of sensors with and without top PI coating after their characterizations is presented in Fig. 8.11. The sample without the top PI layer showed marked wrinkles close to the meander structure, while the sensor with a top PI coating presented a smooth section.

Chapter 9: Cure Monitoring of CNT/PI Films

The use of the CNTs in this work aimed at the development of a piezoresistive polymer film, which was later used to fabricate strain sensors. However, the literature has highlighted CNTs as a potential tool to monitor the curing process of epoxy resin. This has been accomplished by embedding glass fibers grafted with CNTs [103,104] and CNT fibers or yarns [105]. Since the resin modifies the CNT network during its infusion and curing, a change in the electrical resistance of the fibers can be correlated to the curing steps of the material.

In this chapter, the electrical resistance change of a CNT/PI film was used to monitor its thermal curing. The following results were presented at the Conference: M. Cen-Puc, M.G. Vargas Gleason, A. Schander, W. Lang, Online Cure Monitoring of Carbon Nanotube/Polyimide Films, in: 2022 IEEE Sensors, IEEE, Dallas, TX, USA, 2022: pp. 1–4.

9.1 Fabrication of the Sensing Electrodes

For the cure monitoring of the PI/CNT films, gold interdigital electrodes were produced on oxidized silicon wafers. The oxide layer worked as an electrical isolation between the silicon wafer and the CNT/PI film. To enhance the adhesion between the silicon wafer and the gold electrodes, a 15 nm thick chromium layer was sputtered. Then, the gold layer was sputtered with a thickness of 100 nm and structured with a 1.8 µm thickness photoresist AZ1518. The etching of the gold and chromium layers was performed using iodine solution and chrome etchant 3144, respectively.

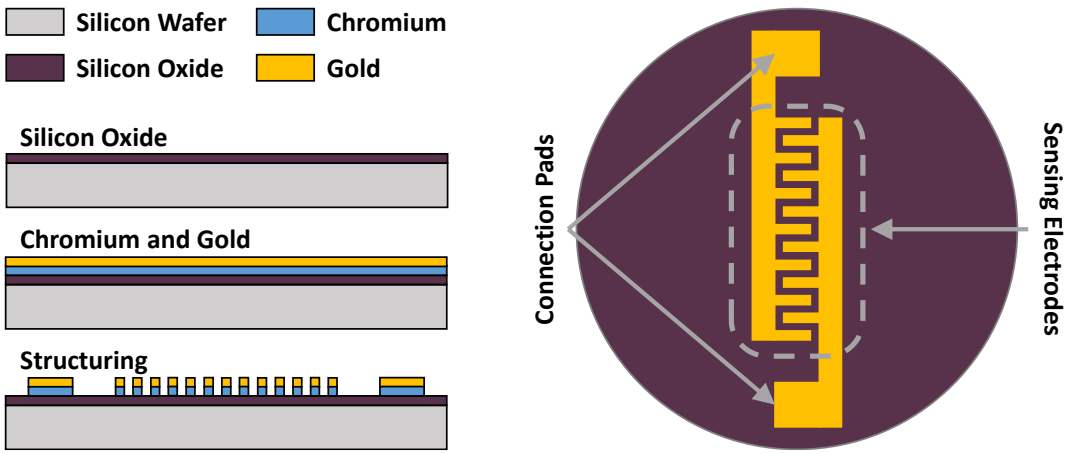

Fig. 9.1 Structuring of electrodes for curing monitoring of films.

After removing the photoresist using AZ 100 Remover, the produced structures were interdigital electrodes with 2 mm width, 8 mm length and 2 mm spacing. The total sensing area was 5 x 2 cm, aimed to register the bulk electrical resistance of the film. The structuring is represented in Fig. 9.1. After fabrication of the sensing structures, two 90° male pins were attached to the connection pads (1 by 1 cm) using a silver glue Elecolit 327.

For proof of concept of the cure monitoring, a polyimide mixture with 3 wt.% CNT was produced using the mechanical mixing method. The wafer with the sensing electrodes was coated with the polymer mixture at 3000 RPM for 60 s and placed in a vacuum hotplate for thermal curing of the film. A multimeter (Keithley DMM6500) was connected to the male pins with small metal clamps to measure the electrical resistance of the film. The measurement setup is represented in Fig. 9.2.

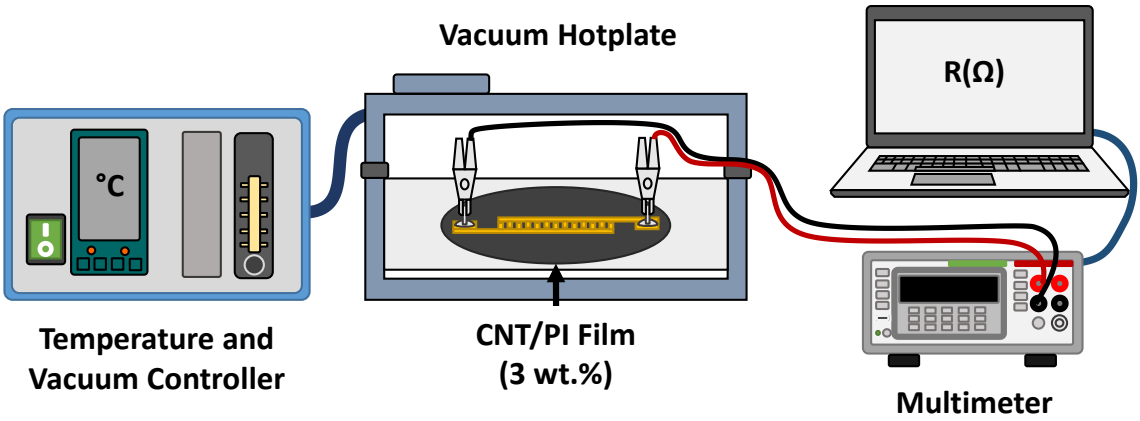

Fig. 9.2 Setup for the measurement during the thermal curing of CNT/PI films.

9.2 Electrical Resistance Changes of CNT/PI Films

The electrical resistance of the film exhibited drops of the electrical resistance during the curing process. The first and largest change occurred during the first temperature step at 120 °C. In this temperature step, the electrical resistance dropped from a value above the measuring range of the multimeter (120 MOhm) to only 8 kΩ. After that, the electrical resistance continued to decrease at each temperature step, reaching a minimum of 470 Ω at the final curing step (450 °C).

Measurements of CNT/PI films are presented in the Fig. 9.3a. The sample A was a film measured during its thermal curing and the sample B was a previously cured one. Their plots show that they behave differently. A picture of a cured film is presented in Fig. 9.3b.

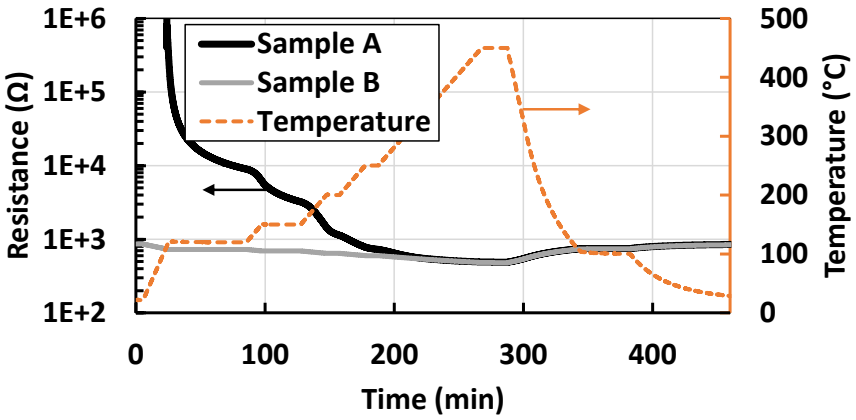

a)

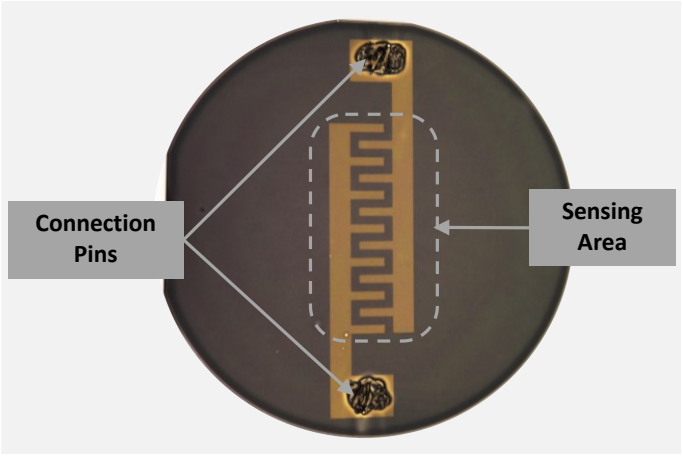

b)

Fig. 9.3 Electrical resistance monitoring of CNT/PI films. a) Measurements during the thermal curing of films. b) Example of a cured wafer.

Given the different behavior of the cured samples, a possible explanation for the electrical change is the solvent evaporation. This can be seen in further heating cycles applied to cured films (Fig. 9.4), showing a similar behavior as described previously in Chapter 6.

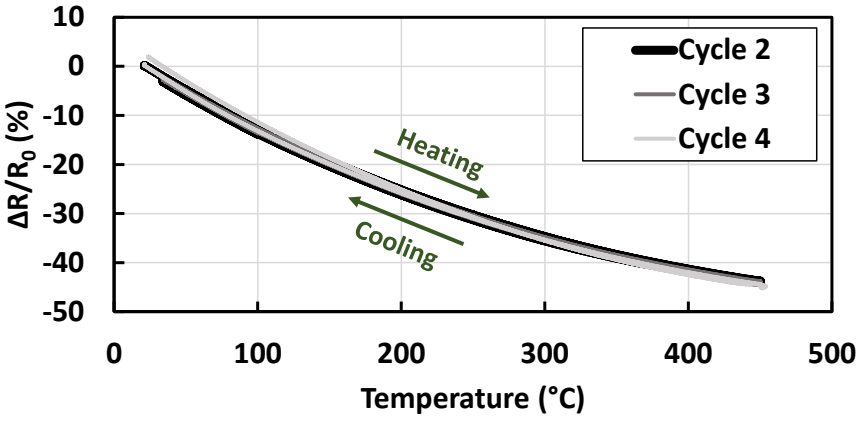

Fig. 9.4 Electrical resistance of a cured CNT/PI film during temperature cycles.

9.3 Solvent Evaporation and Curing of Films

To find the relationship between the solvent evaporation and the electrical resistance, silicon wafers were coated with PI and partially cured up to different temperature steps. The weight of the films was measured before and after partial curing to compute the solvent loss.

The film weight indicated that the most significant mass loss was produced at the temperature step of 120 °C, losing 70 % of the initial weight. The weight continued to reduce and reached a constant value of 18 % at 250 °C. This final weight agrees with the solvent content (82 %) mentioned by the manufacturer [21]. The film weight and the electrical measurements during the curing are plotted in Fig. 9.5.

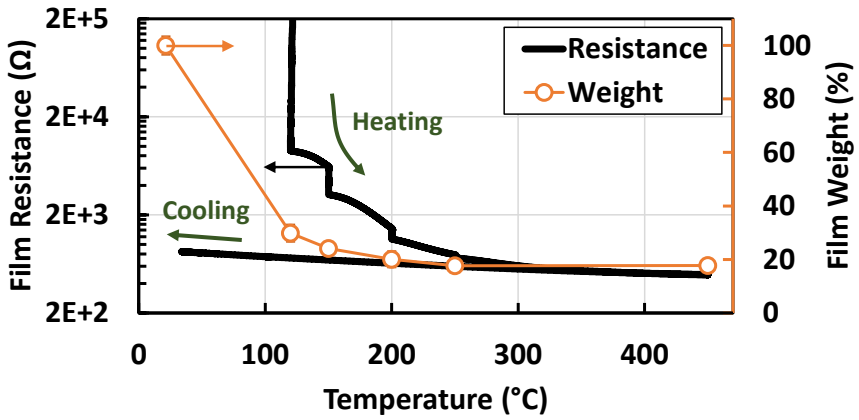

Fig. 9.5 Weight and resistance changes of films during the curing steps.

The derivative of the electrical resistance was used to describe the changes in the electrical resistance of the sample, showing some peaks during the curing of the film. The sample A in Fig. 9.6 corresponds to a sample during its thermal curing, whereas the sample B refers to a previously cured film.

The first and largest peak of the derivative plot resembles the thermogravimetric analysis reported by Gräbner [106], where the mass loss had a peak close to 100 °C. A close look at the derivative plot in Fig. 9.6b showed a second peak between 150 °C and 250 °C that agrees with the expected curing temperature of the polymer, which when analyzed by differential scanning calorimetry, shows a peak close to 200 °C [106]. Interestingly, one last small peak was also observed between 250 °C and 350°C, which could be correlated to post-curing.

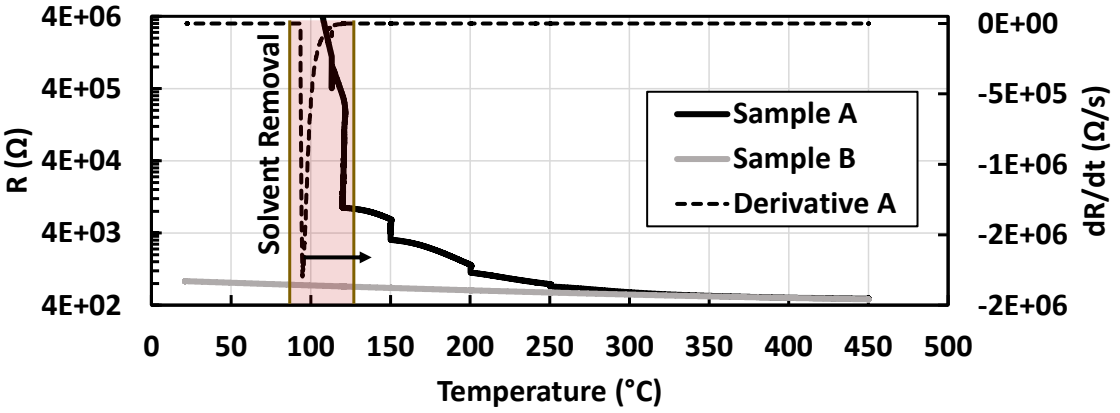

a)

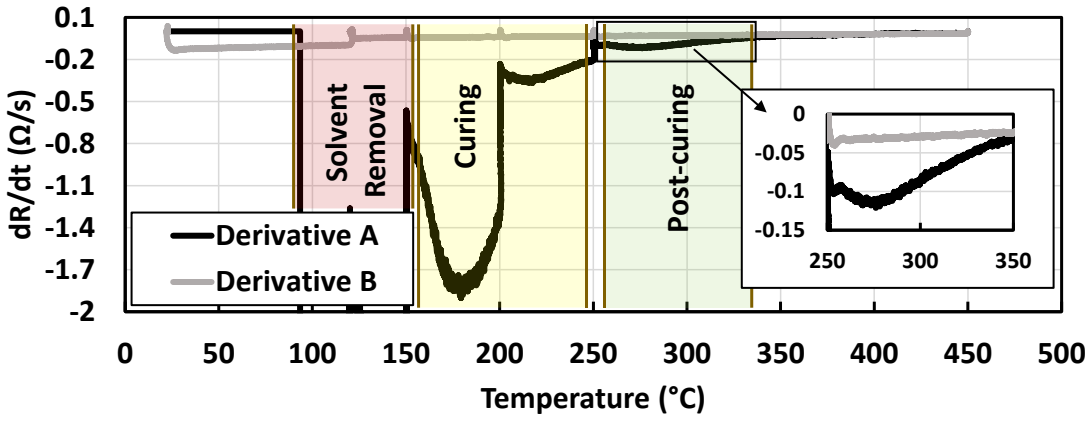

b)

Fig. 9.6 Derivative plot of the electrical resistances of films. a) Peak related to solvent loss. b) Peaks related to curing phases of the film.

The peaks described above were not observed in previously cured samples, indicating a highly potential application of the electrical resistance measurements to monitor the different curing stages of the CNT/PI films.

9.4 Connection Model of CNTs during Film Curing

The solvent present in the film represents 82% of its initial weight, so the volume of the film is reduced after its evaporation. This material shrinkage is expected to lead to the compaction of the CNT network inside the polymer, increasing the CNT-to-CNT connections and thus reducing its electrical resistance.

To simulate this effect, a 2D model was developed in MATLAB, following the Montecarlo approach for the percolation modeling in Chapter 3, but modified to include the solvent

volume. The area of the model was adjusted to different amounts of solvent based on the weight measurements, and it is represented in Fig. 9.7.

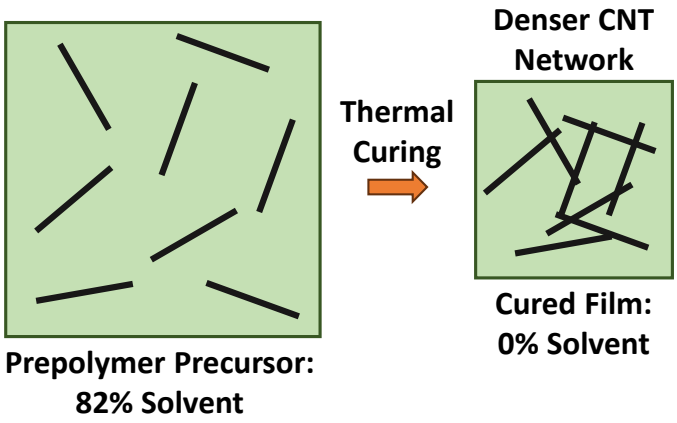

Fig. 9.7 Schema of the CNT network compaction during the film curing.

The number of CNTs in the model was set to 100 nanoparticles to compute their volume and mass, which allowed the calculation of the mass of the PI for a particle loading of 3 wt.% CNT. Various solvent contents were used for the model, from a polymer precursor with 82 % solvent to a cured film with 0 % solvent. The material densities were 2100, 1100 and 1028 kg/m^3, corresponding to the CNTs, PI and the solvent (NMP), respectively.

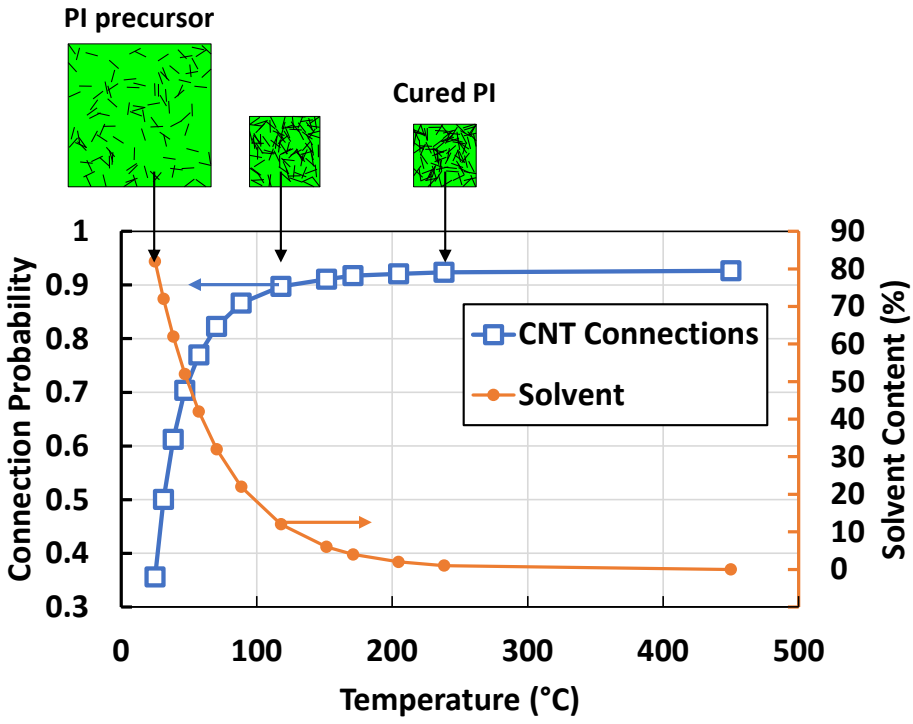

Fig. 9.8 Simulation of CNT-to-CNT connections during the curing of films.

The CNTs were randomly generated as lines inside the model area, and the CNTs connected to another CNT were counted. The simulation ran 1000 times to obtain the connection probability plotted in Fig. 9.8. The solvent content of the film was included in the plot.

The simulation indicated that the number of connected CNTs increases with solvent removal due to densification of the CNT network. At the beginning of the thermal curing, the connection probability was 34 %, and it reached 90 % at 120 °C. After 200 °C, the connection probability saturated.

The findings coincided with the changes in the electrical resistance of the films during the first part of their curing. Therefore, the compaction of the nanoparticle network due to solvent evaporation was responsible for the largest drop of the electrical resistance of films.

Conclusions and Outlook

Conclusions

The main objective of the project was the development of strain sensors based on a carbon nanotubes/polymer thin film. This piezoresistive material was proposed as an alternative to typically used metal layers in order to reduce the foreign body effect. As a proof of concept for sensor integration, the device was embedded to detect deformations of carbon fiber composites.

The first part of the work addressed the adhesion of polyimide films, treating the material surface with alkaline solutions and oxygen plasma. The wettability of all the treated films was increased. However, the 180° peel test indicated that the best adhesion was produced by reactive ion etching plasma, with a power of 50 W for 1 min.

Models were developed to predict the electrical behavior of the films. The resistor model and rule of mixtures predicted electrical conductivities close to graphite for high nanoparticle contents, and the Montecarlo model predicted an electrical percolation threshold of 0.1 % nanotube weight content. The experimental results agreed with percolation predictions.

For the fabrication of the piezoresistive layers, carbon nanotubes were dispersed within the polymer using ultrasonication and direct mechanical stirring. The ultrasonication method had several challenges, requiring a solvent combination (acetone and dimethyl sulfoxide), an evaporation step and partial curing of the layers. On the other hand, the direct mechanical mixing produced a better and faster dispersion of the nanoparticles.

Experiments with graphenic materials for polyimide layers were unsuccessful. The percolation simulations indicated a high particle content and therefore the material was discarded.

The piezoresistive capabilities of films indicated that a 1.5 - 3 % nanotube range content is preferred due to the low electrical resistance. Low nanotube content films were more sensitive to strain, but thinner layers were also more sensitive than thicker films. The selected films for sensor fabrication had a 3 % nanotube content and a thickness of 5 µm, based on processing compatibility and its gauge factor K = 7.6. However, the material sensitivity is non-linear and temperature-dependent, which should be considered for real applications.

The microfabrication for the nanotube/polyimide films by photolithography showed that meander structures with lines of aspect ratio length/width = 10 and linewidths as small as 50 µm are feasible. The first version of sensors (without top polyimide isolation) was proposed with meander structures with a linewidth of 50 µm and 100 µm. The smaller sensors had higher sensitivity (K = 33.6) than the larger ones (K = 14).

The second version of the sensor was embedded within carbon fiber/epoxy resin composites. The sensors had a top polyimide coating for electrical insulation and patterned voids for resin flow. However, their sensitivity was lowered due to the top isolation, the smaller sensor had an average gauge factor K = 10.7, and the larger one K = 3.6. Still, the results showed that nanotube/polyimide film sensors have higher sensitivity than the commercial ones (K = 2).

Additional experiments for monitoring the thermal curing of nanotube/polyimide films showed that this material combination can detect the different curing steps, which may be helpful in the fabrication of parts based on this or even other polymers.

Outlook

Additional experiments combining thinner layers and lower nanotubes contents could be evaluated to improve the sensor sensitivity. Another possibility is the manufacture of other sensor geometries that could allow the use of lower particle concentrations or the use of smaller structures.

Sensor integration into fiber composites is particularly challenging and experiments are needed to investigate the functioning of embedded sensors in more detail. Fatigue or stability tests could also be performed on carbon fiber parts.

Appendix A: Further Results of PI Surface Modification

A.1 Stability of Surface Treatments for PI Films

For a long stability test of PI surfaces, the wettability by the water contact angle of treated PI films was characterized for 14 days (Fig. A.1). During the testing period, the samples had no special storage conditions to evaluate the aging of activated surfaces.

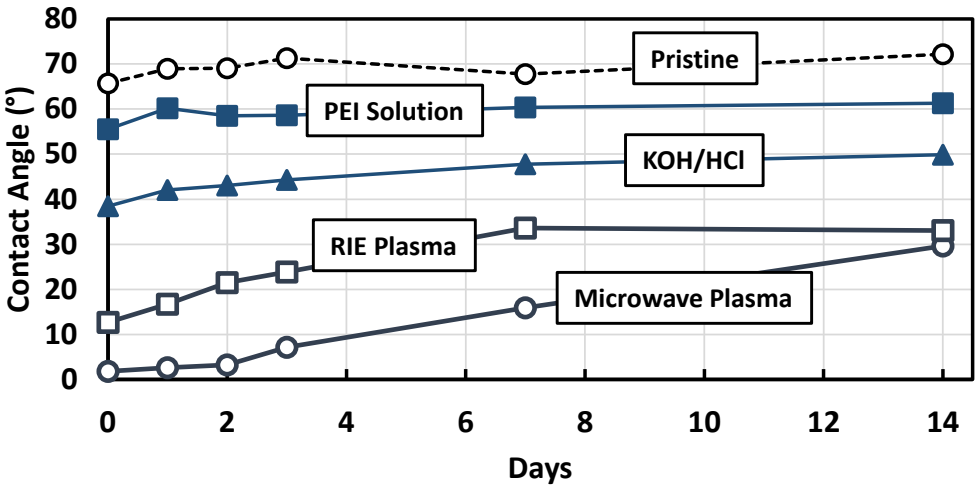

Fig. A.1 Wettability change of PI films for 14 days.

The measurements indicated that all samples reduced their wettability, because their contact angle increased over time. Moreover, the PI films seemed to stabilize after 14 days at a lower angle than the pristine PI films. This suggested that a relatively long-term modification of the polymer surface was produced by the treatments.

A.2 Scratch Test for PI Films

Although the 180° peel test (Chapter 2) quantitatively evaluated the PI layer adhesion, a scratch test [107] of the top PI layer was also explored for a faster adhesion test.

After the fabrication of the first PI layer, its surface was treated and a second PI layer was applied. The top PI layer was cured and structured with O_2/CF_4 by RIE. The structures of the top PI layer were circles (750 µm diameter), which were manually scratched with a needle. The structuring of the samples is represented in Fig. A.2.

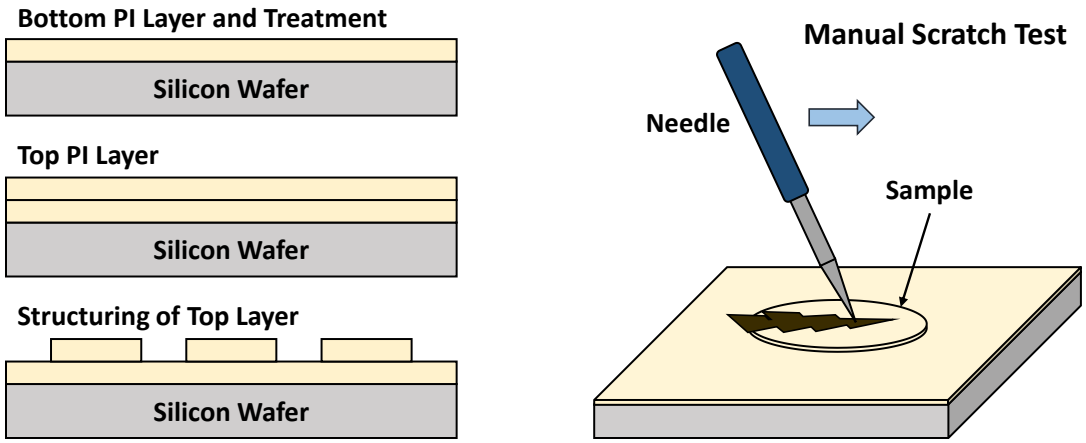

Fig. A.2 Schema of samples fabrication for manual scratch test.

The structures of reference films (untreated) were easy to remove and a smooth surface indicated the lack of layer adhesion. The samples treated by PEI behaved like the pristine films, with no significant adhesion between layers. The samples modified by KOH/HCl were more difficult to remove and left surface marks due to better adhesion. The samples treated by microwave plasma showed no noticeable adhesion. Finally, the RIE-treated samples were not able to peel and they were torn. Therefore, RIE plasma was the best treatment for the films. Micrographs of samples are shown in Fig. A.3.

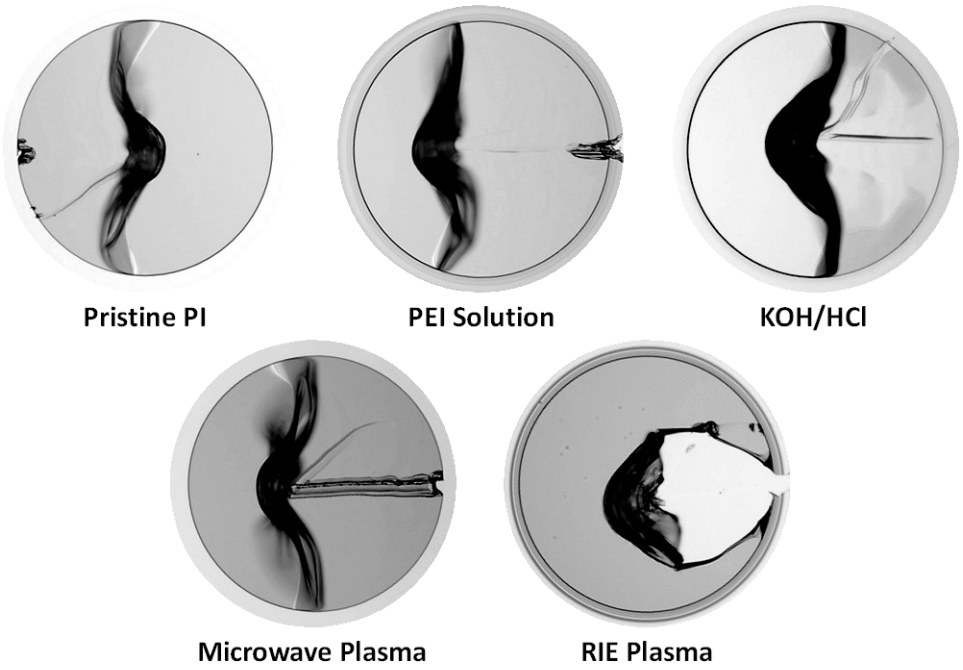

Fig. A.3 Micrographs of PI layers after manual scratching.

Appendix B: Literature Review of CNT/PI Films

A review of published works on the topic of CNT/PI films was collected and is presented in Table B.1. The information included the relevant data for the present research: the film type (thin film <100 um) if available, the type of CNT used for the film, the nanoparticle treatment if used, the dispersion method for the CNTs, the percolation threshold achieved and the maximum CNT content.

The data of the table is presented in weight percentage wt.%, but if the published works provided original data in vol.%, the conversion relations of vol% = wt% and vol% = 2 wt% were used for SWCNT and MWCNT [29], respectively.

Table B.1 Overview of published works on CNT/PI.

Film type	**CNT type**	**Dispersion method**	**Percolation threshold (wt.%)**	**Maximum CNT content (wt.%)**	**Ref.**
Thin Film	SWCNT & MWCNT	Ultrasonication	0.15	5	[85]
Thick Film	MWCNT	Melt Mixing	0.8	7	[108]
Thin film	SWCNT	Ultrasonication	0.05	1	[109]
Thick? Film	MWCNT	Ball Milling	1	3	[110]
Thin? Film	MWCNT (oxidized)	Ultrasonication	1	5	[111]
Thin Film	MWCNT	Ultrasonication	0.3	7.4	[112]
Thin Film	SWCNT (oxidized)	Ultrasonication	0.3	1	[113]
Thin? Film	MWCNT (oxidized)	Ultrasonication	7	12	[114]
Thick Film	SWCNT	Ultrasonication	1	2	[115]
Thin Film	SWCNT	Ultrasonication	0.04	2	[116]
Thin Film	SWCNT	Ultrasonication	0.08	9	[117]
Thick Film	MWCNT	Melt Mixing (Roller blades)	0.8	7	[118]
Thin Film	MWCNT (Plasma Treated)	Ultrasonication	0.1	3	[119]

Thin Film	MWCNT	Surfactant	1	3	[120]
Thin Film	MWCNT (Plasma Treated)	Ultrasonication	0.05	0.4	[121]
Thin Film	MWCNT	Ultrasonication	0.6	5	[122]

From the information above, it was noticed that most of the published works used MWCNT rather than SWCNT for the fabrication of PI films, and that the ultrasonication method for CNT dispersion is preferred. Therefore, ultrasonication dispersion was suggested as a first approach for the fabrication of the CNT/PI films.

The published works reported percolations between 0.04 and 7 wt.%. By taking the percolation threshold and the number of publications, the plot of Fig. B.1 was produced. It can be noticed that most of the works reported a percolation threshold of below 1 wt.%, and it seems to be independent of the CNT type or the nanoparticle treatments. This data also agrees with the Montecarlo simulations and the conductivity of the CNT/PI films in this work.

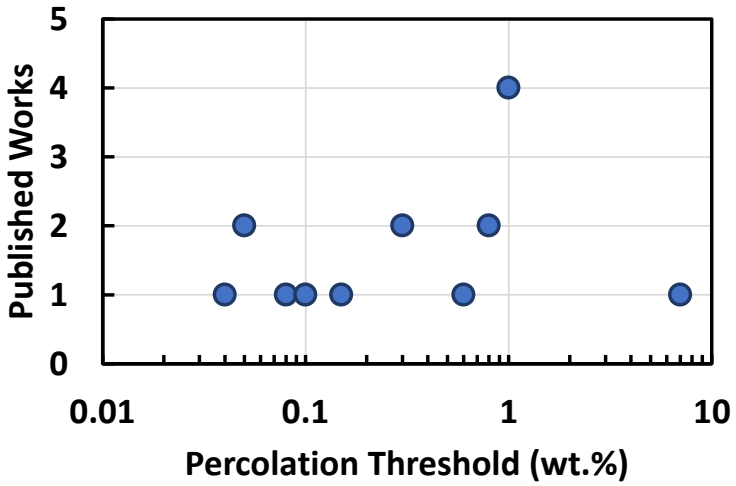

Fig. B.1 Published works per percolation threshold of CNT/PI films.

Appendix C: Design of 3D-printed Tools

C.1 Mechanical Design of Grippers

Due to the small PI samples of this work, customized grippers were fabricated with polylactic acid (PLA) by 3D printing. The grippers were fixed to the bond tester Condor 100 XYZTEC for mechanical characterization of the samples. The mechanical design of the grippers ensured that their deformation was negligible in comparison to the PI films.

For the design, a typical PI film sample (5 mm wide and 5 µm thick) is assumed to be perfectly attached to the grippers (40 mm separation). The gripper geometry is simplified as a PLA block of 30 x 15 mm, with an unknown thickness t_{PLA} as presented in Fig. C.1.

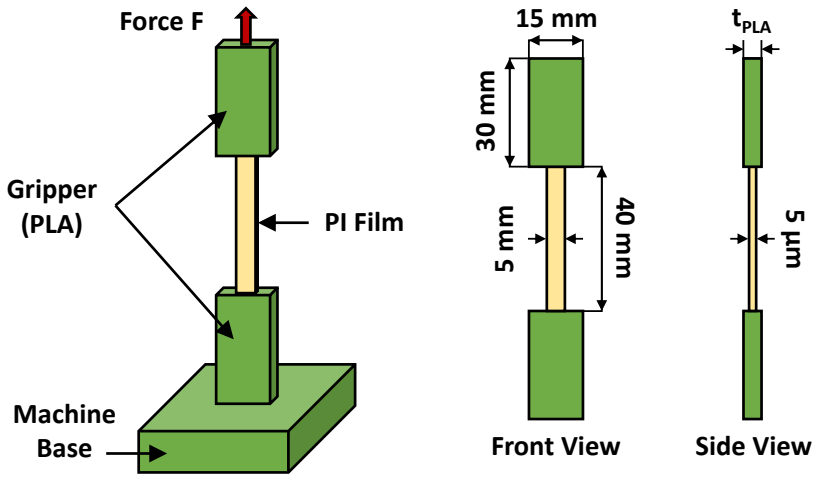

Fig. C.1 Schema for calculation of strains of the PLA grippers.

The tensile strength σ_{PI} = 526 MPa and elastic modulus E_{PI} = 9.8 GPa [21] provide a maximum film deformation ε_{PI} = 5.4 %, determined by:

$$\sigma_{PI} = \varepsilon_{PI} E_{PI}$$
$$\varepsilon_{PI} = \sigma_{PI} / E_{PI} \qquad \text{Eq. C.1}$$

By taking the cross-sectional area of the PI film as A_{PI} = 5 mm x 5 µm, the applied force can be obtained from the mechanical stress expression:

$$\sigma_{PI} = F / A_{PI}$$
$$F = \sigma_{PI} A_{PI} \qquad \text{Eq. C.2}$$

Since the gripper and the PI film are under the same tensile force, the Eq. C.1 and Eq. C.2 can be combined and rewritten to calculate the gripper strain:

$$\varepsilon_{PLA} = F / (A_{PLA} E_{PLA}) \qquad \text{Eq. C.3}$$

Eq. C.3 was used to compute the deformation of the gripper as a function of its thickness t_{PLA}. The gripper strain for three PI film strains (ε_{PI} = 1, 2.5 and 5.4 %) are presented in Fig. C.2a, and the corresponding deformation ΔL in µm is shown in Fig. C.2b. For the computation of the strain, an elastic modulus E_{PLA} = 2.6 GPa [123] was used for the gripper.

The deformation of the gripper decreased nonlinearly with the increase of its thickness. For example, by considering the maximum PI strain ε_{PI} = 5.4 % and the minimum gripper thickness by 3D printing (t_{PLA} = 0.1 mm), the gripper strain is ε_{PLA} = 0.34 % or ΔL = 100 µm. However, when the gripper thickness is t_{PLA} = 3 mm or more, its deformation drops below ε_{PLA} = 0.01 % (ΔL = 3.4 µm). Consequently, a minimum thickness of 3 mm is recommended for the gripper manufacture.

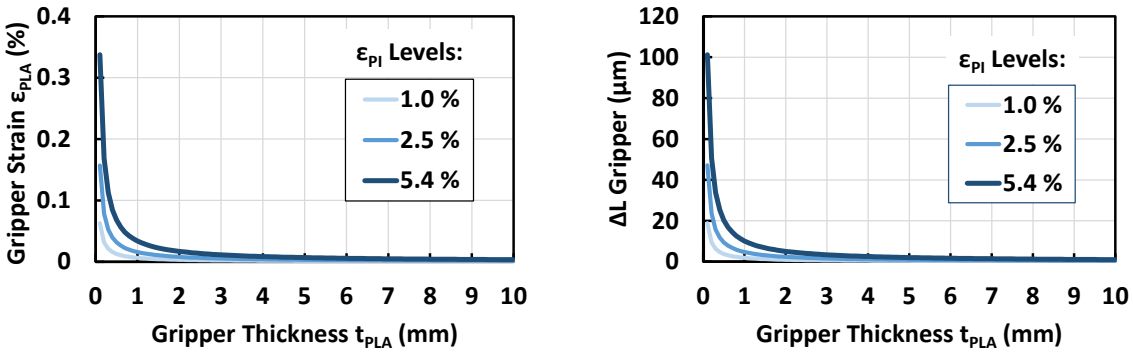

a) b)

Fig. C.2 Computed deformations of PLA grippers. a) Strain in percentage. b) Deformation in µm.

Different grippers were developed for the research, some included a housing for nuts for sample fixture. However, the designs had a minimum 3 mm thickness and were 3D printed as solid parts. Other fixtures were also fabricated to be used with copper plates for electrical contact with CNT/PI films or sensors during piezoresistive characterization.

A specific tool for pressure or compression tests was also produced to evaluate the piezoresistive properties of the CNT/PI films for the development of pressure sensors. This idea was further explored by my colleague Tim de Rijk [124–126], using also the tools developed in this work. Some tool designs are presented in Fig. C.3, in front and side views.

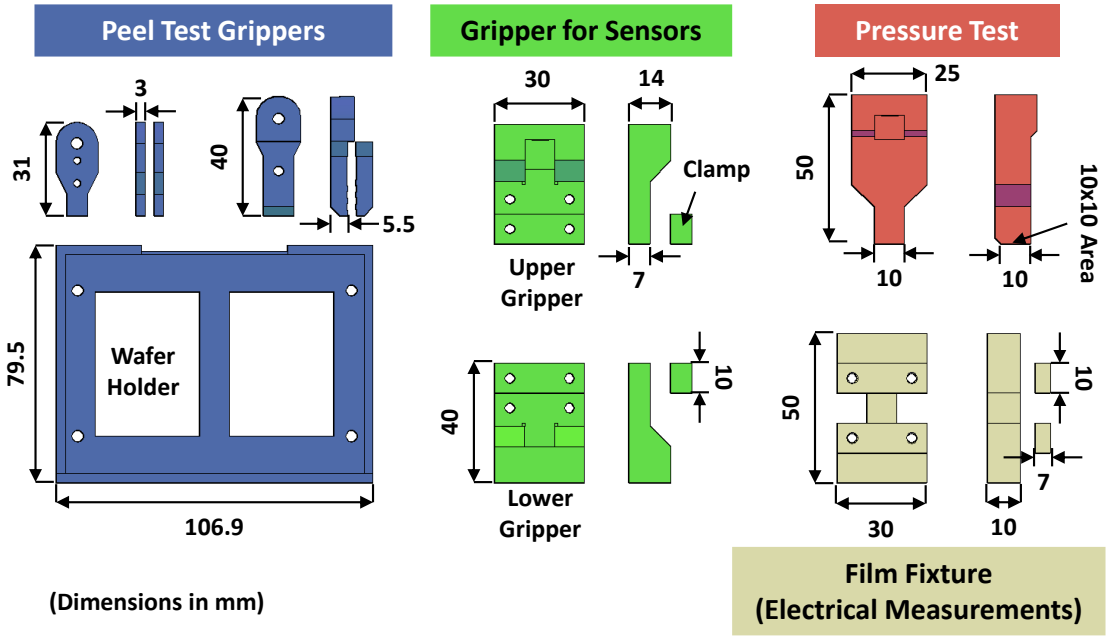

Fig. C.3. Gripper designs and other tools for 3D printing manufacturing.

C.2 Cutting Tool for PI Films

The preparation of PI and CNT/PI samples by photolithography was time-consuming, so a tool was proposed as an alternative to extract samples from PI and CNT/PI films. The tool was designed as an square of 10 by 10 cm with guiding lines for a scalpel knife (0.8 mm thick). The guides had separations of 10 mm or 5 mm, depending on the aimed sample width. The guides were 8.4 mm in length, which is enough for typical 7.5 cm length samples. The tool was 3D printed (with PLA material) with a thickness of at least 2.5 mm to provide mechanical stability during the handling of the blade. A tool design with a guide space of 1 cm is shown in Fig. C.4 (dimensions in mm).

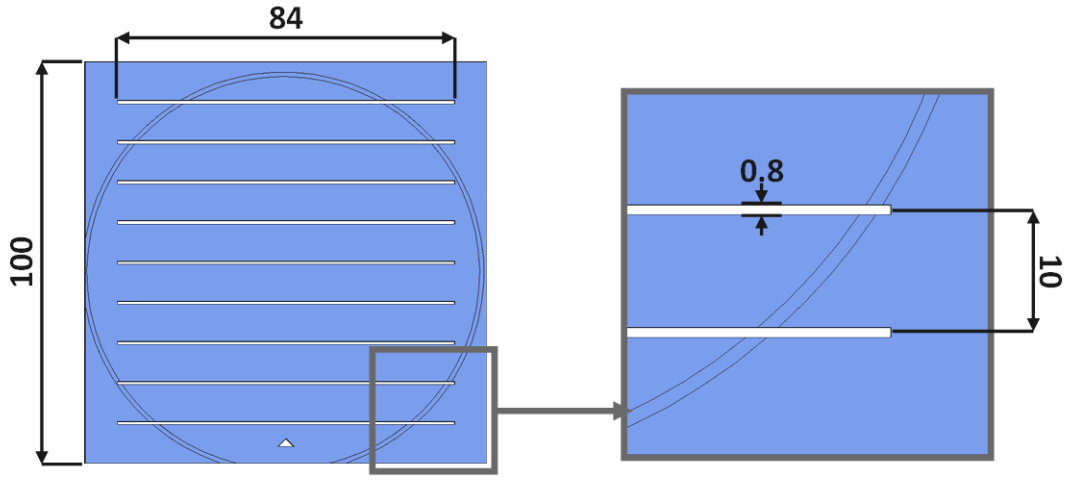

Fig. C.4 Design of a cutting tool for 1 cm wide PI film samples.

The proposed tool reduced significantly the time of sample preparation. The results of mechanical characterizations with specimens obtained by this method and by etching were similar.

Appendix D: Stirrer Design for CNT/PI Mixing

One challenging aspect of the work was the dispersion of CNTs for the PI films. After a promising manual mixing attempt, a stirrer was proposed considering three parameters:

- **Small size.** It should fit inside a commercial 25 ml glass beaker (28.5 mm inner diameter and 38 mm depth).
- **Chemical resistance.** The material used for the mixer should be resistant to the solvent of PI precursor (80 % NMP).
- **CNT dispersion.** The mixer should provide enough shear forces to break down CNT agglomerates.

Since commercial stirrers with such dimensions were not available [127–129], a 3D-printed part was proposed. The preliminary tests showed that parts fabricated from UV resin and PLA can stand the NMP long enough for the mixing. The blade design of the device was based on the stirrer classifications (Fig. D.1): axial, radial, and tangential flow [79,127].

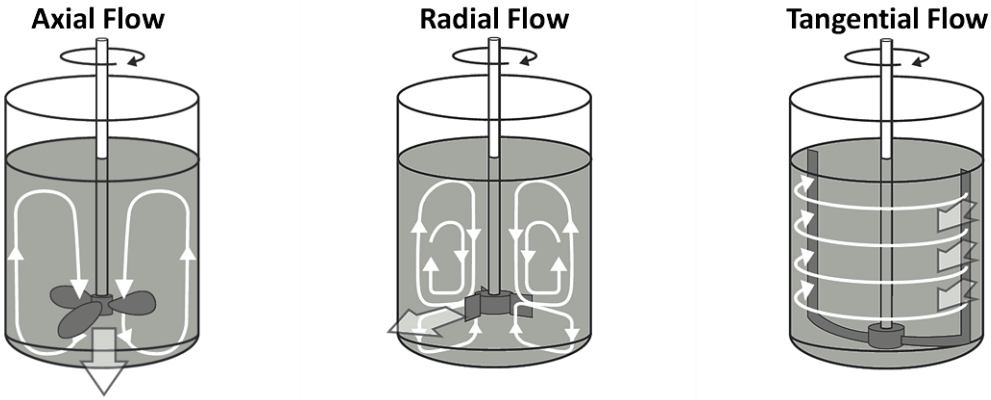

Fig. D.1 Examples of mixer blades classification by mixing flow [128].

The axial flow blades provide low shear forces and are suitable for liquids with a low viscosity. The radial flow mixers produce lower flows but higher shear forces, this is suitable for a medium viscosity material. For tangential flow mixers, the blades move the fluid with low shear forces, which is suitable for high viscosities.

The viscosity of the PI precursor ranges from 5 to 100 Pa·s, being a medium to highly viscous material. Additionally, since shear forces help breaking down the particle agglomerates [79], a promising design is a pitched blade mixer with a balance of axial and radial flow.

The proposed stirrer had a hexagonal shaft (75 mm length) and two blades (2 mm thick). The blade orientation was set at 45° to produce a top-to-bottom axial flow, avoiding the expelling of the CNTs. The number of blades and their orientation were set to be 3D printing friendly, avoiding the use of printing supports. The design is presented in Fig. D.2a, while the fabricated tool and its use during the mixing are shown in Fig. D.2b.

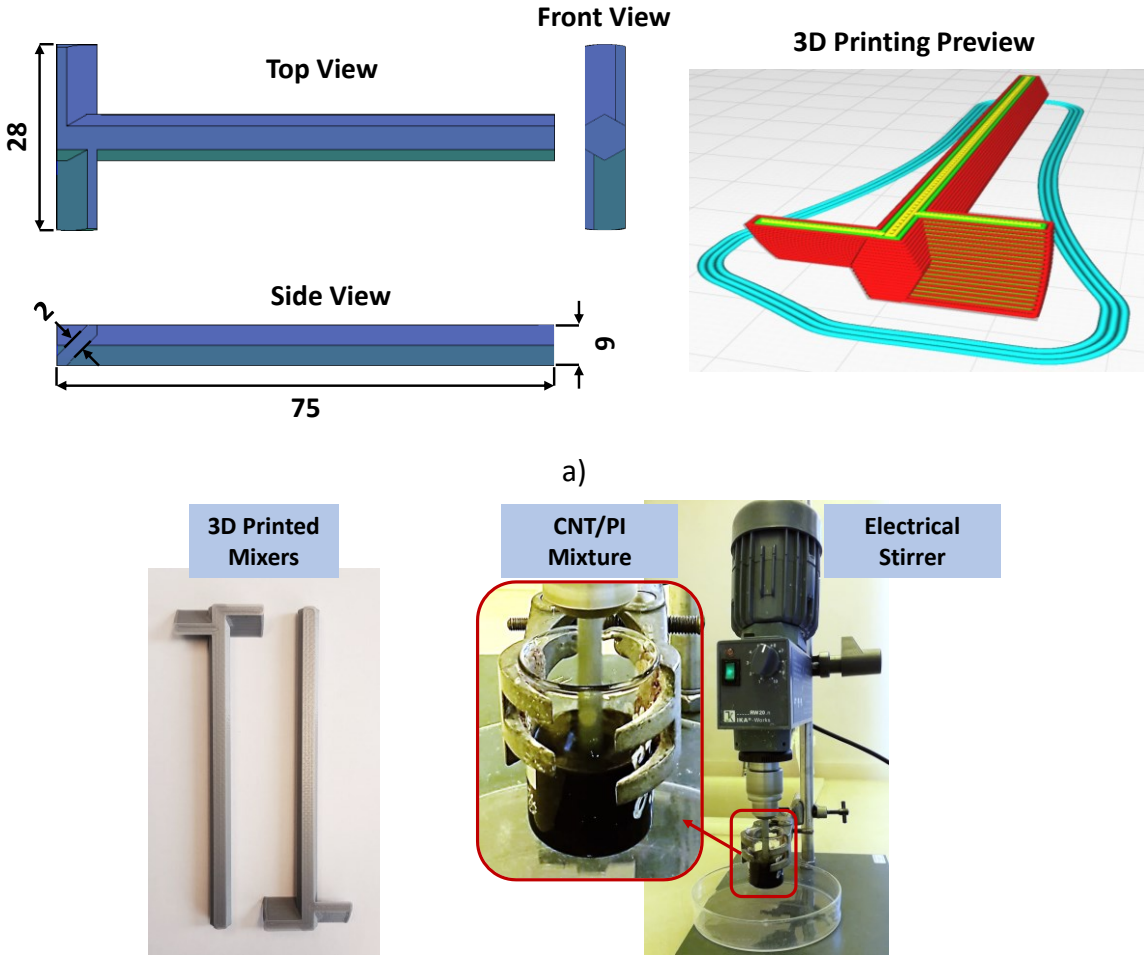

Fig. D.2 Mixer for CNT/PI. a) Design of the tool. b) Fabricated mixer and mixing test.

The developed mixer was used with an electric stirrer IKA RW 20n (IKA Works GmbH) to have control of the stirring RPM and the mixing time. During the mixing process, the blades were placed close to the beaker bottom to promote shear forces for dispersion of the CNTs.

References

[1] H. Janocha, ed., Adaptronics and smart structures: basics, materials, design, and applications ; with 17 tables, Second, revised edition, Springer, Berlin Heidelberg New York, 2007.

[2] A. D'Alessandro, H.B. Birgin, F. Ubertini, Advanced Monitoring of Structures and Infrastructures Through Smart Composite Sensors and Systems, in: C. Rainieri, G. Fabbrocino, N. Caterino, F. Ceroni, M.A. Notarangelo (Eds.), Civil Structural Health Monitoring, Springer International Publishing, Cham, 2021: pp. 485–498. https://doi.org/10.1007/978-3-030-74258-4_31.

[3] D. Balageas, C. Fritzen, A. Güemes, eds., Structural Health Monitoring, 1st ed., Wiley, 2006. https://doi.org/10.1002/9780470612071.

[4] Oak Ridge National Laboratory, Next-generation composites may monitor their own structural health, (2018). https://www.ornl.gov/news/self-sensing-materials-are-here.

[5] B. Han, S. Ding, X. Yu, Intrinsic self-sensing concrete and structures: A review, Measurement 59 (2015) 110–128. https://doi.org/10.1016/j.measurement.2014.09.048.

[6] G. Dumstorff, S. Paul, W. Lang, Integration Without Disruption: The Basic Challenge of Sensor Integration, IEEE Sensors J. 14 (2014) 2102–2111. https://doi.org/10.1109/JSEN.2013.2294626.

[7] M. Hübner, W. Lang, Online Monitoring of Composites with a Miniaturized Flexible Combined Dielectric and Temperature Sensor, in: Proceedings of Eurosensors 2017, Paris, France, 3–6 September 2017, MDPI, 2017: p. 627. https://doi.org/10.3390/proceedings1040627.

[8] D. Boll, K. Schubert, C. Brauner, W. Lang, Miniaturized Flexible Interdigital Sensor for In Situ Dielectric Cure Monitoring of Composite Materials, IEEE Sensors J. 14 (2014) 2193–2197. https://doi.org/10.1109/JSEN.2014.2309172.

[9] W. Lang, F. Jakobs, E. Tolstosheeva, H. Sturm, A. Ibragimov, A. Kesel, D. Lehmhus, U. Dicke, From embedded sensors to sensorial materials—The road to function scale integration, Sensors and Actuators A: Physical 171 (2011) 3–11. https://doi.org/10.1016/j.sna.2011.03.061.

[10] J. Fraden, Handbook of Modern Sensors, Springer New York, New York, NY, 2010. https://doi.org/10.1007/978-1-4419-6466-3.

[11] J.S. Wilson, Sensor technology handbook, Elsevier, Amsterdam, 2005.

[12] HBM, HBM Transducer Strain Gauges, (2023). www.hbm.com.

[13] K.K. Chawla, Composite Materials, Springer New York, New York, NY, 2012. https://doi.org/10.1007/978-0-387-74365-3.

[14] M.W. Hyer, Stress analysis of fiber-reinforced composite materials, Updated edition, DEStech Publications, Inc, Lancaster, Pennsylvania, 2009.

[15] J.M.P.Q. Delgado, ed., Industrial and Technological Applications of Transport in Porous Materials, Springer Berlin Heidelberg, Berlin, Heidelberg, 2013. https://doi.org/10.1007/978-3-642-37469-2.

[16] F.R. Jones, Composites Science, Technology, and Engineering, 1st ed., Cambridge University Press, 2022. https://doi.org/10.1017/9781139565943.

[17] G. Odian, Principles of polymerization, 4th ed, J. Wiley & sons, Hoboken (N.J.), 2004.

[18] M. Abadie, ed., High Performance Polymers - Polyimides Based - From Chemistry to Applications, InTech, 2012. https://doi.org/10.5772/2834.
[19] A. Schander, H. Stemmann, A. Kreiter, W. Lang, Silicon-Based Microfabrication of Free-Floating Neural Probes and Insertion Tool for Chronic Applications, Micromachines 9 (2018) 131. https://doi.org/10.3390/mi9030131.
[20] Hexcel Corporation, HexFlow RTM 6 -Technical datasheet., (2014).
[21] UBE Industries, Polyimide varnish UPIA - Technical datasheet, (2016).
[22] S. Iijima, Helical microtubules of graphitic carbon, Nature 354 (1991) 56–58. https://doi.org/10.1038/354056a0.
[23] M. Meyyappan, Carbon nanotubes: science and applications, CRC Press, Boca Raton, FL, 2005.
[24] M. Foldvari, M. Bagonluri, Carbon nanotubes as functional excipients for nanomedicines: I. pharmaceutical properties, Nanomedicine: Nanotechnology, Biology and Medicine 4 (2008) 173–182. https://doi.org/10.1016/j.nano.2008.04.002.
[25] A. Jorio, G. Dresselhaus, eds., Carbon nanotubes: advanced topics in the synthesis, structure, properties and applications, Springer, Berlin Heidelberg, 2008.
[26] M. Di Ventra, S. Evoy, J.R. Heflin, Introduction to nanoscale science and technology, Kluwer Academic Publishers, Boston, 2004.
[27] A. Nag, J. Kosel, S.C. Mukhopadhyay, Printed Flexible Sensors: Fabrication, Characterization and Implementation, 1st ed. 2019, Springer International Publishing : Imprint: Springer, Cham, 2019. https://doi.org/10.1007/978-3-030-13765-6.
[28] P.M. Ajayan, L.S. Schadler, P.V. Braun, Nanocomposite science and technology, Wiley-VCH, Weinheim, 2003.
[29] W. Bauhofer, J.Z. Kovacs, A review and analysis of electrical percolation in carbon nanotube polymer composites, Composites Science and Technology 69 (2009) 1486–1498. https://doi.org/10.1016/j.compscitech.2008.06.018.
[30] N.G. Sahoo, S. Rana, J.W. Cho, L. Li, S.H. Chan, Polymer nanocomposites based on functionalized carbon nanotubes, Progress in Polymer Science 35 (2010) 837–867. https://doi.org/10.1016/j.progpolymsci.2010.03.002.
[31] M.R. Watt, R.A. Gerhardt, Factors that Affect Network Formation in Carbon Nanotube Composites and their Resultant Electrical Properties, J. Compos. Sci. 4 (2020) 100. https://doi.org/10.3390/jcs4030100.
[32] F. Avilés, A.I. Oliva-Avilés, M. Cen-Puc, Piezoresistivity, Strain, and Damage Self-Sensing of Polymer Composites Filled with Carbon Nanostructures, Adv Eng Mater 20 (2018) 1701159. https://doi.org/10.1002/adem.201701159.
[33] Y.-T. Huang, S.-C. Huang, C.-C. Hsu, R.-M. Chao, T.K. Vu, Design and Fabrication of Single-Walled Carbon Nanonet Flexible Strain Sensors, Sensors 12 (2012) 3269–3280. https://doi.org/10.3390/s120303269.
[34] D. Lee, H.P. Hong, M.J. Lee, C.W. Park, N.K. Min, A prototype high sensitivity load cell using single walled carbon nanotube strain gauges, Sensors and Actuators A: Physical 180 (2012) 120–126. https://doi.org/10.1016/j.sna.2012.04.015.
[35] G. Arana, F. Gamboa, F. Avilés, Piezoresistive and thermoresistive responses of carbon nanotube-based strain gauges with different grid geometric parameters, Sensors and Actuators A: Physical 359 (2023) 114477. https://doi.org/10.1016/j.sna.2023.114477.
[36] J. Jehn, P. Oser, M.A.M. Courrau, M. Kaiser, D. Wu, C.U. Grosse, U. Moosheimer, A. Ruediger, C. Schindler, Fully Inkjet-Printed Carbon Nanotube-PDMS-Based Strain Sensor: Temperature Response, Compressive and Tensile Bending Properties, and Fatigue

Investigations, IEEE Access 9 (2021) 72207–72216. https://doi.org/10.1109/ACCESS.2021.3078799.
[37] X. Peng, X. Zhang, R. Wang, Y. Chen, X. Chu, L. Kong, X. Yan, M. Kuang, Printing of Carbon Nanotube-Based Temperature and Bending Sensors for High-Temperature-Resistant Intelligent Textiles, ACS Appl. Electron. Mater. 4 (2022) 1949–1957. https://doi.org/10.1021/acsaelm.2c00133.
[38] N. Li, G. Huang, Y. Liu, C. Qu, M. Li, H. Xiao, Performance Deficiency Improvement of CNT-Based Strain Sensors by Magnetic-Induced Patterning, ACS Appl. Mater. Interfaces 15 (2023) 5774–5786. https://doi.org/10.1021/acsami.2c18036.
[39] M.-Y. Hwang, D.-H. Han, L.-H. Kang, Piezoresistive Multi-Walled Carbon Nanotube/Epoxy Strain Sensor with Pattern Design, Materials 12 (2019) 3962. https://doi.org/10.3390/ma12233962.
[40] P.-Y. Wu, C.-H. Lin, C.-M. Chen, Study of Surface Metallization of Polyimide Film and Interfacial Characterization, Metals 7 (2017) 189. https://doi.org/10.3390/met7060189.
[41] W.-X. Yu, L. Hong, B.-H. Chen, T.-M. Ko, A study on the interfacial composition of the electroless-copper-plated BPDA-PDA polyimide sheet, J. Mater. Chem. 13 (2003) 818–824. https://doi.org/10.1039/b208102d.
[42] Y.J. Park, D.M. Yu, J.H. Ahn, J.-H. Choi, Y.T. Hong, Surface modification of polyimide films by an ethylenediamine treatment for a flexible copper clad laminate, Macromol. Res. 20 (2012) 168–173. https://doi.org/10.1007/s13233-012-0025-2.
[43] F. Lin, W. Li, Y. Tang, H. Shao, C. Su, J. Jiang, N. Chen, High-Performance Polyimide Filaments and Composites Improved by O2 Plasma Treatment, Polymers 10 (2018) 695. https://doi.org/10.3390/polym10070695.
[44] X. Sun, J. Bu, W. Liu, H. Niu, S. Qi, G. Tian, D. Wu, Surface modification of polyimide fibers by oxygen plasma treatment and interfacial adhesion behavior of a polyimide fiber/epoxy composite, Science and Engineering of Composite Materials 24 (2017) 477–484. https://doi.org/10.1515/secm-2015-0092.
[45] Y. Wen, X. Meng, J. Liu, J. Yan, Z. Wang, Surface modification of high-performance polyimide fibers by oxygen plasma treatment, High Performance Polymers 29 (2017) 1083–1089. https://doi.org/10.1177/0954008316669570.
[46] S.H. Kim, S.W. Na, N.-E. Lee, Y.W. Nam, Y.-H. Kim, Effect of surface roughness on the adhesion properties of Cu/Cr films on polyimide substrate treated by inductively coupled oxygen plasma, Surface and Coatings Technology 200 (2005) 2072–2079. https://doi.org/10.1016/j.surfcoat.2005.05.021.
[47] W. Albrecht, J. Schauer, Th. Weigel, A. Lendlein, Preparation of novel composite membranes: Reactive coating on microporous poly(ether imide) support membranes, Journal of Membrane Science 269 (2006) 49–59. https://doi.org/10.1016/j.memsci.2005.06.015.
[48] H. Qu, Z. Wang, D. Cang, Flexible Bandpass Filter Fabricated on Polyimide Substrate by Surface Modification and In Situ Self-Metallization Technique, Polymers 11 (2019) 2068. https://doi.org/10.3390/polym11122068.
[49] K.W. Lee, S.P. Kowalczyk, J.M. Shaw, Surface modification of BPDA-PDA polyimide, Langmuir 7 (1991) 2450–2453. https://doi.org/10.1021/la00059a009.
[50] W. Yu, T.-M. Ko, Surface characterizations of potassium-hydroxide-modified Upilex-S® polyimide at an elevated temperature, European Polymer Journal 37 (2001) 1791–1799. https://doi.org/10.1016/S0014-3057(01)00060-X.

[51] D.K. Owens, R.C. Wendt, Estimation of the surface free energy of polymers, J of Applied Polymer Sci 13 (1969) 1741–1747. https://doi.org/10.1002/app.1969.070130815.
[52] S.-J. Park, H.-Y. Lee, Effect of atmospheric-pressure plasma on adhesion characteristics of polyimide film, Journal of Colloid and Interface Science 285 (2005) 267–272. https://doi.org/10.1016/j.jcis.2004.11.062.
[53] Z. Zhang, W. Wang, A.N. Korpacz, C.R. Dufour, Z.J. Weiland, C.R. Lambert, M.T. Timko, Binary Liquid Mixture Contact-Angle Measurements for Precise Estimation of Surface Free Energy, Langmuir 35 (2019) 12317–12325. https://doi.org/10.1021/acs.langmuir.9b01252.
[54] C. Yarce, D. Pineda, C. Correa, C. Salamanca, Relationship between Surface Properties and In Vitro Drug Release from a Compressed Matrix Containing an Amphiphilic Polymer Material, Pharmaceuticals 9 (2016) 34. https://doi.org/10.3390/ph9030034.
[55] H. Brown, A. Yang, T. Russell, W. Volksen, E. Kramer, Diffusion and self-adhesion of the polyimide PMDA-ODA, Polymer 29 (1988) 1807–1811. https://doi.org/10.1016/0032-3861(88)90395-3.
[56] M. Ree, Y.H. Park, T.J. Shin, T.L. Nunes, W. Volksen, Self-adhesion of poly(4,4'-oxydiphenylene biphenyltetracarboximide) and its adhesion to substrates, Polymer 41 (2000) 2105–2111. https://doi.org/10.1016/S0032-3861(99)00385-7.
[57] Sigma-Aldrich, Carbon nanotube multi-walled, (2023). https://www.sigmaaldrich.com/DE/en/product/aldrich/901019.
[58] T.W. Ebbesen, H.J. Lezec, H. Hiura, J.W. Bennett, H.F. Ghaemi, T. Thio, Electrical conductivity of individual carbon nanotubes, Nature 382 (1996) 54–56. https://doi.org/10.1038/382054a0.
[59] V.N. Gaitonde, S.R. Karnik, M.S. Jayaprakash, Some Studies on Wear and Corrosion Properties of Al5083/Al₂O₃/Graphite Hybrid Composites, JMMCE 11 (2012) 695–703. https://doi.org/10.4236/jmmce.2012.117055.
[60] N. Hu, Y. Karube, C. Yan, Z. Masuda, H. Fukunaga, Tunneling effect in a polymer/carbon nanotube nanocomposite strain sensor, Acta Materialia 56 (2008) 2929–2936. https://doi.org/10.1016/j.actamat.2008.02.030.
[61] N. Hu, Y. Karube, M. Arai, T. Watanabe, C. Yan, Y. Li, Y. Liu, H. Fukunaga, Investigation on sensitivity of a polymer/carbon nanotube composite strain sensor, Carbon 48 (2010) 680–687. https://doi.org/10.1016/j.carbon.2009.10.012.
[62] X. Zeng, X. Xu, P.M. Shenai, E. Kovalev, C. Baudot, N. Mathews, Y. Zhao, Characteristics of the Electrical Percolation in Carbon Nanotubes/Polymer Nanocomposites, J. Phys. Chem. C 115 (2011) 21685–21690. https://doi.org/10.1021/jp207388n.
[63] Alamusi, N. Hu, H. Fukunaga, S. Atobe, Y. Liu, J. Li, Piezoresistive Strain Sensors Made from Carbon Nanotubes Based Polymer Nanocomposites, Sensors 11 (2011) 10691–10723. https://doi.org/10.3390/s111110691.
[64] X. Ni, C. Hui, N. Su, W. Jiang, F. Liu, Monte Carlo simulations of electrical percolation in multicomponent thin films with nanofillers, Nanotechnology 29 (2018) 075401. https://doi.org/10.1088/1361-6528/aaa0be.
[65] H. Tanabi, M. Erdal, Effect of CNTs dispersion on electrical, mechanical and strain sensing properties of CNT/epoxy nanocomposites, Results in Physics 12 (2019) 486–503. https://doi.org/10.1016/j.rinp.2018.11.081.
[66] R. Ram, M. Rahaman, A. Aldalbahi, D. Khastgir, Determination of percolation threshold and electrical conductivity of polyvinylidene fluoride (PVDF)/short carbon fiber (SCF)

composites: effect of SCF aspect ratio, Polymer International 66 (2017) 573–582. https://doi.org/10.1002/pi.5294.
[67] D. Stauffer, A. Aharony, Introduction To Percolation Theory, 0 ed., Taylor & Francis, 2018. https://doi.org/10.1201/9781315274386.
[68] M. Sahimi, Applications of percolation theory, Second edition, Springer Nature, Cham, Switzerland, 2023. https://doi.org/10.1007/978-3-031-20386-2.
[69] R.D. Chippendale, I.O. Golosnoy, Percolation effects in electrical conductivity of carbon fibre composites, in: IET 8th International Conference on Computation in Electromagnetics (CEM 2011), IET, Wroclaw, Poland, 2011: pp. 186–187. https://doi.org/10.1049/cp.2011.0094.
[70] J. Huang, Carbon black filled conducting polymers and polymer blends, Adv Polym Technol 21 (2002) 299–313. https://doi.org/10.1002/adv.10025.
[71] R. Rothon, ed., Fillers for Polymer Applications, Springer International Publishing, Cham, 2017. https://doi.org/10.1007/978-3-319-28117-9.
[72] J. Nagel, T. Hanemann, B.E. Rapp, G. Finnah, Enhanced PTC Effect in Polyamide/Carbon Black Composites, Materials 15 (2022) 5400. https://doi.org/10.3390/ma15155400.
[73] O. Breuer, U. Sundararaj, Big returns from small fibers: A review of polymer/carbon nanotube composites, Polymer Composites 25 (2004) 630–645. https://doi.org/10.1002/pc.20058.
[74] B. Fiedler, F.H. Gojny, M.H.G. Wichmann, M.C.M. Nolte, K. Schulte, Fundamental aspects of nano-reinforced composites, Composites Science and Technology 66 (2006) 3115–3125. https://doi.org/10.1016/j.compscitech.2005.01.014.
[75] P.-C. Ma, N.A. Siddiqui, G. Marom, J.-K. Kim, Dispersion and functionalization of carbon nanotubes for polymer-based nanocomposites: A review, Composites Part A: Applied Science and Manufacturing 41 (2010) 1345–1367. https://doi.org/10.1016/j.compositesa.2010.07.003.
[76] F. Khan, A. Kausar, M. Siddiq, A Review on Properties and Fabrication Techniques of Polymer/Carbon Nanotube Composites and Polymer Intercalated Buckypapers, Polymer-Plastics Technology and Engineering 54 (2015) 1524–1539. https://doi.org/10.1080/03602559.2015.1021486.
[77] Sigma-Aldrich, Solvent Miscibility Chart, (2023).
[78] Phenomenex Inc., Phenomenex Product Guide 2023, (2023).
[79] E.L. Paul, V.A. Atiemo-Obeng, S.M. Kresta, eds., Handbook of Industrial Mixing: Science and Practice, 1st ed., Wiley, 2003. https://doi.org/10.1002/0471451452.
[80] American Institute of Chemical Engineers, ed., Mixing equipment: impeller type, 3. ed, AIChE, New York, NY, 2001.
[81] Sigma-Aldrich, Graphene nanoplatelets, (2023). https://www.sigmaaldrich.com/DE/en/product/aldrich/900394.
[82] Y.-B. Yi, A.M. Sastry, Analytical approximation of the percolation threshold for overlapping ellipsoids of revolution, Proc. R. Soc. Lond. A 460 (2004) 2353–2380. https://doi.org/10.1098/rspa.2004.1279.
[83] Y. Chen, F. Pan, S. Wang, B. Liu, J. Zhang, Theoretical estimation on the percolation threshold for polymer matrix composites with hybrid fillers, Composite Structures 124 (2015) 292–299. https://doi.org/10.1016/j.compstruct.2015.01.013.
[84] S. Kirkpatrick, Percolation and Conduction, Rev. Mod. Phys. 45 (1973) 574–588. https://doi.org/10.1103/RevModPhys.45.574.

[85] D. Thuau, V. Koutsos, R. Cheung, Electrical and mechanical properties of carbon nanotube-polyimide composites, Journal of Vacuum Science & Technology B: Microelectronics and Nanometer Structures Processing, Measurement, and Phenomena 27 (2009) 3139–3144. https://doi.org/10.1116/1.3250192.
[86] J.J. Ku-Herrera, F. Avilés, Cyclic tension and compression piezoresistivity of carbon nanotube/vinyl ester composites in the elastic and plastic regimes, Carbon 50 (2012) 2592–2598. https://doi.org/10.1016/j.carbon.2012.02.018.
[87] R. Zhang, H. Deng, R. Valenca, J. Jin, Q. Fu, E. Bilotti, T. Peijs, Strain sensing behaviour of elastomeric composite films containing carbon nanotubes under cyclic loading, Composites Science and Technology 74 (2013) 1–5. https://doi.org/10.1016/j.compscitech.2012.09.016.
[88] L. Lin, S. Liu, Q. Zhang, X. Li, M. Ji, H. Deng, Q. Fu, Towards Tunable Sensitivity of Electrical Property to Strain for Conductive Polymer Composites Based on Thermoplastic Elastomer, ACS Appl. Mater. Interfaces 5 (2013) 5815–5824. https://doi.org/10.1021/am401402x.
[89] L. Duan, S. Fu, H. Deng, Q. Zhang, K. Wang, F. Chen, Q. Fu, The resistivity–strain behavior of conductive polymer composites: stability and sensitivity, J. Mater. Chem. A 2 (2014) 17085–17098. https://doi.org/10.1039/C4TA03645J.
[90] D.D.L. Chung, Carbon composites: composites with carbon fibers, nanofibers, and nanotubes, Second edition, Elsevier/BH, Butterworth-Heinemann is an imprint of Elsevier, Amsterdam Boston, 2017.
[91] D.R. Askeland, The Science and Engineering of Materials, Springer US, Boston, MA, 1996. https://doi.org/10.1007/978-1-4899-2895-5.
[92] D.I. Bower, An Introduction to Polymer Physics, 1st ed., Cambridge University Press, 2002. https://doi.org/10.1017/CBO9780511801280.
[93] L.H. Sperling, Introduction to Physical Polymer Science, 1st ed., Wiley, 2005. https://doi.org/10.1002/0471757128.
[94] J.C. Gerdeen, R.A.L. Rorrer, Engineering design with polymers and composites, 2. ed, CRC Press, Boca Raton, Fla., 2012.
[95] J. Amraei, A. Katunin, Recent Advances in Limiting Fatigue Damage Accumulation Induced by Self-Heating in Polymer–Matrix Composites, Polymers 14 (2022) 5384. https://doi.org/10.3390/polym14245384.
[96] D20 Committee, Test Method for Tensile Properties of Thin Plastic Sheeting, (n.d.). https://doi.org/10.1520/D0882-02.
[97] Faserverbundwerkstoffe, Composite Technology, Technical Data: UNIPREG Carbon non-crimp fabric 150, (2021). http://www.ezentrumbilder.de/rg/pdf/td_en_192150050-UUD-PP_2.pdf.
[98] A. Behnam, Y. Choi, L. Noriega, Z. Wu, I. Kravchenko, A.G. Rinzler, A. Ural, Nanolithographic patterning of transparent, conductive single-walled carbon nanotube films by inductively coupled plasma reactive ion etching, Journal of Vacuum Science & Technology B: Microelectronics and Nanometer Structures Processing, Measurement, and Phenomena 25 (2007) 348–354. https://doi.org/10.1116/1.2699836.
[99] J. Lee, A. Efremov, J. Lee, K. Kim, K.-H. Kwon, Etching Characteristics of Carbon Nanotube Thin Films in O2/Ar Plasma, J Nanosci Nanotechnol 16 (2016) 12021–12027. https://doi.org/10.1166/jnn.2016.13637.
[100] M. Kahali Moghaddam, A. Breede, A. Chaloupka, A. Bödecker, C. Habben, E.-M. Meyer, C. Brauner, W. Lang, Design, fabrication and embedding of microscale interdigital

sensors for real-time cure monitoring during composite manufacturing, Sensors and Actuators A: Physical 243 (2016) 123–133. https://doi.org/10.1016/j.sna.2016.03.017.

[101] D30 Committee, Test Method for Tensile Properties of Polymer Matrix Composite Materials, (n.d.). https://doi.org/10.1520/D3039_D3039M-08.

[102] J.G. Noel, Review of the properties of gold material for MEMS membrane applications, IET Circuits, Devices & Systems 10 (2016) 156–161. https://doi.org/10.1049/iet-cds.2015.0094.

[103] S. Luo, Y. Wang, G. Wang, K. Wang, Z. Wang, C. Zhang, B. Wang, Y. Luo, L. Li, T. Liu, CNT Enabled Co-braided Smart Fabrics: A New Route for Non-invasive, Highly Sensitive & Large-area Monitoring of Composites, Sci Rep 7 (2017) 44056. https://doi.org/10.1038/srep44056.

[104] L. Tzounis, M. Liebscher, A. Tzounis, E. Petinakis, A.S. Paipetis, E. Mäder, M. Stamm, CNT-grafted glass fibers as a smart tool for epoxy cure monitoring, UV-sensing and thermal energy harvesting in model composites, RSC Adv. 6 (2016) 55514–55525. https://doi.org/10.1039/C6RA09800B.

[105] O. Rodríguez-Uicab, J.L. Abot, F. Avilés, Electrical Resistance Sensing of Epoxy Curing Using an Embedded Carbon Nanotube Yarn, Sensors 20 (2020) 3230. https://doi.org/10.3390/s20113230.

[106] D. Gräbner, Materialintegrierte Messung von mechanischen Größen: Sensoren und Anwendungen, PhD Thesis, Universität Bremen, 2021. https://doi.org/10.26092/ELIB/768.

[107] A. Schander, Mikroelektroden für die chronische Ableitung und Stimulation neuronaler Aktivität im Kortex, PhD Thesis, Universität Bremen, 2018.

[108] M.R. Kincer, C.E. Meree, E.K. Goss, E.A. Mintz, M.L. Shofner, Thermomechanical properties of nanotubes in a thermosetting polyimide matrix: Relationship to the percolation threshold, Composites Part A: Applied Science and Manufacturing 61 (2014) 60–66. https://doi.org/10.1016/j.compositesa.2014.02.009.

[109] Z. Ounaies, Electrical properties of single wall carbon nanotube reinforced polyimide composites, Composites Science and Technology 63 (2003) 1637–1646. https://doi.org/10.1016/S0266-3538(03)00067-8.

[110] G. Wu, Y. Tang, R. Weng, Dispersion of nano-carbon filled polyimide composites using self-degradated low molecular poly(amic acid) as impurity-free dispersant, Polymer Degradation and Stability 95 (2010) 1449–1455. https://doi.org/10.1016/j.polymdegradstab.2010.06.026.

[111] H.H. So, J.W. Cho, N.G. Sahoo, Effect of carbon nanotubes on mechanical and electrical properties of polyimide/carbon nanotubes nanocomposites, European Polymer Journal 43 (2007) 3750–3756. https://doi.org/10.1016/j.eurpolymj.2007.06.025.

[112] X. Jiang, Y. Bin, M. Matsuo, Electrical and mechanical properties of polyimide–carbon nanotubes composites fabricated by in situ polymerization, Polymer 46 (2005) 7418–7424. https://doi.org/10.1016/j.polymer.2005.05.127.

[113] A. Yu, H. Hu, E. Bekyarova, M.E. Itkis, J. Gao, B. Zhao, R.C. Haddon, Incorporation of highly dispersed single-walled carbon nanotubes in a polyimide matrix, Composites Science and Technology 66 (2006) 1190–1197. https://doi.org/10.1016/j.compscitech.2005.10.023.

[114] B. Zhu, S. Xie, Z. Xu, Y. Xu, Preparation and properties of the polyimide/multi-walled carbon nanotubes (MWNTs) nanocomposites, Composites Science and Technology 66 (2006) 548–554. https://doi.org/10.1016/j.compscitech.2005.05.038.

[115] Y. Wang, A.X. Wang, Y. Wang, M.K. Chyu, Q.-M. Wang, Fabrication and characterization of carbon nanotube–polyimide composite based high temperature flexible thin film piezoresistive strain sensor, Sensors and Actuators A: Physical 199 (2013) 265–271. https://doi.org/10.1016/j.sna.2013.05.023.
[116] S. Deshmukh, Z. Ounaies, Single walled carbon nanotube (SWNT)–polyimide nanocomposites as electrostrictive materials, Sensors and Actuators A: Physical 155 (2009) 246–252. https://doi.org/10.1016/j.sna.2009.07.007.
[117] C.R. Misiego, R.B. Pipes, Dispersion and its relation to carbon nanotube concentration in polyimide nanocomposites, Composites Science and Technology 85 (2013) 43–49. https://doi.org/10.1016/j.compscitech.2013.05.011.
[118] M.R. Schlea, C.E. Meree, R.A. Gerhardt, E.A. Mintz, M.L. Shofner, Network behavior of thermosetting polyimide/multiwalled carbon nanotube composites, Polymer 53 (2012) 1020–1027. https://doi.org/10.1016/j.polymer.2011.12.050.
[119] W. Chou, C. Wang, C. Chen, Characteristics of polyimide-based nanocomposites containing plasma-modified multi-walled carbon nanotubes, Composites Science and Technology 68 (2008) 2208–2213. https://doi.org/10.1016/j.compscitech.2008.04.008.
[120] Q.-Y. Tang, Y.C. Chan, K. Zhang, Fast response resistive humidity sensitivity of polyimide/multiwall carbon nanotube composite films, Sensors and Actuators B: Chemical 152 (2011) 99–106. https://doi.org/10.1016/j.snb.2010.09.016.
[121] K.-P. Yoo, L.-T. Lim, N.-K. Min, M.J. Lee, C.J. Lee, C.-W. Park, Novel resistive-type humidity sensor based on multiwall carbon nanotube/polyimide composite films, Sensors and Actuators B: Chemical 145 (2010) 120–125. https://doi.org/10.1016/j.snb.2009.11.041.
[122] C. Gau, H.S. Ko, H.T. Chen, Piezoresistive characteristics of MWNT nanocomposites and fabrication as a polymer pressure sensor, Nanotechnology 20 (2009) 185503. https://doi.org/10.1088/0957-4484/20/18/185503.
[123] Polymaker, Technical Data Sheet: Polylite PLA, (2023). www.polymaker.com.
[124] T. De Rijk, M. Cen-Puc, J.K. Piening, W. Lang, Single layer piezoresistive polyimide pressure sensor based on carbon nanotubes, in: 2022 IEEE Sensors, IEEE, Dallas, TX, USA, 2022: pp. 1–4. https://doi.org/10.1109/SENSORS52175.2022.9967230.
[125] T.M. De Rijk, Unidirectional sensing via dual-sensitivity bi-axial flexible sensors. Based on electrically aligned carbon nanotube nanocomposites, [object Object], 2024. https://doi.org/10.26092/ELIB/2741.
[126] T.M. De Rijk, M. Cen-Puc, Y. Mirzaei, P. Schneider, U. Giese, W. Lang, Integrated Flexible Polyimide Sensor for Monitoring Compressive Force in Sealings, IEEE Sensors J. 24 (2024) 12153–12160. https://doi.org/10.1109/JSEN.2024.3371090.
[127] Caframo Lab Solutions, Stirrer Guide, (2018).
[128] IKA-Werke GmbH & CO. KG, Overview: Geometry of Stirring Tools, (2021). https://www.ika.com/ika/pdf/flyer-catalog/20210324_Flyer_Stirrers_Technical%20Overview_6%20pages_IWS_EN_web.pdf.
[129] Collomix, Mixing paddles, (2019). https://www.collomix.com/03%20Dokumente-Variants/Datenbl%C3%A4tter%20%26%20Flyer-Produktbrosch%C3%BCre/02%20R%C3%BChrer/DB_%20SammelprospektR%C3%BChrer_EN_45004-011_ebook.pdf.

Miscellaneous Pictures

Several pictures of the project were not included in the explanations of the chapters, some of them are presented in this miscellaneous section. The first picture shows some silicon wafers (10 cm diameter) used for the fabrication of the CNT/PI films. The order of the wafers from left to right shows the improvement in the fabrication process of the films.

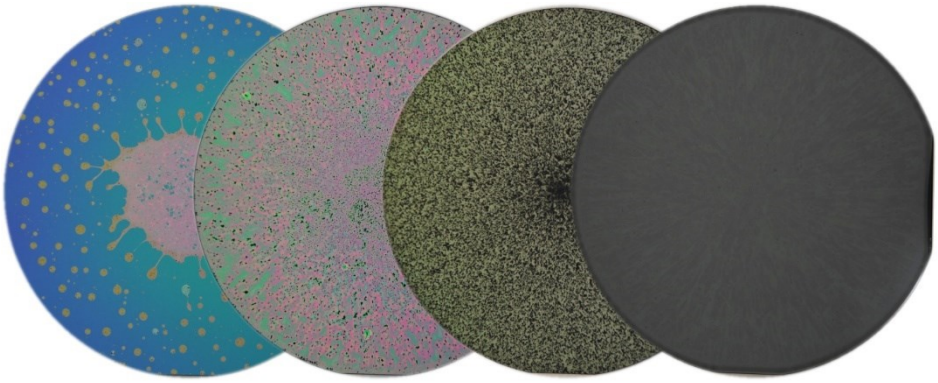

Picture 1 Improvement of the fabrication process for CNT/PI films.

The following picture compares two aligning structures produced on films. The picture on the left is one of the first structures produced by the author, which was a gold layer on a pristine polymer film. The right picture belongs to an aligning structure produced on a CNT/PI film and shows that the use of CNT/PI mixture increased the roughness of the material.

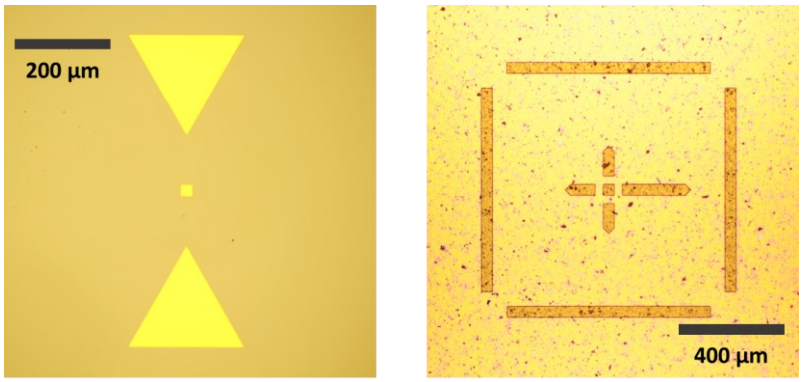

Picture 2 Aligning structures produced on different films.

The following image on the left shows one of the first structuring tests of the CNT/PI film, etched by RIE to produce rectangular samples for mechanical characterizations. The wafer on the right side corresponds to the first version of the meander-structured sensors, which had gold connections for electrical measurements.

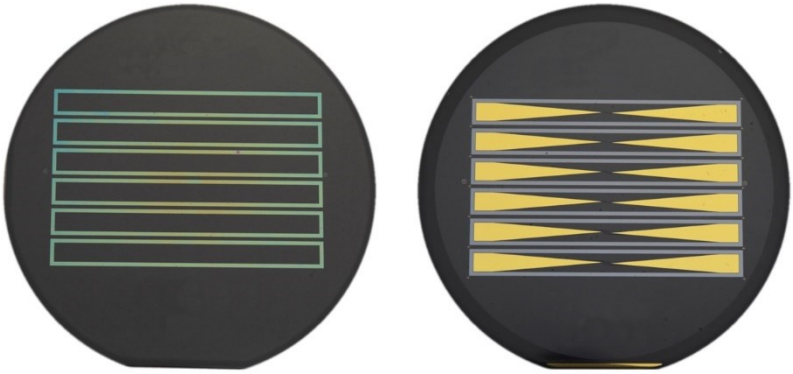

Picture 3 Structured CNT/PI films and first sensor design.

Some of the last sensors produced from CNT/PI films are shown below. The sensors had a top coating for electrical insulation, and the gold layer was used only for the connection pads.

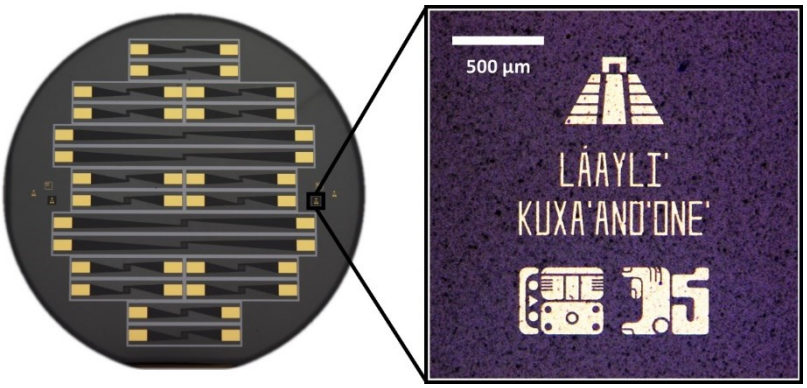

Picture 4 Last version of the CNT/PI strain sensors.

At the time of fabricating these samples, Mexico was celebrating the day of native languages, and the author included some gold orientation marks related to his cultural heritage. The top figure represents a step pyramid, and the text below it is written in Yucatecan Mayan using its modern alphabet: *Láayli' kuxa'ano'one'* (We are still alive). At the bottom, a text is written using the ancient hieroglyphic system: *U ts'íib Ken* (the writing of Ken) as the author's signature. This is probably the first (short) hieroglyphic text written by the Mayan people using microtechnology.

List of Publications and Conferences

1. **M. Cen**, W. Lang, Surface Functionalization of Polyimide Substrates for Microsensors' Applications, LogDynamics Research Report 6 (2019) 25–26.
2. M. Veigt, **M. Cen**, E. Hardi, W. Lang, M. Freitag, Using RFID to Monitor the Curing of Aramid Fiber Reinforced Polymers, in: M. Freitag, H.-D. Haasis, H. Kotzab, J. Pannek (Eds.), Dynamics in Logistics, Springer International Publishing, Cham, 2020: pp. 441–450. https://doi.org/10.1007/978-3-030-44783-0_42.
3. **M. Cen-Puc**, A. Schander, M.G. Vargas Gleason, W. Lang, An Assessment of Surface Treatments for Adhesion of Polyimide Thin Films, Polymers 13 (2021) 1955. https://doi.org/10.3390/polym13121955.
4. **M. Cen-Puc**, T. De Rijk, M.V. Gleason, W. Lang, Carbon Nanotubes/Polymer Films for Microsensors Applications, in: 2021 IEEE Sensors, IEEE, Sydney, Australia, 2021: pp. 1–4. https://doi.org/10.1109/SENSORS47087.2021.9639761.
5. **M. Cen-Puc**, M.G.V. Gleason, A. Schander, W. Lang, Online Cure Monitoring of Carbon Nanotube/Polyimide Films, in: 2022 IEEE Sensors, IEEE, Dallas, TX, USA, 2022: pp. 1–4. https://doi.org/10.1109/SENSORS52175.2022.9967184.
6. T. De Rijk, **M. Cen-Puc**, J.K. Piening, W. Lang, Single layer piezoresistive polyimide pressure sensor based on carbon nanotubes, in: 2022 IEEE Sensors, IEEE, Dallas, TX, USA, 2022: pp. 1–4. https://doi.org/10.1109/SENSORS52175.2022.9967230.
7. **M. Cen-Puc**, T.D. Rijk, A. Schander, M.V. Gleason, W. Lang, Strain Microsensors Based on Carbon Nanotube/Polyimide Thin Films, in: 2023 IEEE SENSORS, IEEE, Vienna, Austria, 2023: pp. 1–4. https://doi.org/10.1109/SENSORS56945.2023.10325146.
8. T.M. De Rijk, **M. Cen-Puc**, Y. Mirzaei, P. Schneider, U. Giese, W. Lang, Integrated Flexible Polyimide Sensor for Monitoring Compressive Force in Sealings, IEEE Sensors J. 24 (2024) 12153–12160. https://doi.org/10.1109/JSEN.2024.3371090.

Kóonts’íib ich Maayat’aan (Yucatecan Mayan)

Ti’ le meyaja’ jbeeta’ab jump’éel u yáalil poliimida *piezoresistiva* (5 µm u piimil) uti’al u beeta’al jump’éel *sensor* ka u p’is buka’aj u sáats’alil ba’alo’ob. Uti’al u beeta’ale’ jxa’ak’ta’ab u *nanotuboso’obil* chúuk yéetel *poliimida*.

U yáalal le *sensoro’* jmeyajta’ab yéetel *plasma* uti’al u béeytal u tak’bal. U jach chichanil u beel le *sensoro’* 50 µm u kóochil, jpa’at yéetel u nu’ukulil *fotolitografía* yóok’olal jump’éel u yáal poliimida yaan ti’ 3 % ti’ u *nanotuboso’obil chúuk*.

Le *sensoro’* jka’ap ti’ jump’éel ba’al beeta’an tu yéetel u sóoskil chúuk uti’al u p’isik buka’aj u sáats’al le *compuestoo’*. U yich le meyaja’ tu ye’esaje’ le túumben *sensoro’* ku p’isik maas ma’alob ti’ jump’éel *sensor* ku ko’onol.

Resumen en Español (Spanish)

En este trabajo se propuso una película piezoresistiva de poliimida (5 µ de espesor) para la fabricación de un sensor de deformación. Para producir este material se usó un método de mezclado directo de nanotubos de carbono con la poliimida.

Las capas del sensor se trataron mediante plasma para promover su adhesión. Los parámetros mínimos para la fabricación con fotolitografía fueron microestructuras con un ancho de línea de 50 µm para una capa de poliimida con 3 % de nanotubos de carbono.

El sensor fue embebido en un compuesto de fibras de carbono para medir las deformaciones del material. Los resultados indicaron que la sensibilidad del sensor desarrollado es mayor que la de los sensores comerciales.

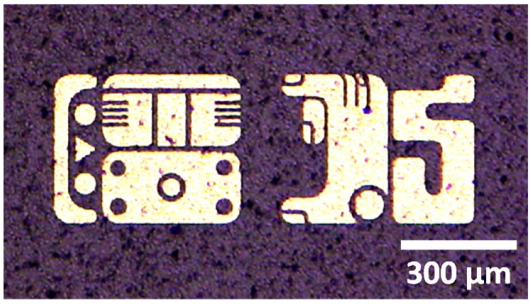

(U ts’íib Cen)

Láayli’ k-ojel t’aan yéetel ixi’im